Activation of Voltage-Gated Ion Channels in Neuroblastoma Cells by an Organic Artificial Photoreceptor

Von der Fakultät für Mathematik und Naturwissenschaften
der Carl von Ossietzky Universität Oldenburg
zur Erlangung des Grades und Titels eines
Doktor der Naturwissenschaften (Dr. rer. nat.)

angenommene Dissertation
von

Frau Oliya S. Abdullaeva
geboren am 26.05.1987
in Taschkent, Usbekistan

Gutachterin:
Jun.-Prof. Dr. Manuela Schiek
Energie- und Halbleiterforschung (EHF)
Institut für Physik

Zweitgutachter:
Prof. Dr. Michael Winklhofer
Sensorische Biologie der Tiere
Institut für Biologie und Umweltwissenschaften

Tag der Disputation: 26.04.2019

weitere Mitglieder der Prüfungskommission:

Apl. Prof. Dr. Karin Dedek
AG Neurosensorik (Animal Navigation)
Institut für Biologie und Umweltwissenschaften

Prof. Dr. Joachim Peinke
AG TWiSt
Institut für Physik & ForWind

Erklärung

Hiermit erkläre ich, dass ich die Dissertation selbstständig verfasst und die benutzten Hilfsmittel vollständig angegeben habe.
Die Dissertation wurde in Teilen bereits veröffentlicht. Eine Publikationsliste ist beigefügt.
Die Dissertation liegt oder hat weder in ihrer Gesamtheit noch in Teilen einer anderen wissenschaftlichen Hochschule zur Begutachtung in einem Promotionsverfahren vorgelegen.
Ich habe die Leitlinien guter wissenschaftlicher Praxis an der Carl von Ossietzky Universität Oldenburg befolgt.
Im Zusammenhang mit dem Promotionsvorhaben wurden keine kommerziellen Vermittlungs- oder Beratungsdienste (Promotionsberatung) in Anspruch genommen.

Oldenburg, den

_____
Oliya S. Abdullaeva

I would like to dedicate this thesis to the loving memory of my mother Mavlyuda Nuriddinova and grandfather Ramiz Nuriddinov.

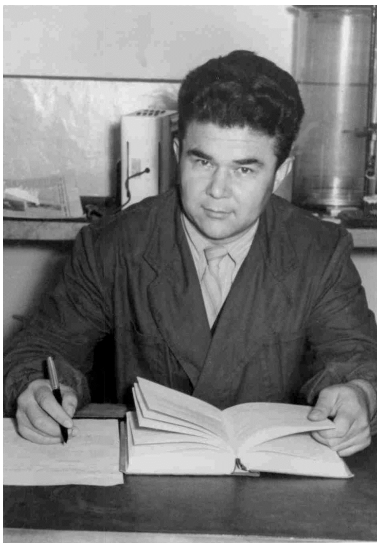

Acknowledgement

First, I would like to express my sincere gratitude to my supervisors Jun.-Prof. Dr. Manuela Schiek, Apl. Prof. Dr. Karin Dedek and Prof. Dr. Jürgen Parisi for the excellent supervision, many fruitful discussions, continuous support and guidance throughout my dissertation and giving me the opportunity to work on an exciting topic. I am very grateful to Prof. Dr. Frank Balzer, our collaboration partner from the University of Southern Denmark, who conducted in-depth measurements including AFM stability tests, spatially resolved absorbance and polarized optical microscopy recordings that contributed considerably to a better understanding of the morphological and optical properties of our squaraine artificial photoreceptors. Moreover, I thank him for taking the time to proofread my thesis. I thank our collaboration partners Prof. Dr. Arne Lützen and his former PhD student Dr. Matthias Schulz from the University of Bonn who supported our project by providing us with the SQIB material that is the basis for all artificial photoreceptor devices in this thesis.
Furthermore, I thank Prof. Dr. Michael Winklhofer for joining the board of examiners and allowing me to finalize my patch-clamp experiments in his laboratory at the end of my dissertation. Here, I would also like to thank Prof. Dr. Joachim Peinke for joining the board of examiners and taking part in my PhD defense. I am very grateful to Prof. Dr. Christoph Lienau and Prof. Dr. Karl-Wilhelm Koch for their continuous interest in our project and giving me the opportunity to join the research training group "*Molecular Basis of Sensory Biology*". I especially want to thank Prof. Dr. Arne Lützen for making me aware of the research training group in the first place and encouraging me to apply for the PhD scholarship. In addition, I thank Dr. Beate Grünberg for the support in the beginnings of my dissertation and organizing numerous workshops and events for us in the research training group.
I thank Matthias Macke, Marion Luttmann, Holger Koch, Nicole Iben, Susanne Wallenstein and Ulf Harksen (mechanical workshop) for all the

technical support in the laboratory. I am especially grateful to Nicole Iben for teaching me the cell culture technique for N2A cells. I am grateful to all former and current members of the Energy and Semiconductor Research Laboratory, in particular, Dr. Jörg Ohland, Janet Neerken, Apl. Prof. Dr. Achim Kittel, Dr. Levent Gütay, Dr. Stephan Heise, Dr. Devendra Pareek, PD Dr. Leonid Govor, Dr. Annette Hammer, Dr. Mohamed H. Sayed, Dr. Martin Knipper, Dr. Dorothea Scheunemann, Grit Schürmann and Elzbieta Chojnowski for the friendly working atmosphere and support. I would also like to thank the members of our research training group and all former and current members of both the Neurosensorics and Visual Neuroscience groups, especially Prof. Dr. Henrik Mouritsen, Prof. Dr. Martin Greschner, Apl. Prof. Dr. Ulrike Janssen-Bienhold, Dr. Christian Puller, Dr. Malte Ahlers, Dr. Jasmin Segelken, Dr. Helena Greb, Dr. Mark Pottek, Nicole Iben, Bettina Kewitz, Josef Meyer, Yousef Arzhangnia, Patrick Dömer, Lena Nemitz, Sabrina Duda, Elaheh Lotfi, Shubhash Chandra Yadav, Stefan Tetenborg, Dr. Arndt Meyer, Anne Depping for the support and providing excellent friendly working conditions. I am grateful to Angelika Maderitsch for conducting thorough SEM and TEM experiments on our organic photoreceptors and helping us gain a comprehensive insight into our devices. In particular, I am grateful to Dominik Höweling, Dr. José Fabio López Salas, Dr. Matthias Schulz, Majvor Mack, Oliver Kolloge, Dr. Sebastian Ströh, Maj-Britt Hölzel, Elena Barykina, Dr. Christopher Krause, Yvonne Zeidler, Angelika Maderitsch and Alexandra Erdt for many nice barbeque and sushi evenings, the moral support and helping me out at all times. I am deeply grateful for my friendship with Dr. Maximilian Hemgesberg who guided me throughout my dissertation and introduced me to the world of industrial chemistry. I will always appreciate the constant support, encouragement, and motivation. I thank Dr. Niklas Struch for our long-time friendship, always being there for me throughout the past years and providing me with good music and sushi.

I thank my parents Mavlyuda Nuriddinova and Dr. Sadrilla Abdullaev for everything they have done for me. Their contribution to my career will always be appreciated. Furthermore, I am deeply grateful to my uncles and aunt Hisomiddin, Fazliddin, Kamoliddin and Nozima who always took care of our family throughout the past decades. My deepest gratitude goes to my mother who motivated and encouraged me to study chemistry and follow my passion for science and research. I will always be thankful for her tireless efforts, support, advices, and guidance.

Abstract

Organic semiconductors are emerging as promising alternatives to silicon-based neuroprosthetics applied so far, especially in the field of retinal implants aimed at restoring the light sensitivity of degenerated retina. Due to their soft mechanical properties and flexibility, organic semiconducting materials exhibit a higher biocompatibility. Also, several studies have already shown their ability to restore light sensitivity in rat or embryonic chicken retinas upon photostimulation. In spite of these major achievements towards organic-based neuronal prosthetics, the mechanism of the photostimulation is subject of continuous discussion. The crucial issue of stimulation mechanism is addressed in this thesis by focusing on squaraine dyes as model semiconductor interfaced with a physiological electrolyte solution. The neurobiological aspect of this study is represented by a simple neuroblastoma cell line which is cultivated on top of the squaraine photoreceptor. Due to the voltage-gated sodium and potassium channels that are inherently present in this cell type, it is possible to investigate different phenomena at the interface and their direct impact on these ion channels by applying the electrophysiological patch-clamp technique. The results achieved in the present study underline two temporal independent photoinduced stimulation mechanisms for the organic bioelectronic interface. The most significant outcome is the observation of a capacitive coupling that facilitates a fast transient current response by the squaraine photoreceptor which in turn leads to a transient depolarization of the membrane potential. The magnitude of this capacitively mediated photostimulation is large enough to directly activate fast responding sodium channels. However, the activation of slow responding potassium channels demonstrates that the photostimulation mechanism is not limited to capacitive coupling. Especially the use of high light intensities bares the risk of causing photodamage due to irreversible redox reactions or local temperature increase during long illumination times.

Zusammenfassung

Organische Halbleiter gelten als vielversprechende Alternativen zu Neuroprothesen, die auf Silizium basieren, insbesondere auf dem Gebiet der Retina–Implantate, die eingesetzt werden, um die Lichtempfindlichkeit von degenerierten Netzhäuten wiederherzustellen. Organische Halbleiter sind aufgrund ihrer flexiblen mechanischen Eigenschaften durch eine höhere Biokompatibilität gekennzeichnet. Mehrere Studien haben bereits gezeigt, dass organische Halbleiter degenerierte oder lichtunempfindliche Netzhäute von Ratten oder Hühnerembryonen photostimulieren können. Trotz dieser Meilensteine auf dem Gebiet der organischen Neuroprothesen ist der Mechanismus der Photostimulation bei diesen Implantaten noch Gegenstand aktueller Forschung. Das Ziel der vorliegenden Doktorarbeit ist es diese Fragestellung anhand von künstlichen organischen Photorezeptoren zu beantworten. Hierfür wird ein Squarain-Halbleiter mit einer physiologischen Elektrolytlösung kombiniert. Die biologische Seite ist durch eine einfache Neuroblastom-Zelllinie repräsentiert, die auf den Squarain-Proben gezüchtet wird. Diese Zelllinie hat den Vorteil, dass sie spannungsgesteuerte Natrium- und Kaliumkanäle exprimiert, die mit Hilfe der elektrophysiologischen Patch -Clamp Technik charakterisiert werden können. Die Ergebnisse der Patch-Clamp Messungen zeigen zwei unabhängige photoinduzierte Mechanismen an der Grenzfläche zwischen organisches Halbleitermaterial, Elektrolytlösung und Zellmembran. Das bedeutendste Ergebnis ist die kapazitive Kopplung, die durch die Photostimulation an der Grenzfläche hervorgerufen wird. Hier führen transiente ionische Verschiebungsströme im Elektrolyten zu einer transienten Depolarization des Membranpotentials, die ausreicht, um direkt Natriumkanäle zu aktivieren. Ein zweiter Mechanismus unabhängig von der kapazitiven Kopplung wurde auch gefunden, der Kaliumkanäle aktiviert. Die Ursache hierfür ist wahrscheinlich das Auftreten von thermischen oder photochemischen Effekten, die durch hohe Lichtintensitäten und lange Beleuchtungszeiten verursacht werden.

Contents

Chapter 1

Introduction

Vision is the result of a highly complex phototransduction that takes place in the retina. The light-sensitive photoreceptor layer is the starting point where light is absorbed by rod and cone photoreceptor cells. This in turn sets off a cascade of biochemical and electrical signals that are transferred through the multi-layered retina and into the brain via the optic nerve. Each layer contains numerous types of cells that contribute to the signaling pathway.[1] The photoreceptor layer is vulnerable to different varieties of retinal degeneration that cause severe visual impairment and eventually complete blindness and affect around 170 million people worldwide.[2,3] The two most common retinal degenerative diseases are age-related macular degeneration (AMD) and retinitis pigmentosa (RP).[3] Once the photoreceptor layer starts degenerating the signaling cascade breaks down. Consequently, the remaining retinal tissue does not get input from the photoreceptors anymore.[3]

Although AMD and RP cannot be cured, numerous types of novel therapies are emerging.[3] Besides gene therapy and stem cell transplantation,[4,5] several promising strategies for a prosthetic treatment have been developed in the past few decades.[3] Interfacing artificial devices with the degenerated retina is aimed at electrically stimulating the residual retinal layers that mostly survive the degeneration process.[3] Though the retina suffers alterations and reorganization after the loss of the photoreceptor layer,[6,7] studies have shown that bipolar and ganglion cells maintain their functionality to a certain degree.[8–13] Therefore, they have been a preferred target for bioelectronic retinal implants.[3]

The first attempts to stimulate neurons electrically were reported in the 18th century.[3] In experiments conducted by LeRoy in 1775, the blind perceived light sensations when their head was exposed to electrical currents. Further experiments in 1780 by Galvani showed that muscles in dead frogs' legs can be successfully stimulated by electricity.[3,14–17] Advanced studies that finally paved the way for today's prevalent retinal prosthetics started almost 200 years later in the 1960s. Brindley and Lewin showed in their study from 1968 that the visual cortex can be electrically stimulated resulting in so-called phosphenes, perception of light independently from the phototransduction where light needs to be absorbed by the photoreceptor layer first.[3,18–20] Later on in 1999, Humayun et al. tested multi-electrode arrays on blind patients. These initial pilot experiments under acute conditions not only evoked phosphenes but further revealed the correlation between localization of the light sensation and specific domain of electrical stimulation in the retina.[10] Localized electrical stimulation was also realized in additional studies by Rizzo et al. during which RP patients were able to distinguish two different stimulation points.[3,21]

Nowadays, several types of retinal implants have been approved for clinical trials or are even commercially available. Usually, they are divided into three categories depending on the location of the electrical stimulation: epiretinal, subretinal and suprachoroidal implants.[3] While epiretinal stimulation (e.g., Argus II) activates ganglion cells directly with multi-electrode arrays[22–33], subretinal implants (Alpha IMS) make use of the retinal circuitry and target the residual retinal layers.[34–38] This approach is aimed at replacing the photoreceptor layer and reactivating the natural signaling pathway by primarily stimulating bipolar cells. Suprachoroidal arrays that are implanted into the sclera are not commercially available and show limitations in the spatial resolution because of the larger spatial distance to the retinal tissue.[39] Both Argus II and Alpha IMS rely on inductive coupling as a power source. However, the advantage of the Alpha IMS subretinal implants is that they make the need for external goggles obsolete due to the use of light-sensitive photodiodes instead of mere electrode arrays.[39] Ideally, the prosthetics would benefit the patients even more if the devices were not dependent on external power sources.[3] Indeed, this issue was dealt with in the development of the novel PRIMA subretinal implant which entered the clinical stage in 2018.[39,40] The goal here is to utilize the photovoltaic nature of the silicon-based devices that can power themselves and simultaneously transfer the visual images to the ill retina

via electrical stimulation.[41–45]

All abovementioned technologies are truly remarkable and are considered as key milestones in the field of bioelectronics. Especially the PRIMA implant is a step closer to self-powering artificial photoreceptors. Nevertheless, the rigid inorganic nature of these devices is a critical issue. In order to achieve a sufficient light absorption, the silicon chips need to be thick.[46] This, on the other hand, could injure the very flexible thin retinal tissue. Furthermore, the biocompatibility is also an important requirement to ensure long-lasting functionality without rejection and to decrease the inflammatory risk.[47–49] Obviously, highly flexible soft materials with the ability to easily adapt to the natural curvature of the retina and that are simple and cheap to fabricate would improve these mechanical problems.[50–55] The emerging field of organic bioelectronics is trying to meet these demands by utilizing the unique properties of organic semiconductors.[56–58] In addition to their photovoltaic nature, they are biocompatible, chemically tunable and show a narrow absorption band very specific to their chemical nature which might enable color discrimination in future artificial stand-alone bionic retinas. Moreover, intermolecular van der Waals forces determine the flexibility which is a clear advantage in terms of the device size. Bigger prosthetics that electrically stimulate large parts of the retina could increase the visual field and contain large numbers of pixels. This in turn would improve the visual acuity.[59–70] Several international research groups have already successfully shown that numerous types of organic semiconductors have the ability to photostimulate degenerated retina.[71] Among them is the polymer poly(3-hexylthiophene-2,5-diyl) (P3HT) that was used by Lanzani et al. and Narayan et al. to restore the light sensitivity of blind rat retinas.[72–80] They adapted the concept of a photovoltaic device by combining the polymer with an indium tin oxide (ITO) electrode and attached degenerated retinal tissue on top of the photoactive layer. Subsequent photostimulation with pulsed illumination triggered an active response by the ill retina in the form of action potentials. The Lanzani group succeeded a few years later in fabricating a flexible P3HT-based prosthesis supported on a conductive polymer PEDOT:PSS and silk fibroin that were directly implanted into a rat model for retinitis pigmentosa. The devices restored the light sensitivity and visual acuity as was revealed by behavioral and electrophysiological studies, even 6-10 months after implantation.[80] Artificial retinal devices based on nanorod-carbon

nanotubes have also been reported by Hanein et al. that restored the light sensitivity of chick retina.[81–83]

Apart from artificial retinal implants, there has been a growing effort to restore light sensitivity using optogenetics. This is an endogenous approach towards artificial vision. Unlike technologies that include the implantation of devices, optogenetics aims at altering the degenerated retina genetically by transfecting the neurons with genes that can encode photosensitive ion channels e.g., channelrhodopsin2 and halorhodopsin. The technique is however not unproblematic since the gene expression is undertaken with viruses giving rise to safety issues.[50,76,84]

Due to their beneficial mechanical and optoelectronic properties, organic semiconductors are promising candidates for many biomedical applications that even go beyond retinal prosthetics and are therefore gaining importance in the field of bioelectronics. However, the underlying cause for the observed photoinduced neuronal activity is under scrutiny. There is a high demand for a thorough understanding of their working mechanism when exposed to living tissue.[71]
Research groups focusing on P3HT-based devices have proposed a capacitive coupling in their initial work.[72] But later experiments conducted on single HEK cells revealed that capacitive events at the interface play a passive role, it is rather a thermal coupling that leads to a substantial depolarization of the cell membrane.[85] According to this mechanism, photostimulating the polymer causes the release of thermal energy resulting in the local heating of the electrolyte surrounding the cell membrane. Furthermore, it was reported that both polythiophene films and organic pigments can directly activate temperature-gated Vanilloid Receptor 1 (TRPV1) channels, indicating that thermal coupling is a universal phenomenon for organic semiconductor-electrolyte interfaces.[86,87] Besides local temperature changes, the possibility of a chemical coupling was also reported for P3HT films including variations in the pH of the electrolyte upon illumination which induces local acidification.[87] Granted, thermal and chemical signaling pathways show great potential in modulating neuronal and cellular activity, but future organic-based retinal implants would need to operate solely via capacitive coupling due to harmful effects of heating and irreversible redox reactions. Organic semiconductors are not good candidates regarding Faradaic charge injections. Here, they usually generate reactive

oxygen species that are futile for healthy biological tissues.[88]

In comparison, safe stimulation mechanisms already exist for their inorganic counterparts, including reversible charge-balanced Faradaic charge injection via iridium electrodes and capacitive coupling using titanium nitride electrodes.[89] Seminal studies done by Fromherz et al. gave interesting insights into capacitive interfaces for non-invasive extracellular neuronal stimulation via silicon chips.[90–99] Their accomplishments elucidated the importance of a direct interaction between voltage-gated ion channels and inorganic semiconductors during an ion-electron coupling.[98] Fromherz et al. developed electrolyte/oxide/semiconductor (EOS) capacitors and cultured them with HEK cells expressing voltage-gated sodium and potassium channels.[98] The application of specific voltage ramps to the chip induced displacement currents within the oxide followed by an ohmic current in the electrolyte bath which ultimately resulted in a sufficient negative extracellular voltage to activate ion channels.[98] These groundbreaking findings illustrated the significance of an additional oxide layer for bioelectronic interfaces. The introduction of a metal oxide as an insulating layer increases the capacitance, the ability to store electrical charge and blocks harmful Faradaic charge transfer. The choice of material for a safe neuronal stimulation is therefore crucial.
According to recent studies, capacitive coupling can be achieved only by combining organic semiconductors with charge injecting metal electrodes as reported in novel studies conducted on P3HT and organic pigments.[59,100] The question if photostimulation via capacitive coupling can be realized with pure organic semiconductors remains unresolved.

Chapter 2

Motivation

The aim of this thesis is to understand the underlying mechanism of photostimulation for organic-based photovoltaic bioelectronics and evaluate in particular the feasibility of a photomediated capacitive coupling for pure organic semiconductor-electrolyte-cell interfaces.
The present work takes a truly interdisciplinary approach by combining the fields of optoelectronic organics and electrophysiology. As a part of the research training group "Molecular Basis of Sensory Biology GRK-1885" (funded by the German Research Foundation) the project was carried out at the Energy and Semiconductor Research Laboratory as well as at the Institute for Biology and Environmental Sciences under the supervisions of Jun.-Prof. Dr. Manuela Schiek and Apl. Prof. Dr. Karin Dedek.

⇒ **Artificial photoreceptor design and characterization:**

To investigate fundamental mechanistic events at organic-based biointerfaces, the first step is to select a suitable organic semiconductor. Here, due to their environmental stability, the class of squaraine dyes is an interesting candidate.[101,102] Although squaraine dyes have been studied extensively in a variety of different fields, including imaging, nonlinear optics, photovoltaics, photodynamic therapy, and ion sensing, they have not been applied in the field of organic bioelectronics yet.[102–105] Typically, they have an aromatic four-membered ring structure and exhibit a resonance stabilized zwitterionic structure (Figure 2.1).[102] High absorption coefficients and their ability to absorb in the visible and near-infrared spectral region make them attractive candidates for electron donor materials in optoelectronic devices.[106–112] Recently, it was found that squaraine-based photovoltaic devices exhibit a poor charge carrier extraction which elicits

the formation of space charges.[113,114] Although space-charge limitation is detrimental to organic solar cells, many studies show that they can be utilized in optoelectronic devices intended for transient photodetection and most importantly for organic artificial retinas aimed at capacitive stimulation.[115–127].

For the purposes of this thesis, a small molecule squaraine compound was selected as organic semiconductor model 2,4-bis[4-(*N*,*N*diisobutylamino)-2,6-dihydroxyphenyl]squaraine designated as SQIB throughout the present work (Figure 2.1). The investigations that will be undertaken here entail the fabrication of photovoltaic thin film devices based on SQIB and the characterization of their morphological and optical features. An important aspect will be to determine the possibility of applying these SQIB devices as organic photosensors in an aqueous biological environment.

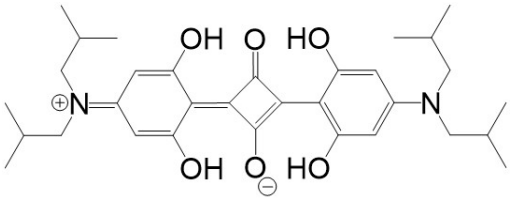

Figure 2.1: Structural formula of SQIB (2,4-bis[4-(*N*,*N*diisobutylamino)-2,6-dihydroxyphenyl]squaraine).

⇒ Cellular approach:

With regard to the applicability of organic semiconductors as artificial retinal implants, the choice of testing these devices on degenerated retinal tissues is justified. However, large neuronal networks are too complex since they exhibit different types of cells and numerous stimulation sites which make it difficult to trace back any potential photoinduced activation to a specific stimulation pathway. This discrepancy is evident in studies that claim to achieve a neuronal stimulation via capacitive coupling by merely showing photoinduced action potentials without supporting the data with an additional direct measurement of voltage-gated ion channels, that are the basis for neuronal firing.[59,72,75,100] As action potentials can also be elicited by temperature changes at the interface, it is essential to investigate the effect of photoinduced events on voltage-gated ion channels first.[128,129]

The study of coupling mechanisms presented in this thesis is therefore conducted on single undifferentiated neuroblastoma cells, termed in this thesis as N2A that function here as a neuronal model. Electrical stimulation experiments including artificial charge injection show that although single undifferentiated N2A cells lack the ability to generate action potentials their membrane voltage can be altered reaching threshold voltage values allowing the activation of voltage-gated sodium and potassium channels which are inherently present in these cells. Since these ion channels can be activated independently on two different time scales and are the basis of electrical signaling in more complex neurons, they constitute an ideal target for a potential photomediated electrical stimulation.

⇒ Experimental approach: patch-clamping and transient photocurrent measurements:

The objective here is to determine if these ion channels can be activated by the artificial SQIB photosensor via photostimulation. To this end, the electrophysiological patch-clamp technique is employed to record any potential photomediated electrical responses in single N2A cells grown on the SQIB device. A crucial aspect of this study is the identification of the mechanism that leads to that activation by performing photocurrent measurements of SQIB devices interfaced with a physiological aqueous electrolyte.

Outline of the following chapters:

Chapters 3 and 4:
These chapters introduce different concepts that have been implemented in the fields of neurobiology, electrophysiology, neurostimulation, and organic semiconductors.

Chapter 5:
This chapter focuses on the results collected during the first part of the project that entailed a proof of principle study on SQIB-electrolyte-N2A interfaces including the fabrication and characterization of SQIB photodevices and testing these on N2A cells. Apart from a quantitative analysis of the cell growth, the photoinduced electrical responses of the N2A cells are recorded via patch-clamping.

Photocurrents measured within the electrolyte give insight into the events at the SQIB-electrolyte-cell biointerface during illumination. In the end, the stability of the artificial photosensors is tested via atomic force microscopy.

Chapter 6:
This chapter demonstrates how the device performance and its effect on the membrane potential can be optimized by systematically modifying the thin film morphology, the capacitance of the semiconductor-electrolyte interface, the resistance of the electrolyte and indium tin oxide (ITO) electrode.

Chapter 7:
The final part of the study is presented here. It includes a test showing how the optimized device affects cell growth. Finally, this chapter also answers the question if voltage-gated ion channels can be activated via photocapacitive stimulation.

Chapters 8 and 9: Discussion, Conclusion, and Outlook
The aim here is to propose and explain two types of photostimulation mechanisms for the biointerface on the basis of the results obtained in the previous chapters and compare them with studies conducted on other types of semiconductors.

Chapter 10: Experimental section
The experiments conducted in Chapters 5-7 are described here in detail, including device fabrication, patch-clamping, photocurrent measurements, atomic force microscopy (AFM), absorbance spectroscopy, external quantum efficiency (EQE), cell culture, LED settings and alignment, optical microscopy, differential interference contrast (DIC) microscopy, scanning electron microscopy (SEM) and transmission electron microscopy (TEM).

Chapter 3

Principles of Electrophysiology and Neurostimulation

This chapter gives a general overview of basic concepts that have been implemented in the fields of neurostimulation and electrophysiology, areas that are closely related. Technological achievements in electrophysiology allowed a better understanding of the electrical processing in neuronal systems. This facilitated, in turn, whole new bioelectronic therapy strategies with the goal to electrically target specific neuronal sights. Before focusing on bioelectronic electrode-electrolyte interfaces that are the core of neurostimulation, it is crucial to understand the bioelectricity of biological structures first.

3.1 Bioelectricity

In biological organisms, the cell membrane plays a key role in separating the cytoplasm from the extracellular environment. The molecular basis are phospholipids that feature both hydrophilic and hydrophobic fatty acid chains which assemble into a bilayer with the polar side chains facing the aqueous surrounding on either side of the membrane while the nonpolar ends constitute the middle of the cell membrane.[130–134] The aqueous environment is composed of ionic charge carriers, e.g. sodium, potassium, chloride and calcium ions. The different concentration of ions on either side of the bilayer gives rise to an electrical potential across the membrane while the osmolarity is the same for both sides (Figure 3.1).[131,135]

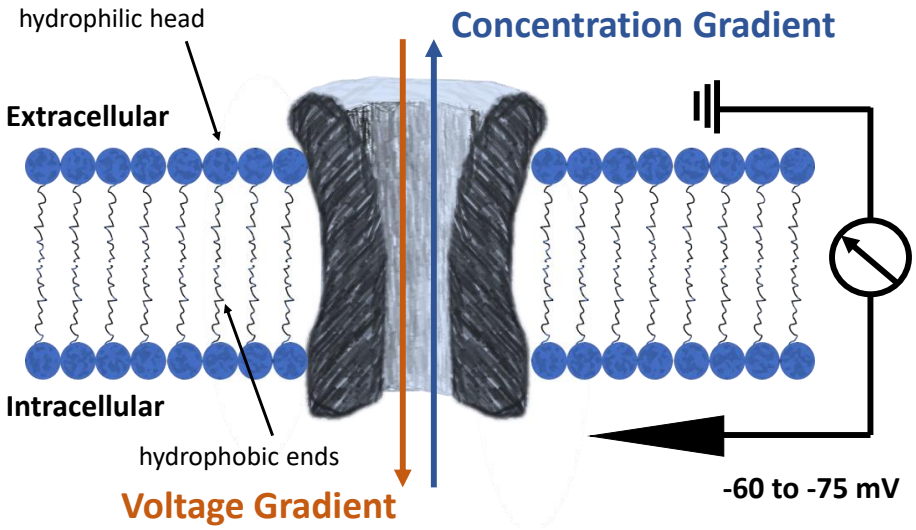

Figure 3.1: Schematic depiction of a lipid bilayer that constitutes a membrane. Ion channels are embedded into the lipid bilayer and allow passive flow of ions along their concentration and voltage gradient. Different concentrations of ions on the extra- and intracellular side of the lipid bilayer give rise to a membrane potential. (Adapted from *From Molecules to Networks.*[131])

Type of ion	Extracellular	Intracellular	Equilibrium potentials E
Na^+	150 mM	18 mM	+ 56 mV
K^+	3 mM	135 mM	-102 mV
Cl^-	120 mM	7 mM	-76 mV
Ca^{2+}	1.2 mM	0.1 µM	+125 mV

Figure 3.2: An overview of concentrations of sodium, potassium, chloride and calcium ions in the extra-/intracellular medium and the equilibrium potential for each ion channel.[131] (Adapted from *From Molecules to Networks.*[131])

This potential is maintained by active ionic pumps embedded in the membrane and the ion selectivity of ion channels in the selectively permeable membrane. Ion channels are proteins that are permeable only to a certain type of ion which can diffuse through the channels along the concentration gradient.[131,135] In contrast, ionic pumps actively transport ions under energy consumption across the membrane against the concentration gradient. Figure 3.1 gives a schematic overview of a cell membrane and an ion channel. The respective concentrations for each ionic species distributed in the intra- and extracellular area are shown in Figure 3.2.[131,135]

The passive flow of charged ions I across the channels can be quantified as the sum of ion flow down the concentration $I_{\text{concentration}}$ and voltage gradient I_{voltage}:[131]

$$I = I_{\text{voltage}} + I_{\text{concentration}} \tag{3.1}$$

There is no net current flow when the ion channel reaches an electrochemical equilibrium, where the movement of ions across the ion channel is balanced by an electrical gradient in the opposite direction. This stage is also termed the equilibrium potential E_{ion} as described by the Nernst equation (R: gas constant, T: temperature, F: Faraday's constant, z: valence of the ion, $[\text{ion}]_{\text{o}}$ and $[\text{ion}]_{\text{i}}$: ion concentration inside (i) and outside (o) of the cell):[131]

$$E_{\text{ion}} = \frac{RT}{zF} \ln\left(\frac{[\text{ion}]_{\text{o}}}{[\text{ion}]_{\text{i}}}\right) \tag{3.2}$$

The equilibrium potentials for each type of ion channel are shown in Figure 3.2. Later on, the Goldman-Hodgkin-Katz equation, a variation of the Nernst equation was introduced for the resting membrane potential V_{m} under consideration of the ionic concentration of sodium, potassium and chloride ions and the relative permeability of the membrane p_{ion} to each ionic species:[131]

$$V_{\text{m}} = \frac{RT}{F} \ln\left(\frac{p_{\text{K}}[\text{K}^+]_{\text{o}} + p_{\text{Na}}[\text{Na}^+]_{\text{o}} + p_{\text{Cl}}[\text{Cl}^-]_{\text{o}}}{p_{\text{K}}[\text{K}^+]_{\text{i}} + p_{\text{Na}}[\text{Na}^+]_{\text{i}} + p_{\text{Cl}}[\text{Cl}^-]_{\text{i}}}\right) \tag{3.3}$$

The resting membrane potential V_{m} is by definition the potential inside the cell relative to the outside and usually amounts to approximately -60 to -75 mV for typical mammalian neurons, meaning that the intracellular side is charged more negatively.[131]

Hodgkin-Huxley Model

In 1952, Alan Hodgkin and Andrew Huxley presented their pioneering Hodgkin-Huxley model to explain the electrical properties of excitable neurons. Here, they modeled the cell membrane as an electrical circuit consisting of a capacitive element C_m representing the dielectric nature of the lipid bilayer (Figure 3.3).[131,135–141]

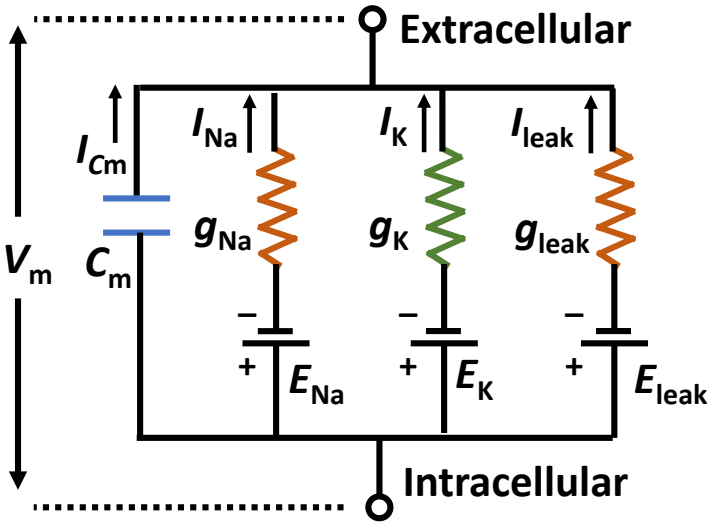

Figure 3.3: Hodgkin and Huxley used an electrical circuit to model the electrical properties of the cell membrane. They introduced the concept of a parallel *RC*-circuit with a capacitor C_m and resistor for the membrane lipid bilayer and the ion channel conductances g_ion, respectively. The specific electrochemical potential gradient E_ion was represented by battery elements in series with the resistors. (Adapted from *From Molecules to Networks.*[131])

Furthermore, the circuit was complemented with resistors, equivalent to the conductances g_ion of ion channels and leakage current that are parallel to the capacitive element C_m and in series with a battery representing the specific electrochemical potential gradient E_ion. According to this equivalent circuit, the total current flow I_membrane across the membrane can be subdivided into capacitive currents $I_\mathrm{capacitive}$ that are associated with the charging of the lipid bilayer capacitor and direct ionic currents I_ionic in ion channels (Equations 3.4 and 3.5).[131,142]

$$I_{\text{membrane}} = I_{\text{capacitive}} + I_{\text{ionic}} \tag{3.4}$$

$$I_{\text{membrane}} = C_{\text{m}} \left(\frac{\mathrm{d}V_{\text{m}}}{\mathrm{d}t} \right) + \frac{V_{\text{m}}}{R} \tag{3.5}$$

Neuronal cells can exibit both passive and active electrical signals upon electrical stimulation. Figure 3.4 summarizes different types of possible voltage signals stemming from a neuron that occur upon current injection.[135]

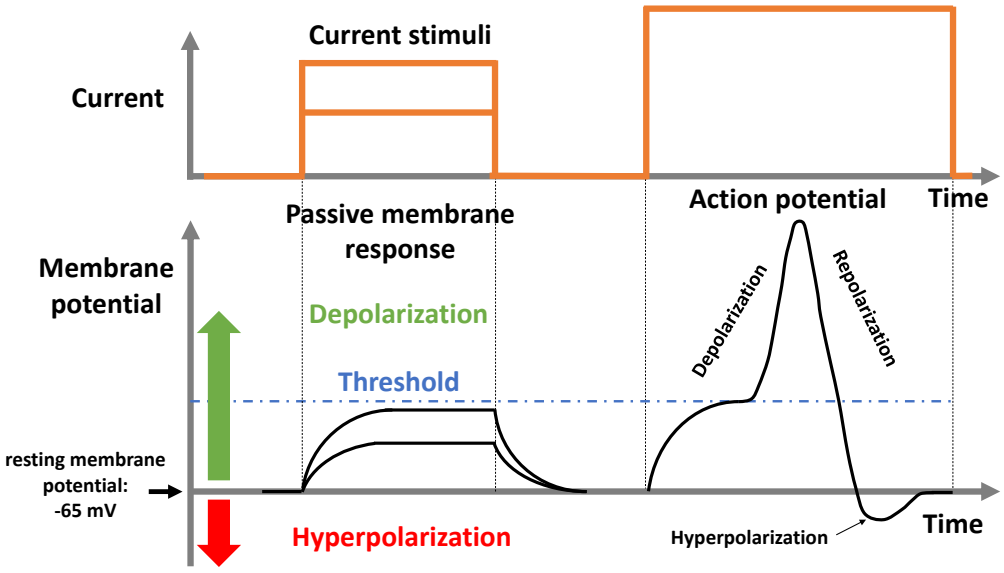

Figure 3.4: Schematic overview of voltage responses (bottom) induced by artificial current stimuli (top) in a nerve cell. Passive membrane response: before the onset of the current stimulus the nerve cell is situated at a resting membrane potential (e.g., -65 mV). A shift of the membrane potential to more positive values upon the onset of the stimulus is designated as a depolarization. A shift to more negative values would be considered a hyperpolarization. Active membrane response: if the magnitude of the current stimulus is large enough the membrane potential can depolarize to a threshold value that initiates an action potential that is characterized by an initial depolarization phase where the membrane potential reaches even more positive values than the threshold. This phase is followed by a repolarization that features a drop in the membrane potential. During a short hyperpolarization phase, the membrane potential shifts to more negative values before regaining the initial resting membrane potential. (Adapted from *Neuroscience*.[135])

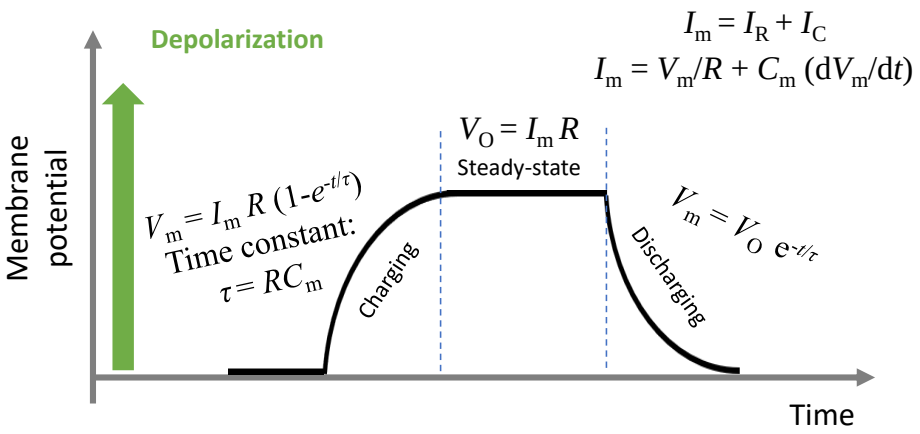

Figure 3.5: A detailed illustration of the passive voltage signal depicted in Figure 3.4. The signal is characterized by a charging and discharging phase upon on- and offset of the current stimulus, respectively that can be described mathematically with exponential functions. R: membrane resistance, C_m: membrane capacitance, τ: time constant, V_m: membrane potential, V_O: steady-state membrane potential, I_m: current across the membrane, sum of capacitive I_C and ionic I_R currents. (Adapted from *Molecular and Cellular Physiology of Neurons* [142] and *Neuroscience.* [135])

A positive shift in the resting membrane potential is designated as depolarization, whereas a hyperpolarization is associated with a negative shift. During the depolarization, the inside of a neuron becomes more positive compared to the outside resulting in a rise in the voltage. [135,142] Since the behavior of the cell membrane basically resembles a parallel RC-circuit (Figure 3.3), the rise of the membrane potential does not immediately change upon applying a current (Figure 3.5). [143] At first the current flows solely across the capacitor where the displacement current initiates a potential difference by increasing the charge separation. The flow of capacitive current is reflected in the rise of the membrane potential (see Figure 3.5: "charging") which can also be described mathematically via the exponential function shown in the same Figure. [135,142–145] Following the rise of the membrane potential, the RC circuit enters a steady-state phase where the current flows only through the resistor that is induced by the same potential difference that was present across the capacitor while the displacement current gradually diminishes. [131,135,143] When the electrical stimulation is turned off, displacement currents dominate the RC circuit again, resulting in an exponential drop of the membrane voltage that regains the initial resting state (see Figure 3.5: "discharging").

The time that is required to alter the membrane potential during electrical stimulation depends on the resistance R and capacitance C_{m} of the cell membrane and is given by the time constant τ:[131,135,142,143]

$$\tau = RC_{\mathrm{m}} \tag{3.6}$$

In contrast, action potentials are active membrane voltage responses, termed "*all-or-non*"[146] events that appear in excitable neurons when the membrane potential is depolarized above a certain threshold value.[135] In their work on squid giant axons, Hodgkin and Huxley recognized the ionic basis of action potentials: fast inward sodium currents across sodium ion channels that depolarize the membrane and slow outward potassium currents through potassium ion channels that ensure a repolarization.[135,147] After almost 30 years, the inventors of the patch-clamp technique which will be introduced later, Sakmann and Neher verified the observations of Hodgkin and Huxley via direct measurements of single sodium and potassium channels.[146,148] Because this thesis focuses on single N2A cells that express sodium and potassium channels, it is important at this point to address the characteristic features of these ion channels.

Voltage-Gated Ion Channels

Sodium and potassium ion channels belong to the class of voltage-gated ion channels that open or close depending on the membrane potential. These type of ion channels contain a voltage sensor that responds to changes in the membrane potential. When the membrane potential is either depolarized or hyperpolarized these voltage sensors initiate structural changes in the ion channel, either an opening or closing. The opening of the channels allows ions to diffuse through the channels along their electrochemical gradient. Hodgkin and Huxley introduced following mathematical description which states that this ionic current I_{ionic} in voltage-gated sodium and potassium channels is proportional to the membrane conductance g_{ion} (reciprocal of the membrane resistance R):[135,146]

$$I_{\mathrm{ionic}} = g_{\mathrm{ion}}(V_{\mathrm{m}} - E_{\mathrm{ion}}) \tag{3.7}$$

While I_{ionic} represents either the sodium or potassium current, g_{ion} is the conductance. According to this equation the ionic current is further determined by the electrochemical driving force which is the difference between the membrane potential V_{m} and the equilibrium potential E_{ion}.[135] The experiments conducted by Hodgkin and Huxley on giant squid axon revealed that the ion channels respond with a temporal variation in their conductance when the membrane potential is depolarized.[135] Further findings showed that this change in the conductance correlates with sodium and potassium currents originating from the respective ion channels. In the following, the dynamics of these ion channels will be explained on the basis of N2A cells that also exhibit voltage-gated ion channels making them an ideal cell model.

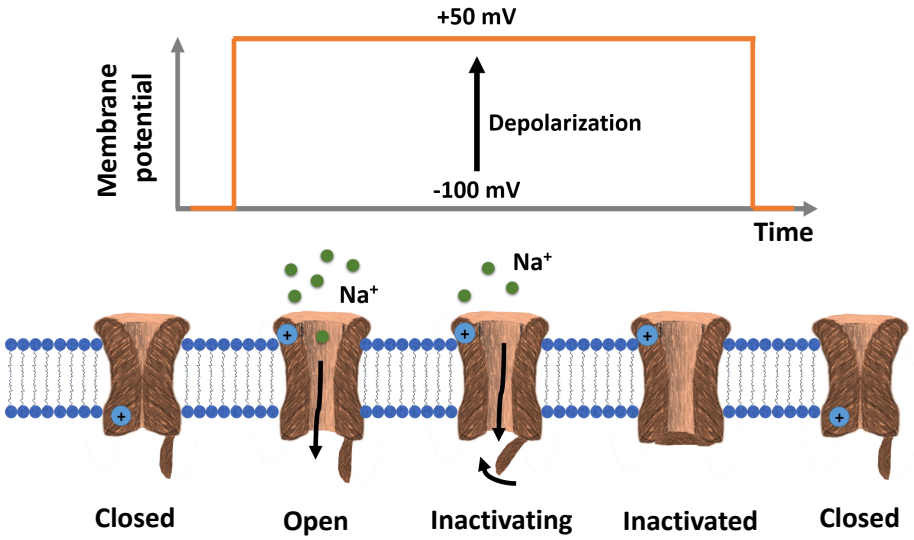

Figure 3.6: A schematic image of the structural changes that occur in sodium ion channels initiated by a depolarization step from -100 mV to +50 mV. Note that the voltage sensor of the ion channel is visualized schematically by a blue "+" sign. Initially, the sodium channels are situated in a closed state before the onset of the depolarization pulse. Upon depolarization the voltage sensors detect the potential change and elicit the opening of the sodium channels instantly, allowing an inward flow of sodium ions. The open state is followed by an inactivation even though the depolarization pulse is continued. Upon termination of the depolarization pulse, the sodium channels are hyperpolarized and regain their closed state. (Adapted from *Neuroscience*.[135])

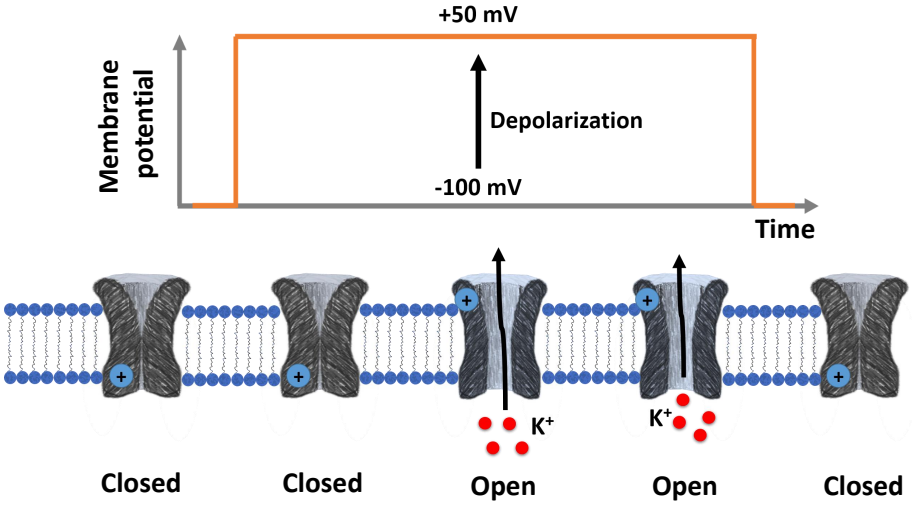

Figure 3.7: A schematic image of the structural changes that occur in potassium ion channels initiated by a depolarization step from -100 mV to +50 mV. Note that the voltage sensor of the ion channel is visualized schematically by a blue "+" sign. Initially, the potassium channels are situated in a closed state before and shortly after the onset of the depolarization pulse. While sodium ion channels start inactivating (see Figure 3.6), potassium channels enter their activation state which continues until the depolarization pulse is terminated. The activation of the potassium channel leads to the opening of the channel allowing an outward flow of potassium ions. (Adapted from *Neuroscience*.[135])

Figure 3.8 shows an overview of sodium and potassium currents recorded in a N2A cell while applying a depolarization pulse. Here, as in all electrophysiological techniques, the negative current response signalizes an inward flow of sodium ions (from the outside into the inside of the cell). The positive current signal represents an outward flow of potassium ions (inside to outside).[135,146]

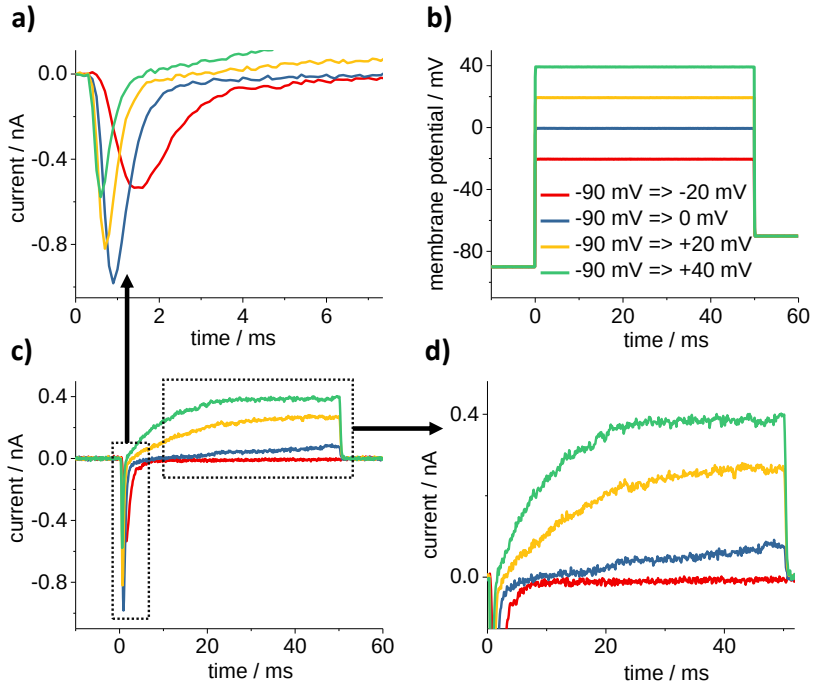

Figure 3.8: Artificial depolarization test conducted on a N2A cell grown on a glass substrate in whole-cell configuration and in physiological electrolyte solution (termed "standard Ringer's solution" that has following composition (in mM): 137 NaCl, 5.4 KCl, 1.8 $CaCl_2$, 1 $MgCl_2$, 10 D-glucose, and 5 HEPES (pH adjusted to 7.4 with 1 M NaOH)). A variety of 50 ms artificial depolarization pulses were applied to the N2A cell as shown in Figure 3.8 b). Figure c) gives an overview of negative sodium inward and positive potassium outward currents measured in voltage-clamp mode. A close-up of the sodium currents induced by the artificial depolarization can be found in a). d) depicts a close-up of the potassium outward currents. The current traces represent one N2A cell.

Sodium channels are characterized by a very fast dynamic. The current signal reaches it's maximum after few milliseconds whereas potassium channels activate very slowly, showing a current maximum only after 40 ms. Another important feature of sodium channels is the decay of the current response which represents the inactivation phase of the ion channel. During depolarization, ion channels switch between different states (Figures 3.6 and 3.7).[135,146] At the resting membrane potential, both channels are closed. Immediately after the onset of the depolarization pulse sodium channels are activated and subsequently open while potassium channels are in a closed state. Although the depolarization is constant, the sodium channels enter an inactivation state after a few milliseconds which results in the interruption of the ion flow. Simultaneously, potassium channels open. Compared to sodium channels potassium channels do not inactivate, the ion flow continues until the depolarization pulse is turned off.[135,146]

During electrophysiological experiments both sodium and potassium channels can be selectively blocked with different types of blocking agents, resulting in a zero ionic current flow along the ion channels. This provides the possibility to distinguish between different types of ionic currents and also between active and passive current responses. Tetrodotoxin (TTX) can selectively block sodium channels when added to the extracellular medium. There are also three types of chemicals that are used to block ion channels intracellularly: CsCl and tetraethylammonium (TEA) for potassium channels and QX-314 bromide for sodium channels.[98,149,150]

Action Potentials

The temporal progression of an action potential voltage signal recorded in neurons is based on the activity of ion channels (Figure 3.9).[135,146]

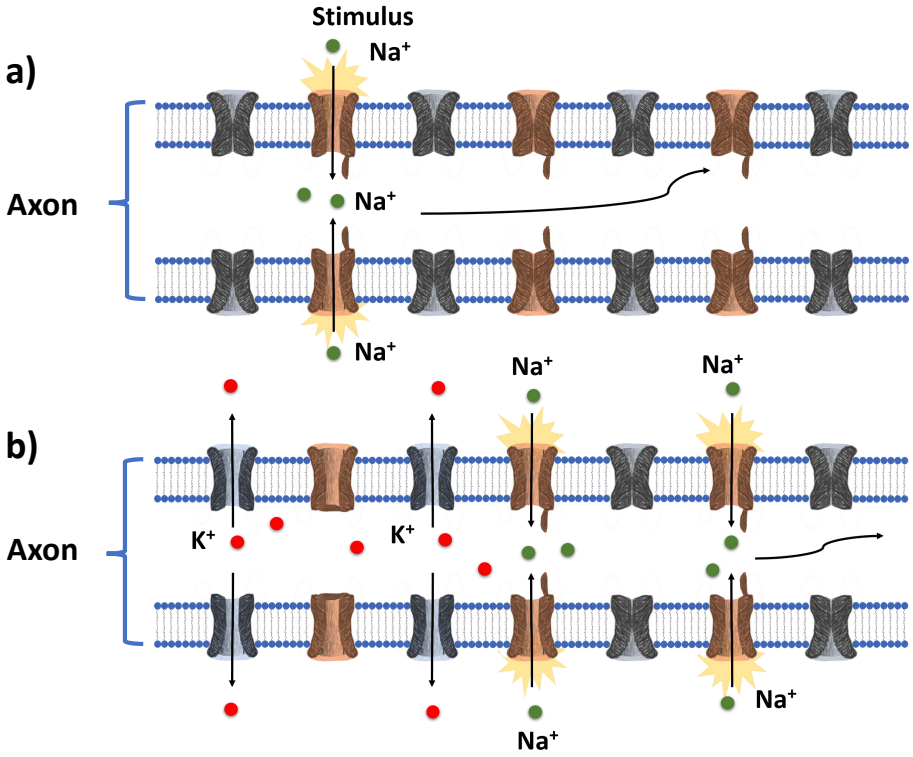

Figure 3.9: Schematic representation of the processes that take place in an axon during an action potential. a) Upon a local activation of sodium channels via an external stimulus sodium ions flow across the sodium channels into the axon. b) The sodium ions flow passively along the axon (black arrows) and depolarize neighboring sodium channels initiating their activation while the sodium channels at the first stimulation site deactivate. While sodium channels enter their inactivation phase, potassium channels activate resulting in an outward flow of potassium ions. (Adapted from *Neuroscience*.[135])

The depolarization phase stems from the inward flow of sodium ions that make the inside of the neuron more positive due to activation of sodium channels triggered by an external stimulus. Once the sodium channels inactivate, potassium channels are activated causing the repolarization due to the outward flow of potassium channels that remove the excess positive charge. This step is followed by a slight hyperpolarization before the resting membrane potential is restored because the outward flow of potassium ions makes the inside more negative for a short period of time. Characteristic behavior of actions potentials is the possibility of a spacial propagation along an axon. Figure 3.9 illustrates how an initial action potential can trigger a second one in the same neuron. This can be explained by the passive flow of positive sodium ions along the neuron that depolarize neighboring closed sodium ion channels.[135,146]

3.2 The Patch-Clamp Technique

The knowledge about the electrical properties of living organisms is based on electrophysiological measuring techniques. The beginnings of modern-day electrophysiology go back to the middle of the 20th century where glass electrodes (glass pipettes filled with a conductive physiological solution and an electrical wire) were used for measuring membrane potentials, transmembrane currents and even injecting current by directly penetrating the cell membrane of neuronal tissues. The development of micropipettes contributed considerably to the advancement of electrophysiology.[151]
In 1976, Neher and Sakmann developed the patch-clamp technique which compared to other electrophysiological techniques offers several advantages: 1) only one electrode suffices for voltage measurement and current injection. Hence, it can also be termed as a continuous single-electrode voltage clamp technique (cSEVC)[146], 2) the single electrode is also suitable for small cells that otherwise can not be recorded by intracellular two-electrode techniques, 3) recording of single channels and 4) good signal-to-noise ratio by avoiding the penetration of the cell membrane and instead establishing a tight seal between cell membrane and glass pipette, allowing recordings of picoampere currents.[148,151,152] As in all electrophysiological techniques, the recording electrode consists of a glass micropipette that is filled with an electrolyte (intracellular solution) and electrically contacted with the amplifier via a nonpolarizable Ag/AgCl wire.

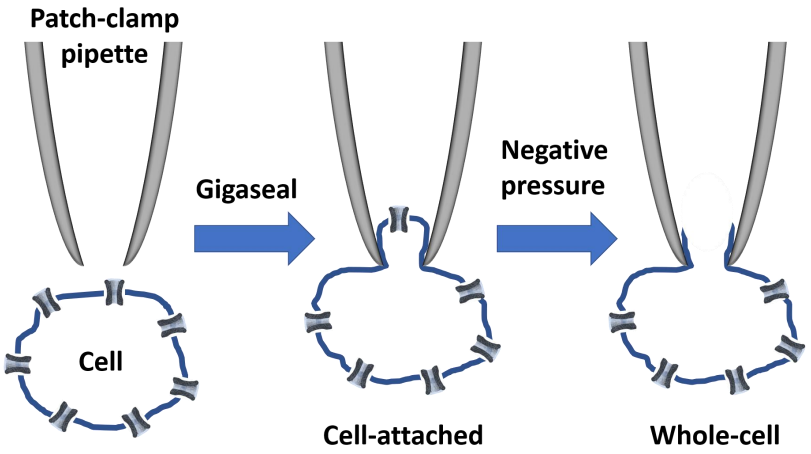

Figure 3.10: Schematic overview of the patch-clamp procedure which involves establishing a gigaseal between the patch-clamp glass microelectrode and the cell membrane (cell-attached) which is followed by rupturing a small patch of the cell membrane resulting in a whole-cell configuration. (Adapted from *Modern Tools of Biophysics*.[153])

This type of electrode enables a reversible conversion between ionic and electron current.[154] Figure 3.10 shows the patch-clamp procedure in whole-cell configuration where the micropipette is attached to the cell membrane. To avoid damage to the cell membrane, the tip of the patch-clamp glass micropipette needs to be fire-polished in contrast to sharp micropipettes that are used for direct penetration in intracellular recordings.[154,155] Usually, the diameter of the tip opening for patch-clamp micropipettes ranges from 1 to 3 µm.[154] This size is sufficient to achieve a cell-attached configuration which is obtained by applying low pressure to the micropipette through a syringe (Figure 3.10). As a result, a small patch of the cell membrane gets pulled into the opening of the micropipette without rupture of the cell membrane.[151] At this stage, the glass micropipette and the cell membrane form a tight seal, also termed the gigaseal because the resistance here amounts to several gigaohms. If a whole-cell configuration is intended the next step consists of rupturing the small piece of patch by repeated application of negative pressure to the pipette in order to establish a direct electrical contact with the interior of the cell.[154] Despite the breach of the cell membrane, the gigaseal is maintained. The current recordings in whole-cell configuration correspond to the activity of all voltage-gated ion channels together that are present in the cell membrane.[146,151–154] The patch-clamp technique allows two recording configurations: the voltage- and current-clamp that will be introduced in the following.

Voltage-Clamp

During voltage-clamp the aim is to clamp the membrane potential of the cell to a certain value and simultaneously record the current flow through the ion channels at this fixed potential.[146,151,152] This configuration is based on an electronic feedback system that consists of a current-to-voltage-converter, a combination of an operational and differential amplifier (Figure 3.11).[146,151,152,156,157]

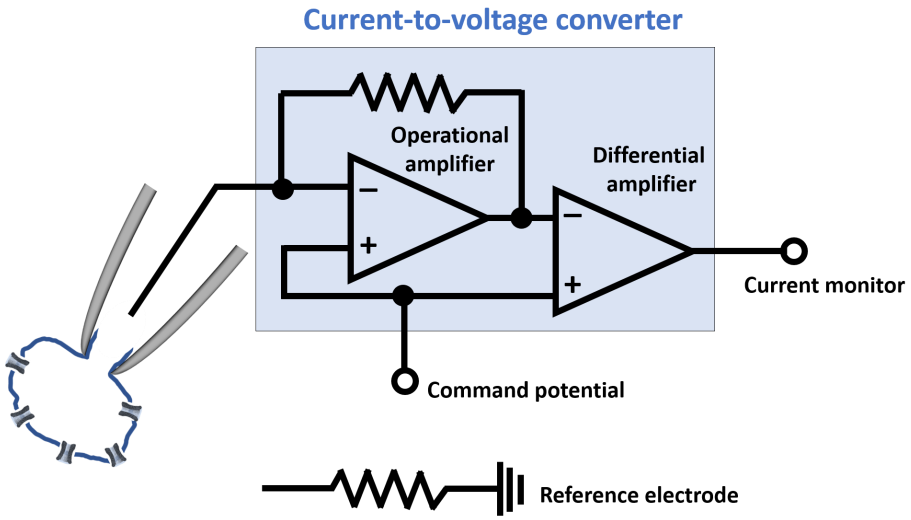

Figure 3.11: Electrical circuit applied during voltage-clamp mode in whole-cell configuration which consists of a current-to-voltage converter (a combination of an operational amplifier equipped with a megaohm resistor and differential amplifier). The circuit is complemented by a current monitor and a reference electrode. (Adapted from *Action potentials recorded with patch-clamp amplifiers: are they genuine?*[156] and *Cellular and Molecular Neurophysiology.*[146])

The operational amplifier is equipped with a megaohm resistor in a negative feedback loop. Currents in the nanoampere range can be obtained with 500 MΩ feedback resistors.[152] The operational amplifier typically has an inverting (-) and a noninverting input (+) with high input resistances so that all current is forced to flow across the feedback resistor and not into the input of the amplifier.[158–160] While clamping the membrane potential V_{m} to a certain voltage, the command potential V_{cmd} is set at the noninverting input whereas the inverting input is directly connected to the single patch-clamp electrode that is responsible for current injection and voltage-measurement.[146,151,152] The purpose of the operational amplifier is to force the membrane potential of the cell to assume the value that is chosen at the noninverting input as command potential.[146,151]

Due to the intrinsic properties of the operational amplifier, the output voltage can be considered as the difference between command potential and actual membrane potential.[151,161,162] As soon as the command potential is changed the output voltage elicits a current flow through the negative feedback resistor until V_{cmd} and V_{m} are identical.[146,151,152] Below, the concept of voltage-clamp will be explained by reference to the measurement of voltage-gated sodium channels. In the beginning, after patch-clamping the cell, the command potential is set to a resting membrane potential of -70 mV. This resting state is followed by a 100 ms depolarization step by changing the command potential from -70 to -20 mV. Since the values on both inputs of the operational amplifier do not coincide the output injects positive current into the cell until V_{m} is -20 mV.[146] The voltage-sensors of the sodium channels detect this depolarizing current and respond with an activation of the channels and the eventual flow of sodium ions into the cell.[135,146] This inward flow of positive sodium ions would usually cause a further depolarization beyond -20 mV. To keep the membrane potential at -20 mV the operational amplifier injects a negative current that compensates the sodium inward current.[146] In the end, the actual current signal that is being recorded during voltage-clamp is the negative current that has been injected by the amplifier, and that corresponds to the sodium inward current with the opposite polarity. Therefore, voltage-gated sodium channels exhibit a negative current in electrophysiological recordings. The differential amplifier functions as a current monitor since the voltage output here corresponds to the current flow in the patch-clamp electrode.[146,151,152,156]

Current-Clamp

On the other hand, a current-clamp recording allows the measurement of the membrane potential while the value of the injected current is clamped to a specific value.[146,151] The amplifier circuit which is used for current-clamp mode is given in Figure 3.12. Here, an additional feedback operational amplifier is employed in order to amplify the difference between command current and current monitor. The output voltage serves to balance out the command current and pipette current by varying the potential at the measuring electrode.[146,151,156]

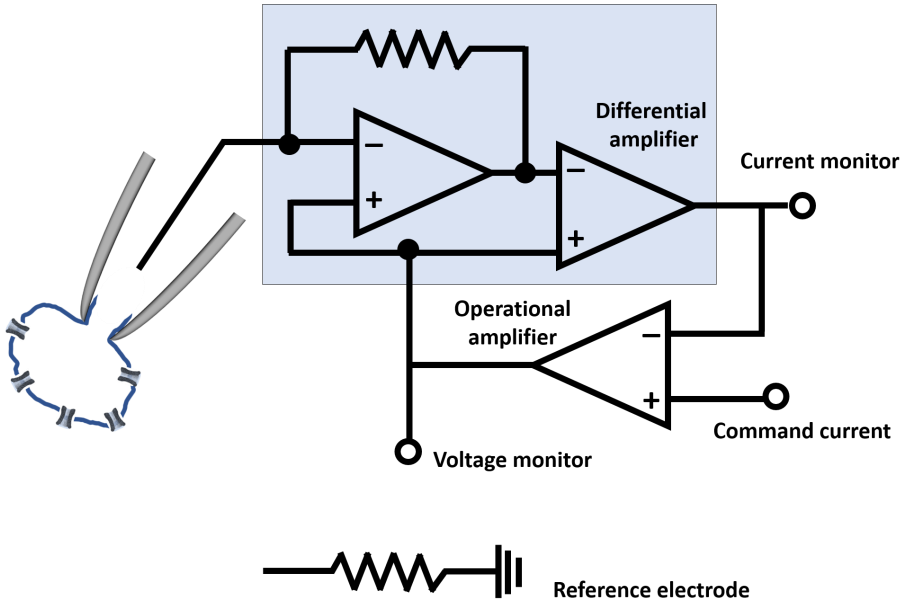

Figure 3.12: Electrical circuit applied during current-clamp mode in whole-cell configuration. Here, the circuit used for voltage-clamp mode is complemented by an additional operational amplifier. (Adapted from *Action potentials recorded with patch-clamp amplifiers: are they genuine?.*[156])

3.3 Neurostimulation

Long before the concept of present-day neurostimulation was born, several theories have been introduced to explain the electrode-electrolyte interface. According to them, the electrode-electrolyte interface can be modeled in two ways: capacitive and Faradaic charge transfer. The goal here is to transduce electric current from the electrode into ionic current in the aqueous electrolyte (Figure 3.13).[81,89,163,164]

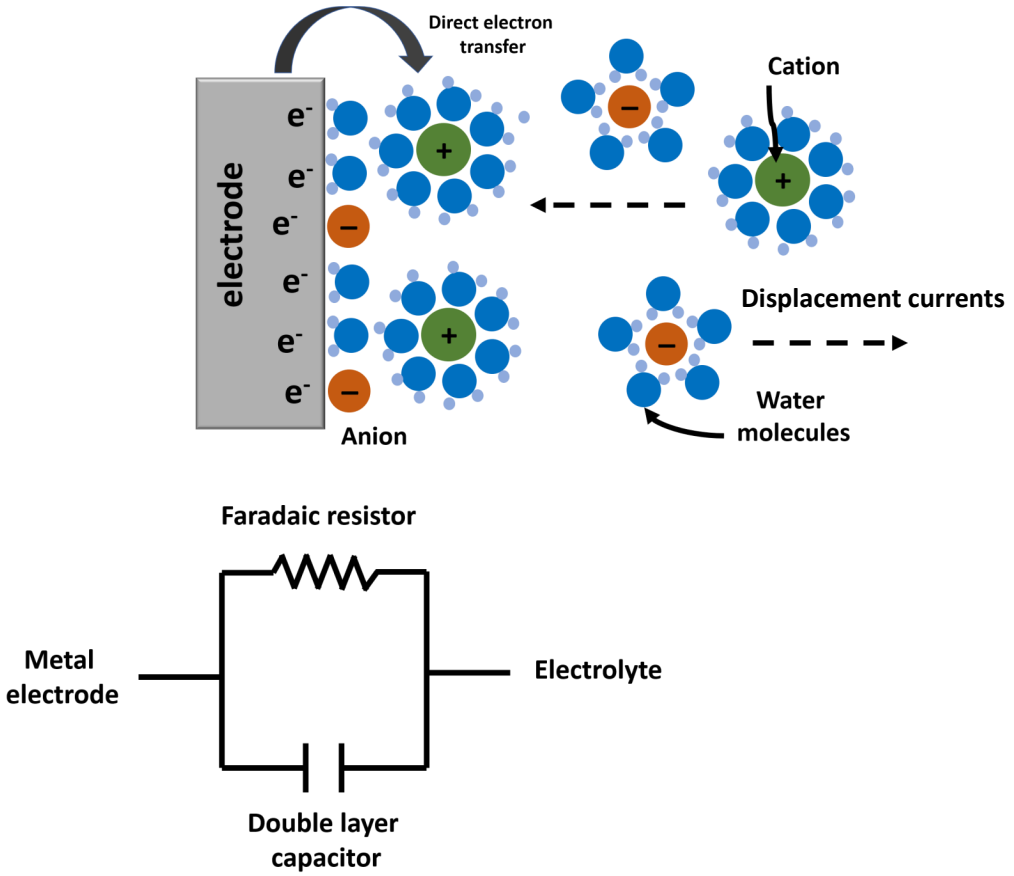

Figure 3.13: Schematic visualization of the electronic processes that occur at an electrode/electrolyte interface: Faradaic and capacitive charge transfer. During Faradaic charge injection an electron is directly transferred from the electrode, leading to the reduction of a hydrated cation in the electrolyte. Capacitive charge injection is characterized by a reversible redistribution of ionic charges in the electrolyte (displacement currents). The electrode-electrolyte interface can be modeled as an electrical circuit consisting of a double layer capacitor and a Faradaic resistor. (Adapted from *Biomaterials Science: An Introduction to Materials in Medicine.*[163])

In both cases, the stimulation is achieved by exposing the biological tissue to an electrical field generated by charge injection through the electrode.[81,89,163,164] Faradaic stimulation is characterized by oxidation and reduction reactions at nonpolarizable electrodes which involve direct electron transfer between chemical species in the electrode and electrolyte. On the other hand, capacitive charge injection through polarizable electrodes can be considered as a transient flow of electrons, unlike Faradaic processes with a steady-state current flow.[81,89,163,164] Placing an electrode into an aqueous solution elicits the formation of a capacitive double-layer at the electrode-electrolyte interface. This electrical double layer model was first proposed by Helmholtz in 1879, and its behavior resembles a capacitor with a dielectric in between two conductors, the electrolyte and the electrode.[163,165] Halide ions and polar water molecules tend to adsorb to the surface of the electrode and contribute to the charge separation at the interface (Figure 3.13).[164] Once the electrode is electrically charged, it attracts oppositely charged hydrated ionic species. This rapid redistribution which can also be designated as fast charging transient displacement current within the solution ultimately causes the depolarization of the biological tissue by changing the local charge distribution in the vicinity of the cell membrane.[89,164,166–168] At this point, it needs to be emphasized that this type of neuromodulation is considered an extracellular stimulation since the charge distribution outside of the cell is altered by the charge injecting electrode, compared to the intracellular electrophysiological techniques introduced above that artificially change the charge inside of the cell. During neurostimulation a charge-balanced stimulation is crucial.[3,89,164,169] To ensure a reversible charge injection, the cathodic stimulation phase (negative potential at the electrode initiates the flow of current from the electrode into the electrolyte) is followed by an anodic phase that reverses the direction of the current flow and reestablishes the initial state.[163] Due to this biphasic character of the stimulation, the total net charge injection is zero.[89] This concept can also be applied to electrodes that show reversible Faradaic reactions e.g., iridium oxide without degradation of the electrode material. However, there are limits to the amount of charge that is allowed to be injected for both capacitive and reversible Faradaic electrodes, as an infinitely large magnitude would result in water electrolysis, variations in the pH and electrode ablation.[89,164]

Chapter 4

Organic Semiconductors

There are several types of organic semiconductors: molecular crystals, amorphous molecular films, polymer films (e.g., P3HT (Figure 4.1)), fullerenes and carbon nanotubes.[170] They all belong to a class of carbon-based materials that feature flexibility, softness and lightweight which can be attributed to intermolecular van der Waals forces within the material.[170] Further advantages entail the possibility of fabrication on plastic substrates enabling thin and flexible devices. Most importantly, their conjugated structure with delocalized π electrons gives rise to electronic properties which are the basis for their ability to convert light into electricity by generating charge carriers upon light absorption.[171]

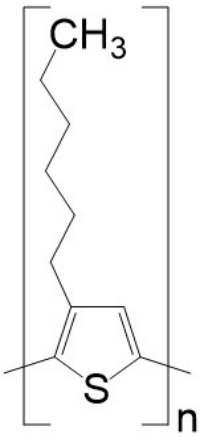

Figure 4.1: Structural formula of P3HT (poly(3-hexylthiophene-2,5-diyl)).

The π conjugated system arises due to the formation of molecular orbitals by overlap of p_z orbitals in molecules that exhibit alternating single and double bonds.[171,172] The formation of π bonds between electrons that are present in the p_z orbitals results in a "*cloud of electrons*"[171] which is delocalized throughout the conjugated molecular backbone.[171–174] According to quantum mechanics, particles including electrons can have only discrete energy values and their state can be represented mathematically via a wavefunction.[170–172,175] Figure 4.2 demonstrates the simple example of a double bonded ethene molecule that is used here as model to explain the idea of molecular orbitals, where two p_z orbitals overlap that are perpendicular to the molecular plane as indicated by dashed lines in Figure 4.2 a).[171,172,176]

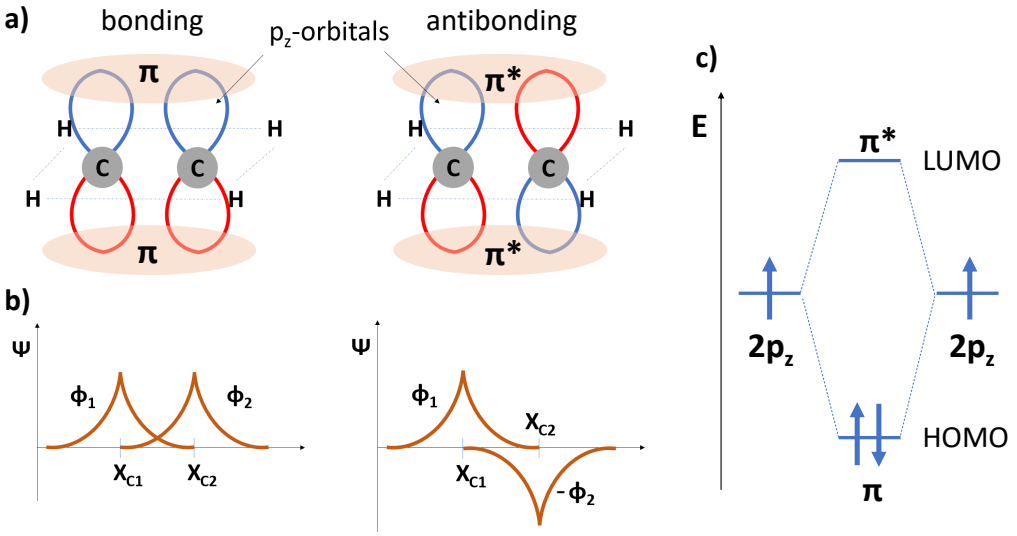

Figure 4.2: a) p_z orbitals of carbon atoms (C) in an ethene molecule that form bonding π and antibonding π^* orbitals. Electron wave functions ϕ_1 and ϕ_2 of the carbon atoms (X_{C1} and X_{C2}) are illustrated in b) (brown traces). A linear combination of these wavefunctions give either a constructive or destructive interference resulting in a bonding HOMO or antibonding LUMO molecular orbital, respectively. c) Energy level diagram of HOMO and LUMO and both atomic p_z orbitals of the carbon atoms. (Adapted from *Organic Solar Cells: Theory, Experiment, and Device Stimulation.*[172])

The wave properties allow mathematically a bonding and antibonding configuration upon the linear combination of the electron wavefunctions for each p_z orbital.[170] The constructive interference results in a bonding HOMO: highest occupied molecular orbital while a LUMO: lowest occupied molecular orbital arises due to destructive interference canceling out the wavefunctions.[170] A simple energy diagram can be drawn for both configurations, showing that both electrons originating from the p_z orbitals of the

carbon atoms fill out the HOMO level while LUMO is empty (Figure 4.2 c)). In more complex organic semiconductor structures the absorption of a photon induces the excitation of an electron from the HOMO into the LUMO level which enters the molecule into an electronic state that is considered energetically higher.[171] Organic semiconductors in their ground state can absorb light only in a specific wavelength range because the photon energy needs to be equal to or larger than the energy differences between HOMO and LUMO.[174,175,177] In inorganic semiconductors, free electron and positive (hole) charge carriers are generated upon photoexcitation.[171] This is not the case for organic semiconductors. Here, the excitation of an electron from HOMO to LUMO initiates the generation of an exciton that features an electron-hole pair bound by coulombic forces.[171,178] Excitons have a limited lifetime which means that the molecule will return to its ground state and the electron-hole pair recombines when the exciton is not dissociated into free electron and hole charge carriers. In order to facilitate a dissociation, organic photovoltaic devices combine two types of organic semiconductors: an electron donor (e.g., SQIB) and an acceptor (e.g., PC60BM (Figure 4.3)).[178,179]

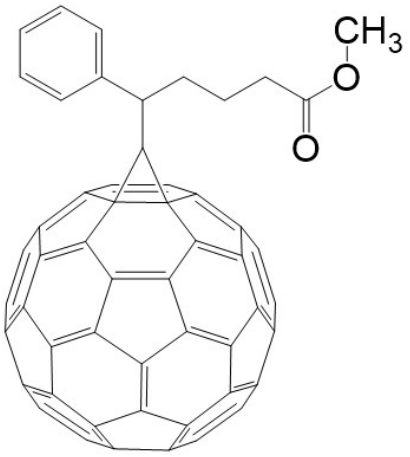

Figure 4.3: Structural formula of PC60BM ([6,6]-Phenyl C_{61} butyric acid methyl ester).

While the donor exhibits a large ionization potential *IP* (energy needed to excite an electron from the HOMO level into vacuum) the electron acceptor features a high affinity for electrons *EA* (LUMO level relative to vacuum) (Figure 4.4 a)).[178]

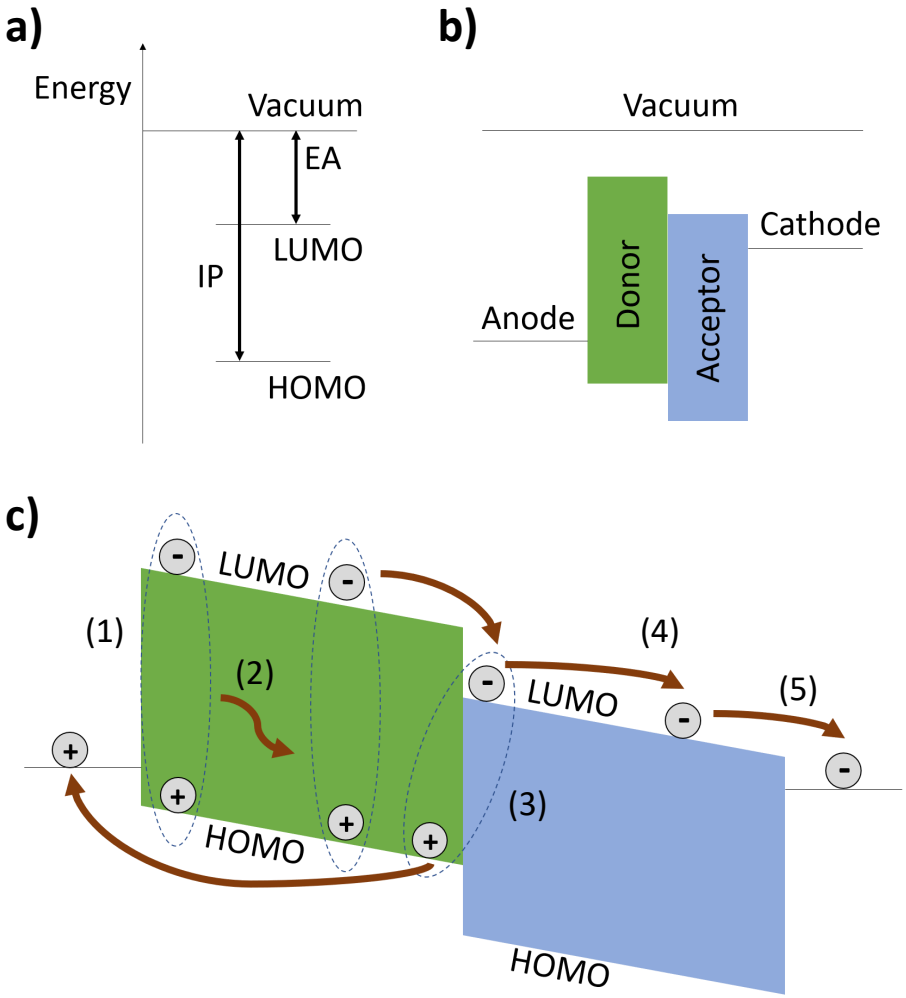

Figure 4.4: a) Energy level diagram illustrating the HOMO and LUMO levels of an organic semiconductor. *EA*: electron affinity. *IP*: ionization potential. b) Energy level diagram of a heterojunction organic photovoltaic device that consists of a donor and acceptor material sandwiched between an anode and cathode. c) Photovoltaic processes that take place in an organic photovoltaic device upon illumination: 1) Light absorption and subsequent generation of excitons. 2) Diffusion of the exciton to the donor-acceptor interface and formation of a geminate pair. 3) Exciton dissociation. 4) Transport of free charge carriers to the electrodes. 5) Charge carrier collection at the organic material/electrode interface. (Adapted from *Organic Solar Cells: Materials and Device Physics*[171], *Organic Solar Cells: Theory, Experiment, and Device Stimulation*[172] and *The future of organic photovoltaics.*[178])

To extract free charge carriers in photovoltaic devices the donor and acceptor bilayer needs to be sandwiched between two electrodes as shown in Figure 4.4.[179] The mechanistic steps that take place in an organic photovoltaic device during illumination are summarized in the following (Figure 4.4):[171,178]

1) Generation of excitons in the donor material upon light absorption [171,178]

2) Diffusion of the exciton to the donor-acceptor interface along the chemical potential gradient and subsequent formation of a charge transfer complex termed as geminate pair, an electron-hole pair bound to each other across the donor acceptor interface. Here, the exciton diffusion length, defined as the distance the exciton travels in the donor material before the electron-hole pair recombines, is a crucial parameter that needs to be considered while designing the device architecture. Bilayer devices where the donor and acceptor layers are stacked on top of each other have the disadvantage that excitons generated far away from the interface recombine since they would have to overcome a distance that is longer than their diffusion length to reach the interface, resulting in the loss of charge carriers. A solution to this problem was the development of bulk heterojunction devices. Here, the donor and acceptor materials are blended allowing a mosaic-like distribution of the two components with more contact area between donor and acceptor and shorter distances between interfaces. [171,178,179]

3) Dissociation of the exciton into free charge carriers via the transfer of the electron into the LUMO level of the acceptor material while the hole remains in the HOMO state of the donor material. By choosing the right combination of donor and acceptor material, the transfer can be made energetically favorable. The potential difference between both LUMO levels has to be larger than the exciton binding energy to ensure a dissociation. [171,178]

4) The transport of free charge carriers (electrons to cathode and holes to anodes) after dissociation is determined by drift and diffusion currents. Drift currents are characterized by the movement of hole and electron charge carriers along an intrinsic electric field usually established by selecting an anode with a high work function whereas the cathode exhibits a low work function, defined as the energy that is needed to transfer an electron from the surface of a metal into vacuum. [180,181] On the other hand, the diffusion current arises due to the movement of charge carriers along the concentration gradient in the donor and acceptor material. Since the geminate pairs contribute to a high concentration of charge carriers at the interface, the holes and electrons travel away from the heterojunction when the dissociation is completed. [171,178]

5) In the final step, the free charge carriers are extracted at the interface between organic material and an electrode. In order to have a low potential barrier at this interface, it is necessary to choose anode and cathode materials with work functions that coincide with the energy levels of the donor HOMO and acceptor LUMO, respectively. Indium tin oxide (ITO) electrodes are typically selected as anodes that fit the HOMO of P3HT. Aluminium is an example for a cathode material with a low work function that is suitable for charge collection of electrons originating from a PC60BM acceptor.[171,178]

This photovoltaic process is the core of many organic-based photovoltaic devices e.g., organic photodiodes and solar cells. However, in contrast to organic solar cells, organic photodiodes usually operate with an external electric field that facilitates the charge separation. Solar cells are intended for harvesting light to generate electricity whereas organic photodiodes constitute the basis for photodetectors and sensors.[182]

Organic semiconductors suffer from short exciton diffusion lengths and low charge mobilities that promote charge recombination.[171,183] Another phenomenon that affects organic semiconductors is the formation of space charges (charge accumulation) that occur when there is a large discrepancy between the mobilities of electron and hole charge carriers. When electrons travel faster to the cathode due to their higher mobility, this will cause them to accumulate at the semiconductor-cathode interface.[171] A growing number of studies demonstrate that the space charge effect can be exploited to develop a new generation of optoelectronic devices by combining an organic semiconductor with an insulator.[115–127] Photoexcitation does generate charge carriers within the organic material. However, the insulator functions as blocking layer, hindering a charge extraction resulting in a charge accumulation at the interface between insulator and semiconductor. These space charges polarize the insulator and give rise to displacement currents which can be measured as transient photocurrent responses. This device concept is being adapted for organic artificial retinas. The first devices of these type were reported by Narayan et al. and Lanzani et al. who combined P3HT thin films supported on ITO with a physiological electrolyte solution. Their experiments confirmed transient displacement currents within the electrolyte upon photostimulation that elicited action potentials in degenerated retina.[72,74,119]

Chapter 5

Organic Bioelectronic Interfaces I: Passive Photostimulation

This chapter presents a set of experiments that were conducted on squaraine-based artificial photoreceptors during the first phase of the thesis, which consisted of a proof of principle study with following objectives that will each be addressed in the upcoming subchapters:[1]

⇒ **Subchapter 5.1**
Characterization of the squaraine photosensor to learn more about the morphological and optical properties of the blend organic semiconductor thin film, that need to be taken into consideration while discussing the results obtained for the adhesion of the N2A cells to the device, followed by photostimulation experiments and stability tests. Experimental details are summarized in the experimental section.

⇒ **Subchapter 5.2**
Here, the focus is on N2A cells and quantitative evaluation of their growth behavior on the SQIB:PC60BM blend film.

⇒ **Subchapter 5.3**
Characterization of the electrical properties of N2A cells grown on the photoreceptor device.

[1]Parts of this chapter have been published in: "*Photoelectrical Stimulation of Neuronal Cells by an Organic Semiconductor-Electrolyte Interface*".[184]

⇒ **Subchapter 5.4**
After a short introduction into the experimental setup that was used during photostimulation measurements, the photocurrent responses of SQIB:PC60BM devices inserted into an electrolyte solution are presented here.

⇒ **Subchapter 5.5**
Here, the aim is to show how the N2A cells respond to the photocurrents introduced in section 5.4, including recordings of N2A cells in voltage- and current-clamp configuration.

⇒ **Subchapter 5.6**
The chapter is finalized by revealing results obtained during stability tests via atomic force microscopy with the goal to evaluate the long term stability of the SQIB:PC60BM photoactive layer in ambient and aqueous environment under dark and illuminated conditions.

5.1 Characterization of the SQIB:PC60BM Photoreceptor

The squaraine-based photosensor was fabricated via solution processing. SQIB was blended with PC60BM, giving a mixture ratio of 1:1 (total concentration of 12 mg/mL) and spin coated onto transparent ITO/glass electrodes. The schematic device architecture is illustrated in Figure 5.1 a). As the devices were intended for biological application, the samples had to be treated thermally at 180 °C or 120 °C (following chapters) for two hours in order to be sterilized. The annealing step led to a unique crystallization of the SQIB:PC60BM blend film. The optical microscopy images taken with crossed polarizers, shown in Figures 5.1 b), c) and d), revealed two different birefringent motifs. Throughout this thesis, the golden areas are referred to as platelets, and the colorful regions are termed ferns. Combined X-ray diffraction and local optical spectroscopy investigations showed that the fern and platelet regions consist of monoclinic and orthorhombic crystals, respectively.[185] Interestingly, the platelets were interspersed with numerous elongated pinholes which appeared dark in polarized microscopy images. Moreover, these pinholes had a parallel orientation within the same platelet domain, and in addition, the orientation varied for every single domain. The fern regions also lacked homogeneity, having large dark voids between individual branches. Because these pinholes and voids were non-responsive to polarized microscopy imaging, it is most likely that the blend film comprises a second amorphous layer underneath the crystalline surface.

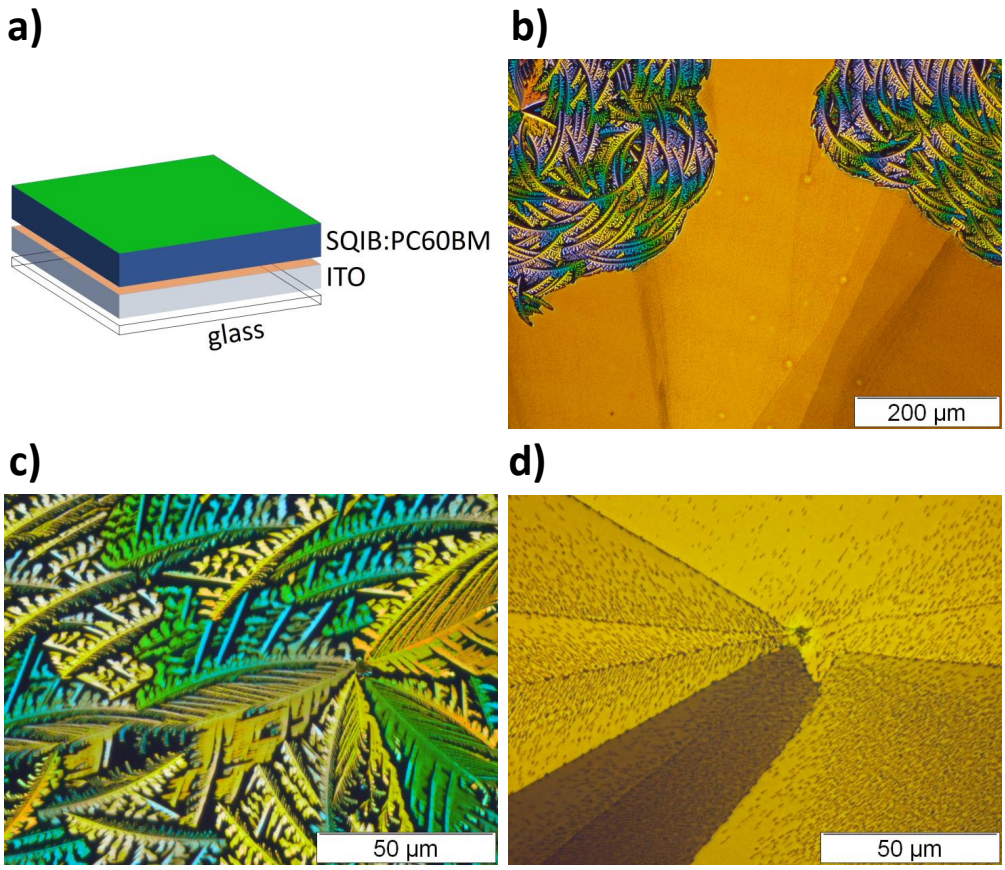

Figure 5.1: Characterization of SQIB:PC60BM(1:1)/ITO/glass (180 °C, 2h) artificial photoreceptor. a) Schematic illustration of the device architecture: ITO/glass substrates are spin coated with a SQIB:PC60BM blend solution and subsequently annealed resulting in a thin film on top of the ITO layer. b) Optical microscopy image of the SQIB:PC60BM blend film surface (Olympus BX41), recorded in reflection with crossed polarizers reveals two birefringent crystalline structures: c) ferns and d) platelets. c) Magnified optical microscopy image of ferns that show thick branches with dark non-birefringent areas in-between. d) Platelet structures contain several domains with pinholes (dark spots) distributed over the complete area.

To test this hypothesis, it was necessary to conduct advanced scanning and transmission electron microscopy (SEM and TEM) experiments (Figures 5.2 and 5.3). Indeed, according to images collected via SEM, the pinholes showed sharp edges, uncovering unique tesselated mosaic-like structures which even shined through the above rather smooth homogenous platelet layer, strongly indicating that the SQIB:PC60BM blend film undergoes a phase separation upon annealing (Figures 5.2 a) and b)). The same structures could be identified on floating samples fabricated by spin casting the blended mixture onto a sacrificial LiF layer supported on glass substrates, excluding the possibility of the structures revealed by the pinholes being bare ITO (Figure 5.2 c)). Additional cross section images (Figure 5.2 d)) of the device architecture recorded via transmission electron microscopy revealed an ITO electrode fully covered with an approximately 44 to 78 nm thick SQIB:PC60BM layer exhibiting sharp edges that are characteristic for the pinholes as shown in Figures 5.2 a) and b). The observation that the layer exposed by the pinholes is thinner (approximately 44 nm, see Figure 5.2 d)) supports the initial assumption that the pinholes are exposing a second layer (most likely PC60BM) underneath the smooth platelet structure. The same techniques were used to study the morphology of the fern areas which consisted of large SQIB:PC60BM branch motifs separated by a second layer with numerous holes revealing bare ITO (Figures 5.3 a) and b)). Similar exposed ITO areas were also found in transmission electron microscopy images of the device cross section (Figure 5.3 d)). Areas that showed bare ITO were noticeable as holes in floating SQIB:PC60BM fern samples shown in Figure 5.3 c). To verify the origin of the second layer in-between the dark branch structures, it was necessary to record a scanning electron microscopy image of a PC60BM layer (6 mg/mL PC60BM solution spin coated onto ITO/glass substrates and annealed at 180 °C for 2h). Upon comparison of the images 5.3 a) and e) it can be concluded that the second layer separating the branches consists of amorphous PC60BM. This conclusion is also supported by the optical microscopy image in Figure 5.1 c) where these areas appear dark and are non-responsive to polarized light.

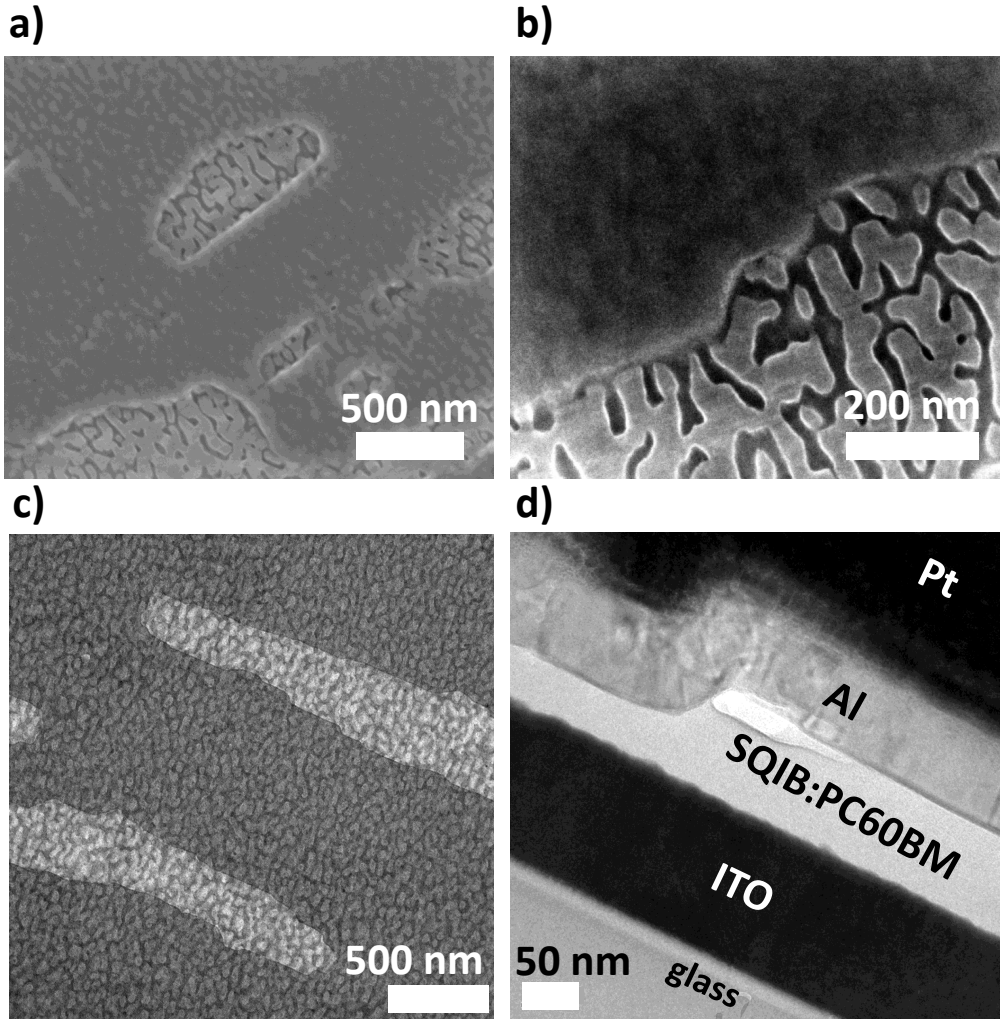

Figure 5.2: Electron microscopy images of platelet regions on SQIB:PC60BM(1:1)/ITO/glass (180 °C, 2h) devices.
a) Scanning electron microscopy image giving an overview of platelet structures with visible pinholes spread over the layer. Two structural motifs are noticeable. The pinholes expose a mosaic-like domain which is covered by a flat smooth second layer on top (acceleration voltage: 2 kV, probe current: 0.17 nA). b) Magnified scanning electron microscopy image of an interface between smooth layer and pinholes reveals edges around the pinholes (acceleration voltage: 5 kV, probe current: 0.34 nA). The structures that were found in the pinholes are distributed over the complete platelet area as evidenced in the transmission electron microscopy image shown in c). d) Lamella of the cross section recorded via transmission electron microscopy proving that the ITO electrode is fully covered and that the interface between pinhole and the residual layer is characterized by a step with a height difference of about 40 nm. Images c) and d) were recorded via transmission electron microscopy. Scanning electron microscopy images were recorded with a FEI Helios NanoLab 600i microscope system. (Samples were prepared by Oliya S. Abdullaeva. Lamella preparation and image recording were conducted by Angelika Maderitsch.)

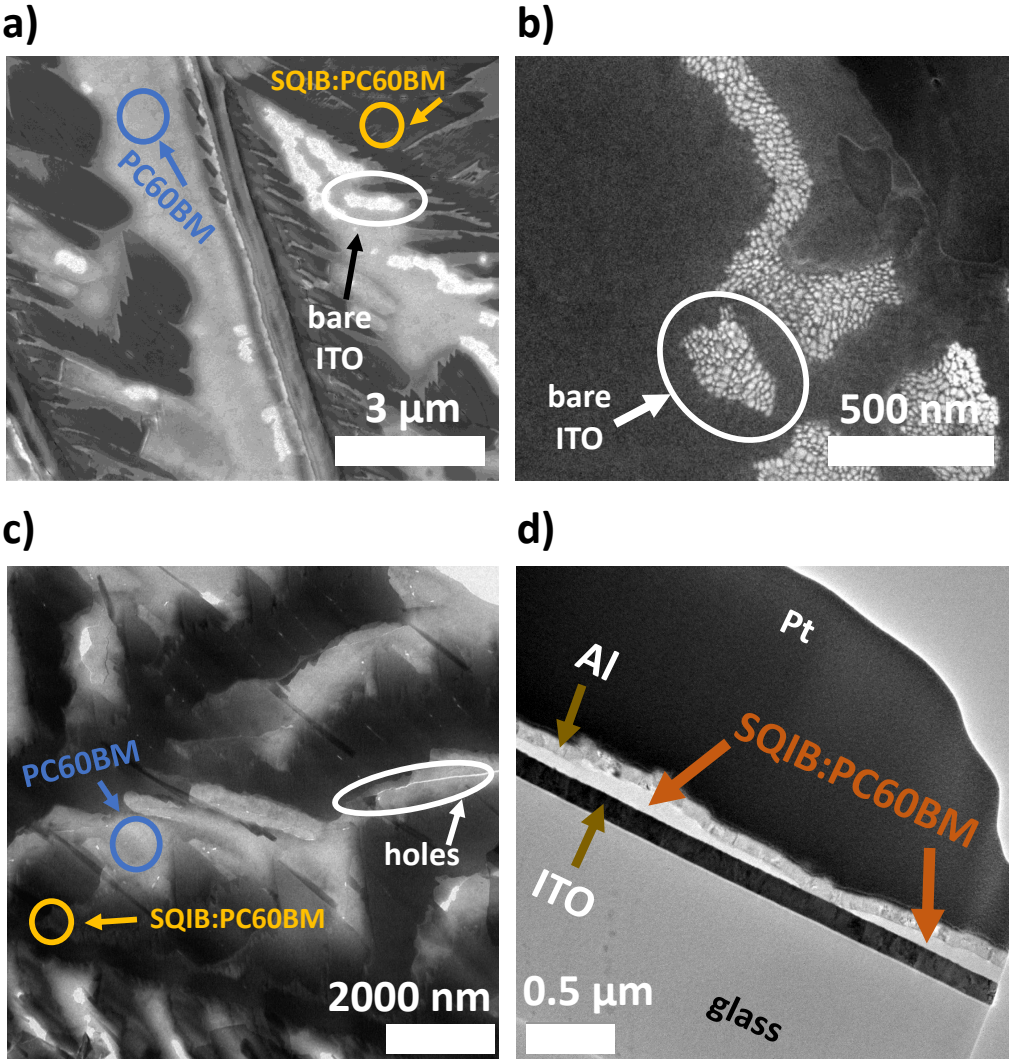

Figure 5.3: Electron microscopy images of fern regions on SQIB:PC60BM(1:1)/ITO/glass (180 °C, 2h) devices.
a) Scanning electron microscopy image showing an overview of fern structures with bright spots between individual branches (SQIB:PC60BM domains) that appear darker compared to the residual areas. In addition, the dark branches are separated by a thin layer that resembles PC60BM (see Figure 5.3 e)) (acceleration voltage: 2 kV, probe current: 0.17 nA). b) Magnified scanning electron microscopy image of the bright spots noticeable in the fern regions, resembling bare ITO (acceleration voltage: 15 kV, probe current: 0.17 nA). c) Transmission electron microscopy image of fern branches that exhibits similar features that are also noticeable in a) and b). Dark areas can be attributed to SQIB:PC60BM domains that are surrounded by a PC60BM layer. Areas exposing bare ITO in images a) and b) appear as holes in c). d) Lamella of the device cross section shows how the thickness of the SQIB:PC60BM layer varies strongly. At the thickest point the SQIB:PC60BM layer has a thickness up to 145 nm while the ITO electrode is uncovered in other regions. Images c) and d) were recorded via transmission electron microscopy. Scanning electron microscopy images were recorded with a FEI Helios NanoLab 600i microscope system. (Samples were prepared by Oliya S. Abdullaeva. Lamella preparation and image recording were conducted by Angelika Maderitsch.)

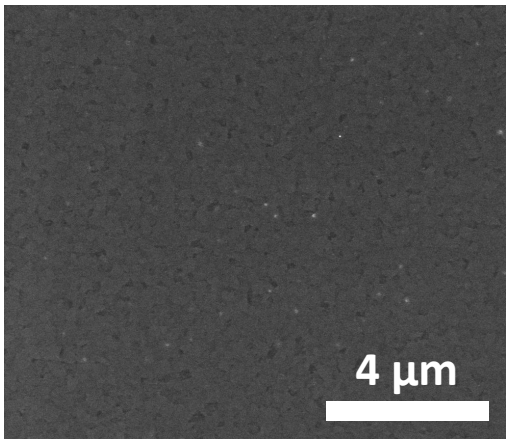

Figure 5.3 e): Scanning electron microscopy image of a PC60BM(6 mg/mL)/ITO/glass (180 °C, 2h) sample showing the morphology of a PC60BM thin film layer (acceleration voltage: 2 kV, probe current: 0.17 nA). The image was recorded with a FEI Helios NanoLab 600i microscope system. (Sample was prepared by Oliya S. Abdullaeva and the image recorded by Angelika Maderitsch.)

UV/Vis spectroscopy was used to learn more about the optical properties of the fern and platelet structures which were randomly distributed over the sample. The size of the region that was selected for the measurement was 1.85 mm^2. The resulting spectra are summarized in Figure 5.4: a) platelet-rich and b) fern-rich, showing four peaks positioned around 730, 658, 580 and 530 nm. The peak ratio of the humps at 658 and 730 nm varied strongly, depending on whether the region of interest consisted mostly of ferns or platelets. Furthermore, the signal around 530 nm was more conspicuous for the fern-rich regions. According to spatially resolved absorbance spectra of individual platelets (Figure 5.4 a)) and ferns (Figure 5.4 b)), the macroscopic spectra are the result of superpositioning these two textural motifs. The shoulder mentioned above, around 530 nm, can be attributed to the ferns that exhibit the highest absorbance for this wavelength. On the contrary, platelets show a salient peak around 730 nm which explains the strong signal of platelet-rich areas at this wavelength. Absorbance spectra also allow assertions about the molecular orientation of small organic semiconductor molecules within thin films. Aromatic molecules exhibit the tendency to assemble into aggregates due to electrostatic attraction, termed H- and J-aggregation. H-aggregates are characterized by a side-by-side assembly and J-aggregates are formed when monomers are orientated head-to-tail.[186] The aggregates show a different absorbance behavior compared to the monomer.

H-aggregation causes a shift of the absorption band into the blue region of the spectrum whereas the J-aggregates are noticeable by a red-shift.[186–188] The previously mentioned study of SQIB-alone devices found a direct correlation between optical properties, crystal structure, and surface morphology.[185] The findings show that the blue-shifted absorbance peaks can be attributed to an H-type aggregation with a monoclinic structure whereas red-shifted signals originate from J-aggregates forming orthorhombic crystals. Moreover, a Davydov-splitting was evident in the absorbance spectra of both aggregates.[185] These experiments were further complemented by EQE recordings where the SQIB:PC60BM was interfaced with an electrolyte. The spectral photocurrent resulting from the photostimulation of a SQIB:PC60BM photoactive layer - containing approximately the same amount of ferns and platelets - through the electrolyte is shown in Figure 5.4 c). Although the obtained EQE values were quite low, the spectral distribution of the photocurrent strongly reflected the absorbance behavior of the photoactive layer. Both squaraine and PC60BM domains contributed to the photocurrent for wavelengths ranging from 520 to 760 nm and smaller than 500 nm, respectively. Images of the SQIB:PC60BM film taken after the EQE experiment showed signs of degradation, most likely due to ablation of the blend film (Figure 5.4 d)). However, because large parts of the layer were intact, it is possible that capacitive currents at the semiconductor/electrolyte play a significant role here.

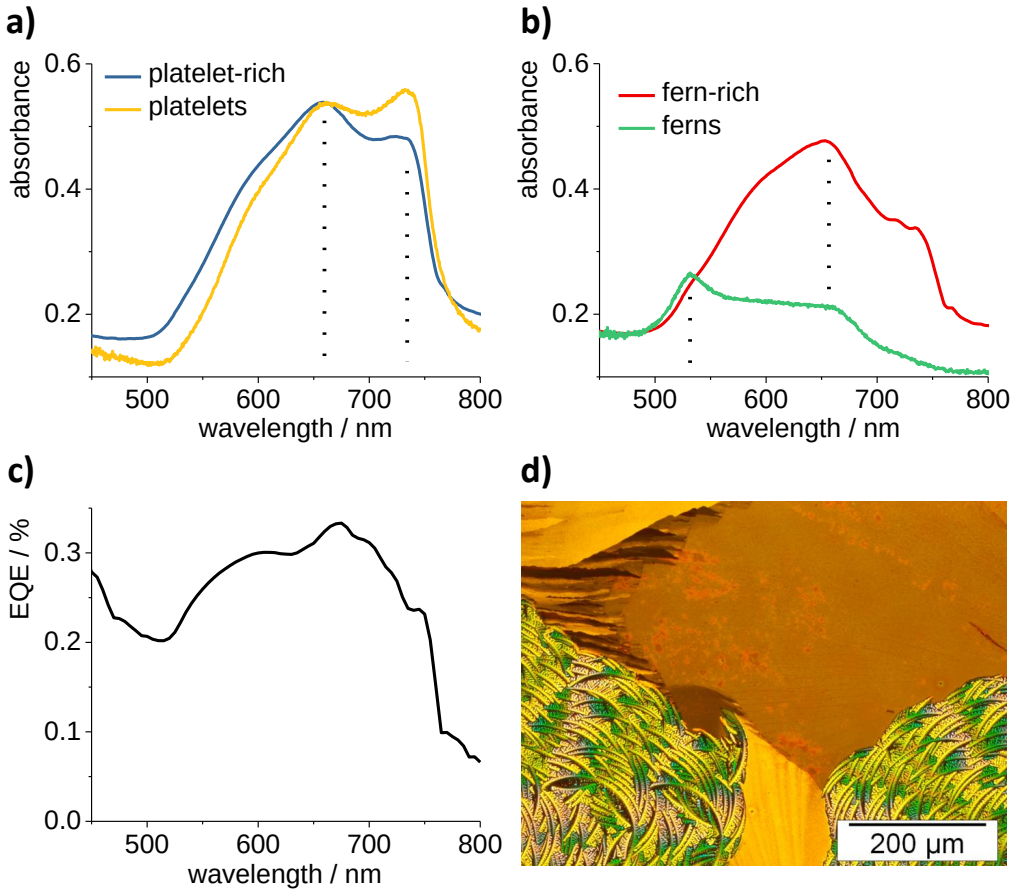

Figure 5.4: Optical properties of SQIB:PC60BM(1:1)/ITO/glass (180 °C, 2h) devices. a), b) Macroscopic absorbance spectra showing absorbance behavior of platelet-rich (blue trace) and fern-rich (red trace) regions (referenced to air): sample area of 1.85 mm^2. Spatially resolved spectra (referenced to air) of fern (green trace) and platelet (yellow trace) structures. Dotted lines mark humps at approximately 530 nm, 658 nm, and 730 nm. c) Photocurrent response recorded via EQE measurement of photoactive layer interfaced with standard Ringer's solution. d) Polarized optical microscopy image (Olympus BX41) recorded in reflection with crossed polarizers of a SQIB:PC60BM(1:1)/ITO/glass device taken after completed EQE measurement showing several damaged platelet areas. (Samples were prepared by Oliya S. Abdullaeva and spatially resolved absorbance spectra were recorded by Frank Balzer.)

5.2 Cell Growth

The intimate attachment of bioelectronic devices to biological tissue is crucial to ensure long-lasting applicability. Therefore, the first step was to evaluate the cell adhesion of the N2A cells to the device surface. During the cultivation, the SQIB:PC60BM samples were covered with a cell culture medium containing N2A cells and further incubated for three days (Figure 5.5). The incubation was discontinued by removing the samples from the culture medium and placing them into a physiological standard Ringer's solution. N2A cells that had adhered sufficiently to the surface survived the insertion into the Ringer's solution while cells that could not attach were washed away or drifted on top of the device surface. Here, the extent of the adhesion was determined by differential interference contrast (DIC) microscopy (Figure 5.5). Exemplary images showing N2A cells grown on ferns and platelets can be found in Figures 5.5 a) and b). The number of adhered N2A cells was calculated for fern and platelet regions, respectively. Interestingly, the fern regions showed a higher number of N2A cells, approximately 150 cells per mm^2 compared to 40 per mm^2 for the platelet areas (Figure 5.5 c)). The most salient observation was the fact that the adhesion of the N2A cells was successful even without an additional adhesion promoter. Even though certain organic semiconductors are considered biocompatible, they are hydrophobic and therefore usually require additional treatment with ionic polyamino acids before the cultivation of cells or neurons.[189] Negatively charged proteoglycans, glycolipids, and glycoproteins, key components of the cell membrane interact electrostatically with the positive charge of the ionic polyamino acids e.g., poly-L-lysine, poly-D-lysine, and poly-L-ornithine.[189] This additional coating improves the cell adhesion, but it can also be vulnerable to degradation due to digestion by some types of cells.[189] Additionally, these ionic polyamino acid layers might disrupt the intended signaling between organic semiconductor and cell. Although the use of polycationic coatings is common, they can be avoided by optimizing the film morphology.[189] As was shown by Lensen et al., micropatterning poly(ethylene glycol) and perfluorinated polyether instead of merely flat films supports cell adhesion even without an adhesion promoter.[189,190] The cell growth is dependent on the nanotopography rather than the chemical composition. Indeed, a comprehensive investigation by Gentile et al. concluded that moderately rough substrates with large fractal dimensions are highly beneficial for direct cell adhesion

and growth.[191] The findings in this present work demonstrate that this is also the case for squaraine-based devices. The highly textured crystalline SQIB:PC60BM blend film ensures an adequate topography for a direct proliferation of N2A cells. The difference in cell adhesion for fern and platelet regions can be affiliated to the roughness. Fern structures are ten times rougher than platelets although both have the same chemical composition, as was revealed by AFM recordings (Figure 5.6).

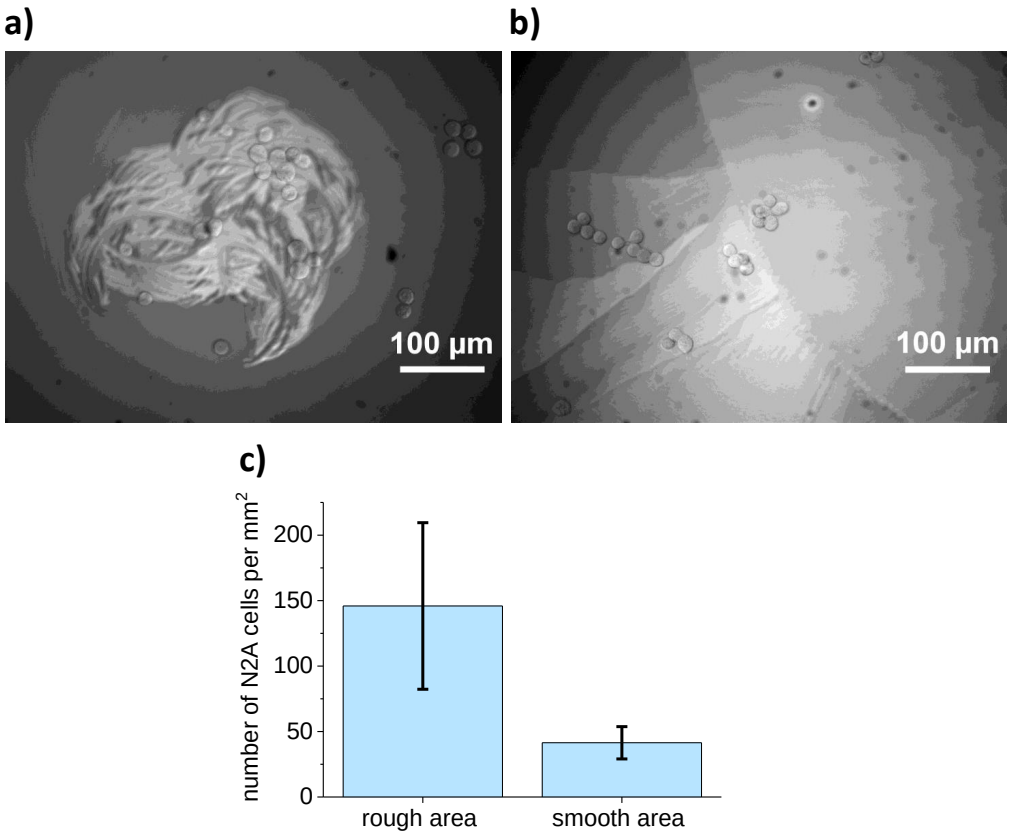

Figure 5.5: Differential interference contrast (DIC) microscopy images of N2A cells grown on SQIB:PC60BM(1:1)/ITO/glass (180 °C, 2h) devices: a) N2A cells attached to fern areas. b) N2A cells grown on platelet regions. c) The number of N2A cells grown on ferns and platelets per mm ^{2}. The cell adhesion was evaluated for four samples in total, 31 different device areas were recorded per sample. Error bars are standard deviations.

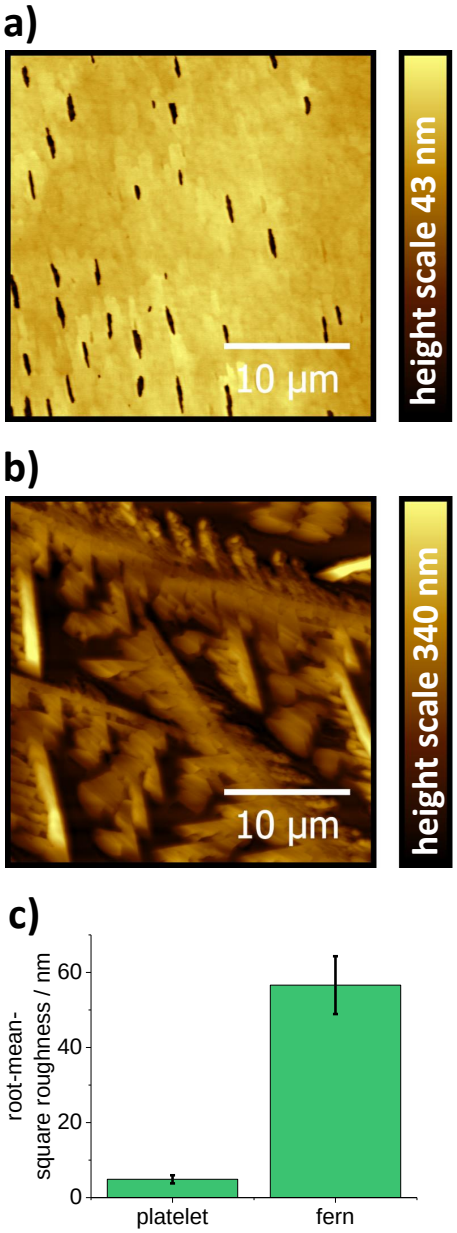

Figure 5.6: Atomic force microscopy measurements in contact mode of a) platelet and b) fern structures on SQIB:PC60BM(1:1)/ITO/glass (180 °C, 2h) devices. The recordings were conducted on an Agilent 5420 SPM/AFM microscope with ContAl-G tips (Budget Sensors: resonant frequency: 13 kHz, force constant: 0.2 N/m). The pinholes that were found for the platelet regions are also visible in the AFM images in a). Fern branches described in polarized optical microscopy images are also reflected in b). c) Average root-mean-square roughnesses for respective regions. In total, three platelet and four fern areas were recorded. Error bars represent standard deviations. Images were analyzed with Gywddion software.[192,193]

5.3 Characterization of Voltage-Gated Ion Channels in N2A Cells

After ensuring a sufficient cell adhesion, the electrical properties of the N2A cells had to be tested via artificial depolarization experiments (Figure 5.7). The experiments were conducted in the dark and entailed an application of depolarizing voltage steps to the N2A cell by artificial charge injection through the patch-clamp electrode. The depolarization induced fast negative currents which peaked within one millisecond after the voltage step and that can be assigned to activated sodium channels and slower positive currents, revealing that the N2A cells also have functioning potassium channels. The SQIB:PC60BM device did not impair the functionality of the voltage-gated ion channels. This test was also important to determine the depolarization threshold that is required to activate sodium channels. A net depolarization of 60 mV induced a minor negative inward sodium current. A maximum current of over 400 pA was obtained upon a larger net depolarization of 80 and 100 mV. The earliest potassium currents appeared for an 80 mV net depolarization.

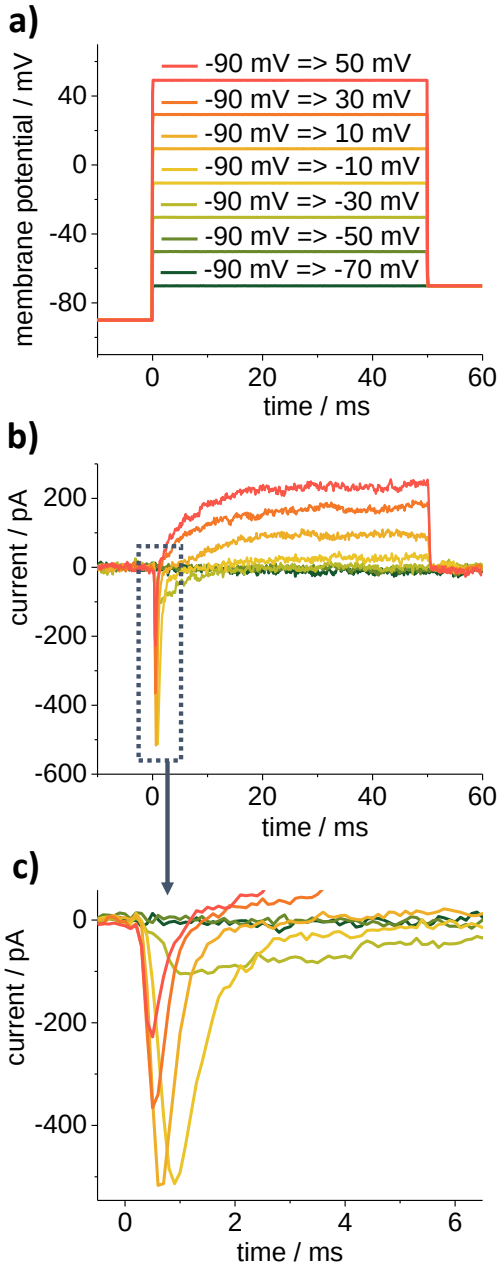

Figure 5.7: Artificial depolarization test conducted in the dark on a N2A cell grown on a SQIB:PC60BM(1:1)/ITO/glass (180 °C, 2h) device. A variety of 50 ms artificial depolarization pulses were applied to the N2A cell as shown in a). Figure b) gives an overview of negative sodium inward and positive potassium outward currents measured in voltage-clamp mode. A close-up of the sodium currents induced by the artificial depolarization can be found in c). All recordings were measured in standard Ringer's solution.

5.4 Transient Photostimulation Experiments

So far, there have been no studies with a focus on squaraine-electrolyte interfaces. To characterize the electrical response of this kind of devices, a photocurrent measuring technique needed to be implemented during this thesis.[72] Necessary to that end was the employment of the patch-clamp recording electrode and amplifier (Figure 5.8 a)). The SQIB:PC60BM devices were placed in an electrolyte bath, the Ringer's solution. In this floating condition, the patch-clamp micropipette, also filled with Ringer's solution, was held approximately 3 µm above the surface of the blend film without the tip of the micropipette directly touching the device. The exact position of the pipette was monitored by optical microscopy. Due to the small diameter of the pipette opening at the tip (1.5 µm), it was possible to measure the local photocurrent for fern and platelet regions separately on one device. To close the electrical circuit, a second Ag/AgCl electrode was immersed into the Ringer's solution and positioned at the edge of the electrolyte bath beyond the reach of the sample. A 150 W xenon high stability lamp functioned as a light source with an enclosed Polychrome V monochromator. The light was guided through a Till Photonics quartz fiber to a 20x Leica objective and eventually across the electrolyte onto the sample (Figure 5.8 a)). Additional experimental details can be found in the experimental section.

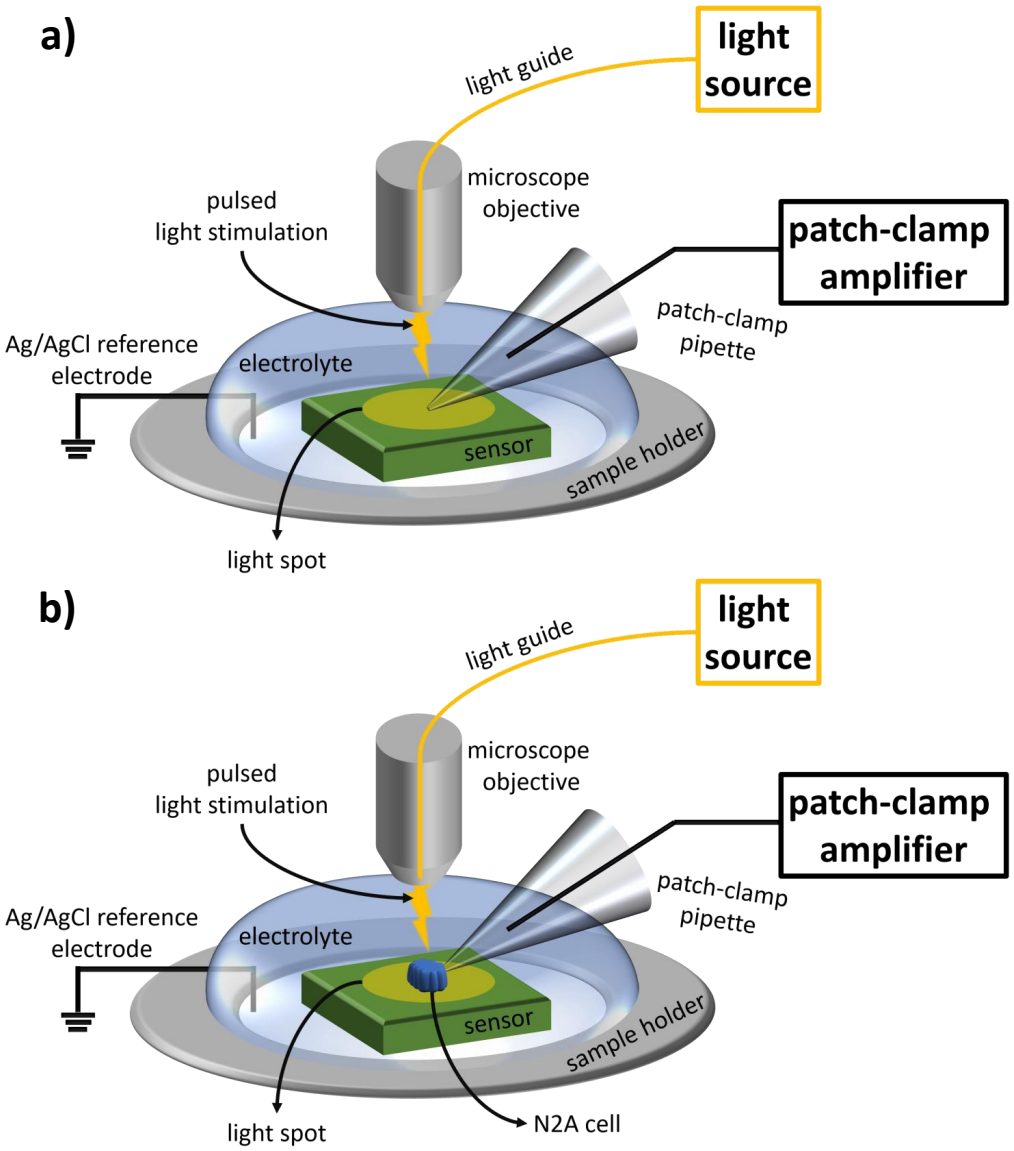

Figure 5.8: Schematic illustration of the experimental setup that was used for all a) transient photocurrent and b) patch-clamp recordings. The sample holder consisted of a Teflon ring where the middle was closed with a glass plate. The photosensor was placed onto the glass and covered with the electrolyte (Ringer's solution). The devices shown in this chapter were photostimulated from the top through the microscope objective via a light guide across the electrolyte. A Leica microscope objective (20x or 40x) was immersed into the electrolyte to monitor N2A cells during patch-clamping and to observe the device surface and the tip of the patch-clamp electrode. The 20x water-immersion objective was used to record images of the N2A cells and light spots. During all measurements, an Ag/AgCl reference electrode was placed into the electrolyte without touching the sensor. a) During transient photocurrent recordings, the tip of the patch-clamp pipette was fixed into the center of the light spot and approximately 3 µm above the device surface. b) Patch-clamp recordings entailed attaching the patch-clamp electrode to a single N2A cell that was located in the middle of the light spot.

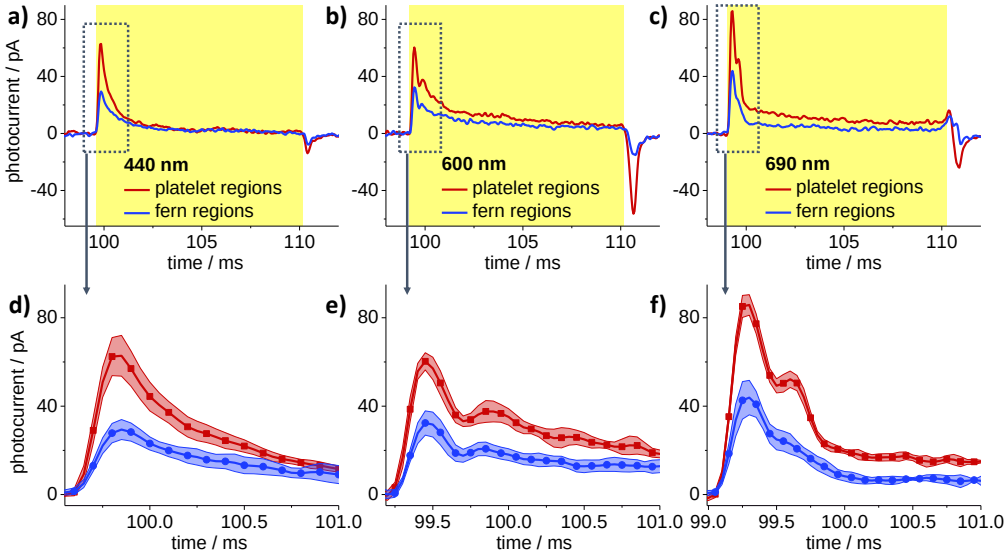

Figure 5.9: Transient photocurrent measurements of platelet (red current trace) and fern (blue current trace) regions on SQIB:PC60BM(1:1)/ITO/glass (180 °C, 2h) devices at three different wavelengths using the 150 W xenon high stability lamp, 10 ms light pulse: a)/d) 440 nm (0.17 mm^2 light spot size, 1.75 mW), b)/e) 600 nm (0.06 mm^2 light spot size, 0.9 mW) and c)/f) 690 nm (0.05 mm^2 light spot size, 0.39 mW). Shaded areas are standard deviations and represent current responses of four platelet and five fern regions. The lower row shows a close-up of the photoinduced ON-peak currents.

Figure 5.9 shows the recorded photocurrents at 440 nm, 600 nm and 690 nm for fern and platelet regions, respectively. In general, all observed current curves exhibited very fast positive ON- and negative OFF-transient peaks upon stimulation with 10 ms light pulse trains. A further similarity was a negligible positive steady-state current. Interestingly, the platelet regions generated a larger photocurrent as evidenced by higher ON-current peak amplitudes at the onset of the light pulse. Secondly, there was a decrease in the negative discharging OFF-current peak indicating that a charge-transfer occurs to some extent during the illumination. However, direct electron injection from the organic semiconductor should be avoided as this will lead to a gradual ablation of the material and the production of toxic byproducts e.g., hydrogen peroxide, singlet oxygen or superoxide radicals.[88] Therefore, the magnitude of the steady-state current should be as low as possible for organic materials. To ensure a safe neuronal stimulation, a capacitive charge injection via displacements currents is the most suitable approach. Indeed, the results presented here prove that capacitive coupling can be realized for squaraine-electrolyte interfaces.

The ON- and OFF-current transients measured by the patch-clamp electrode are caused by the accumulation of photogenerated charge carriers, space charges, in the semiconductor triggering a rapid redistribution of ionic species in the electrolyte and a subsequent formation of a Helmholtz electric double layer at the semiconductor-electrolyte interface. A systematic investigation of the ON-current peak for various light intensities revealed a nonlinear dependency on the illumination intensity (Figures 5.10 and 5.11). When a photovoltaic device exhibits a nonlinear behavior, increasing the light intensity does not result in an equal increase of the photocurrent.[194,195] Additional measurements of SQIB-and PC60BM-alone devices demonstrated that the amplitude and polarity of the transient photocurrents can be regulated by the respective sample configuration (Figure 5.12). Upon omission of PC60BM, thin films based only on the donor material SQIB showed significantly lower current signals compared to previously reported SQIB:PC60BM blend films. Conversely, an acceptor-only layer fabricated from a 6 mg/mL PC60BM solution resulted in a transient photocurrent at 440 nm with a negative polarity indicating an accumulation of positive ionic charges at the organic semiconductor-electrolyte interface.

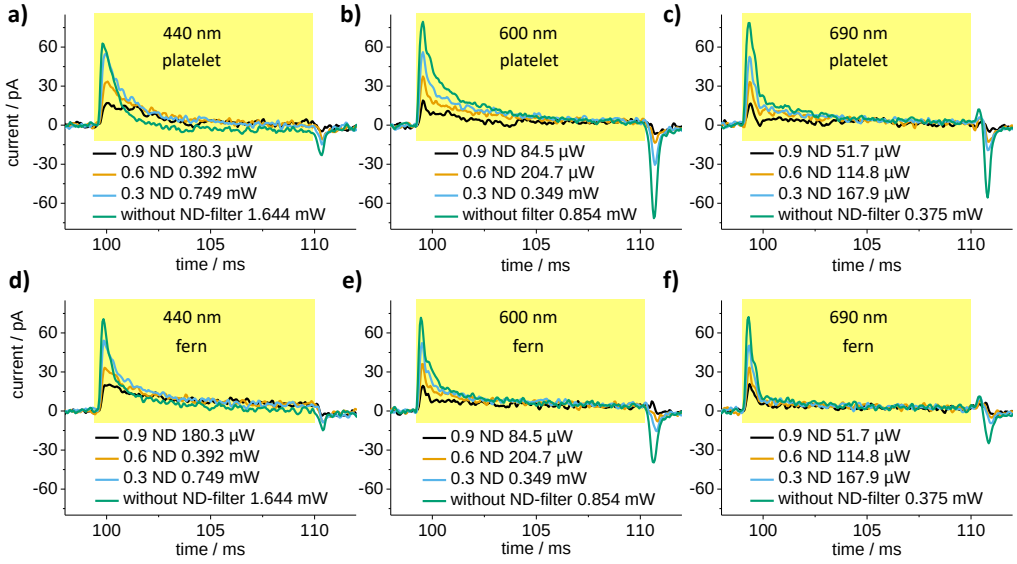

Figure 5.10: Transient photocurrent measurements of platelet (upper row) and fern regions (lower row) on SQIB:PC60BM(1:1)/ITO/glass (180 °C, 2h) devices at three different wavelengths using the 150 W xenon high stability lamp: a)/d) 440 nm (0.17 mm^2 light spot size, 1.75 mW), b)/e) 600 nm (0.06 mm^2 light spot size, 0.9 mW) and c)/f) 690 nm (0.05 mm^2 light spot size, 0.39 mW). Furthermore, the light power was gradually decreased with three types of ND-filters: 0.3 ND, 0.6 ND and 0.9 ND.

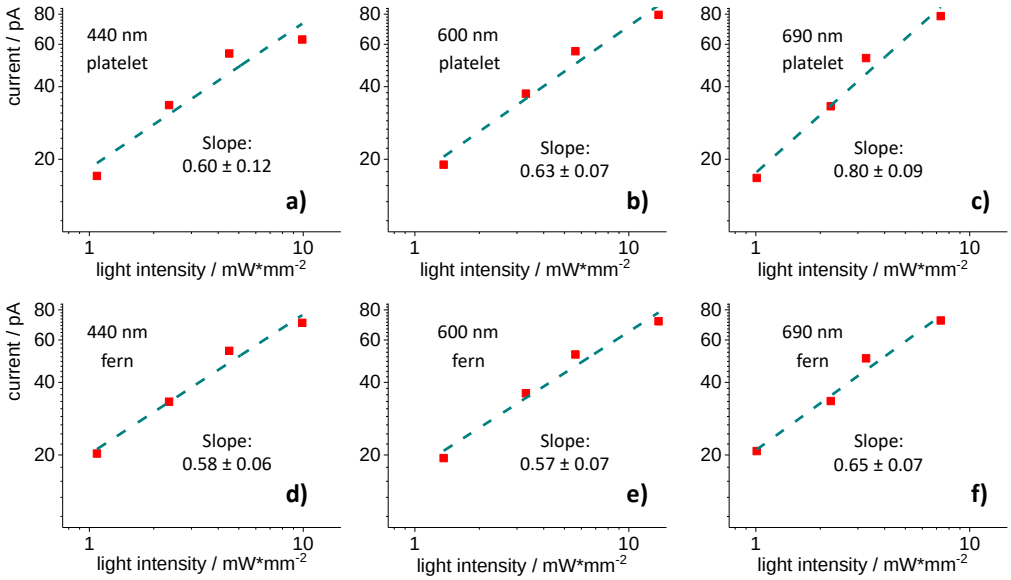

Figure 5.11: Dependence of the ON-current peak maxima on various light intensities. Data was collected from the measurements shown in Figure 5.10: a), b), c) platelet and d), e), f) fern regions. A linear fit of data points in all figures is visualized via dashed lines.

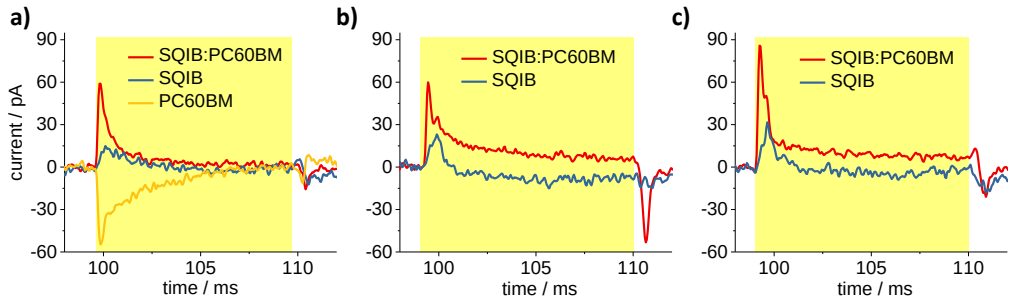

Figure 5.12: Transient photocurrent measurements of three types of devices applying following settings for the illumination source: 150 W xenon high stability lamp, 440 nm (0.17 mm^2 light spot size, 1.75 mW), 600 nm (0.06 mm^2 light spot size, 0.9 mW) and 690 nm (0.05 mm^2 light spot size, 0.39 mW). Recordings of ON- and OFF-current peak signals induced upon photostimulation of SQIB:PC60BM(1:1)/ITO/glass, SQIB(6 mg/mL)/ITO/glass and PC60BM(6 mg/mL)/ITO/glass samples at a) 440 nm, b) 600 nm and c) 690 nm with 10 ms light pulses. All samples were annealed at 180 °C for 2h.

5.5 Photostimulation Recordings of N2A Cells Grown on SQIB:PC60BM Photoreceptor in Voltage- and Current-Clamp Mode

The sufficient cell adhesion and successfully established capacitive coupling at the semiconductor-electrolyte interface were promising preconditions to test the feasibility of photostimulating N2A cells grown on the SQIB:PC60BM photoreceptor. For this purpose, the single N2A cells were clamped to a holding potential of -70 mV in whole-cell configuration while the sensor was stimulated with 10 ms light pulses (Figure 5.13). The photostimulation caused fast transmembrane currents at the onset of illumination and upon the termination of the light pulse (Figure 5.13 b)). The similarity to the photoinduced ON- and OFF- transients in the electrolyte was noticeable and motivated a control experiment where the N2A cells were probed on devices containing only the photoactive layer supported on glass substrates. The current signal was inhibited upon the removal of the ITO electrode which leads to the conclusion that the transmembrane currents were of a photocapacitive nature (Figure 5.13 c)). Further current-clamp measurements proved that the transmembrane currents were directly linked to a photoinduced depolarization (light on) and hyperpolarization (light off) of the cell membrane (Figure 5.13 a)). In spite of the successful photostimulation of the cell membrane, the extent of the depolarization was not sufficient to activate voltage-gated ion channels. Instead, the cell response was limited to a passive capacitive transmembrane current that did not change upon application of TTX (Figure 5.13 d)).

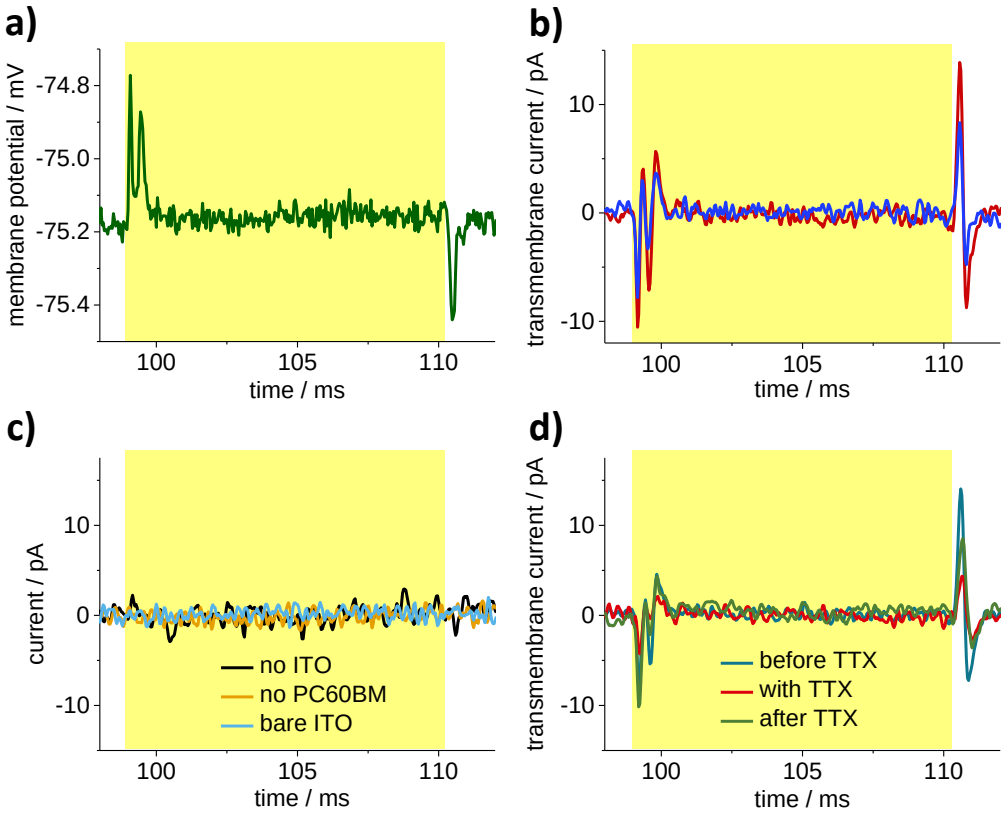

Figure 5.13: Voltage- and current-clamp recordings in standard Ringer's solution of N2A cells grown on SQIB:PC60BM(1:1)/ITO/glass (180 °C, 2h) devices using following settings for the illumination source: 150 W xenon high stability lamp, 690 nm, 0.05 mm^2 light spot size, 0.39 mW, 10 ms light pulse. a) Current-clamp recording that depicts the depolarization and hyperpolarization signals induced by a 10 ms light pulse. The voltage trace represents the average value of 10 consecutive recordings on one N2A cell. b) Voltage-clamp measurements of passive transmembrane currents induced upon on- and offset of illumination in N2A cells grown on platelet (red current trace) and fern structures (blue current trace). c) Voltage-clamp experiments of N2A cells grown on bare ITO/glass, on SQIB:PC60BM(1:1)/glass and on SQIB(6 mg/mL)/ITO/glass devices, all annealed at 180 °C for 2h. d) Voltage-clamp experiments of N2A cells grown on SQIB:PC60BM(1:1)/ITO/glass samples in standard Ringer's solution containing TTX. All voltage-clamp recordings were conducted at a holding potential of -70 mV. Current responses were normalized to 10 pF capacitance. The sampling rate for all measurements was set to 25 kHz.

5.6 Stability Tests

Regarding applicability in a biological environment, a non-degradable photoreceptor is vital. To test this, it was necessary to conduct stability experiments which consisted of exposing the SQIB:PC60BM device to ambient and aqueous conditions in the dark and under constant illumination. The atomic force microscopy technique was employed to monitor any morphological changes. According to the before and after AFM images depicted in Figure 5.14 degradation processes affected both platelet and fern structures. Their respective initial states are shown in images 5.14 a) and 5.14 d) recorded under ambient conditions in the dark. The platelets show first signs of degradation three days after storage in Ringer's solution. In addition to cracks that are noticeable along the thin rifts that are a characteristic feature for the platelets there was also an increase in the root-mean-square roughness of the platelets from 1.7 to 2.1 nm (Figure 5.14 b)).[184] The degradation was facilitated by constant illumination. Three days of additional constant white light illumination resulted in a further increase of the roughness to 6.3 nm and a complete loss of the platelet structures (Figure 5.14 c)). A similar loss of material is observed for the fern regions (Figure 5.14 e)). While the voids between the ferns show no structural changes, the ferns thin out upon exposure to Ringer's solution combined with constant illumination. Moreover, there is a decrease in the root-mean-square roughness of the ferns from 63 to 28 nm due to the skeletonizing of the thick fern branches.[184]

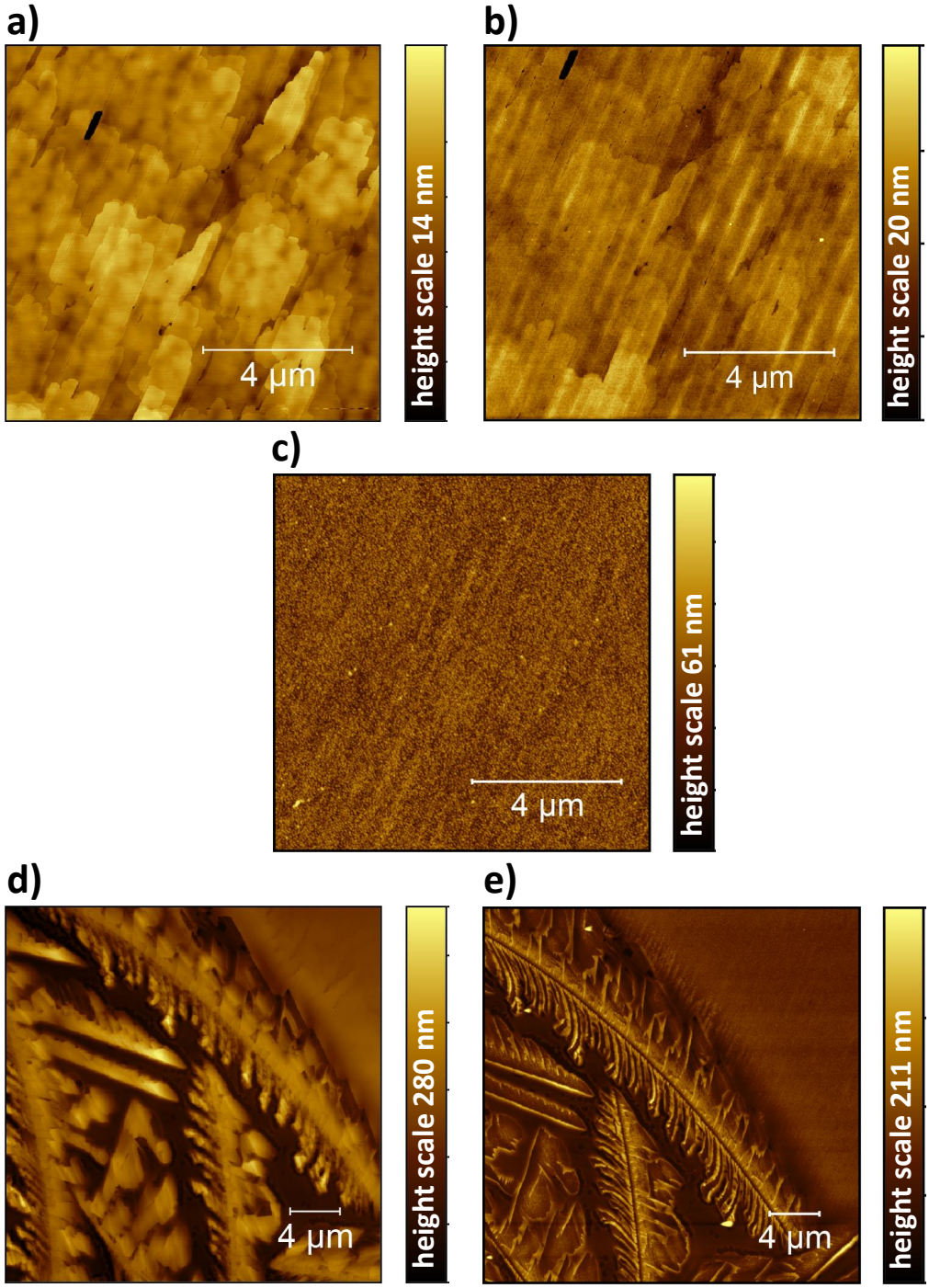

Figure 5.14: Stability tests of SQIB:PC60BM(1:1)/ITO/glass (180 °C, 2h) devices under ambient conditions and in Ringer's solution measured via atomic force microscopy. Images of a) platelet and d) fern structures were recorded under ambient conditions. The same regions are also depicted in Figures b) platelet: after 3 days in Ringer's solution under dark conditions, c) platelet: after an additional 3 days under constant illumination, e) fern: stored in Ringer's solution for 6 days, first 3 days in the dark followed by 3 days under constant illumination. (Samples were prepared by Oliya S. Abdullaeva. AFM measurements were conducted by Frank Balzer).

Chapter 6

Optimization

This chapter presents the optimization procedure that was undertaken on the basis of the results discussed in the preceding Chapter 5. Several parameters regarding the device architecture and experimental setup were systematically modified with the goal to enhance the photocurrent response and subsequently the depolarization of the cell membrane. Following summary lists each parameter and outlines how their modification effects the device performance:[1]

⇒ **Subchapter 6.1**
Mixture ratio and annealing temperature of the SQIB:PC60BM blend film.
Result:
The photocurrent response depends on the blend film morphology. Increasing the amount of SQIB in the blend film and slightly decreasing the annealing temperature results in more platelet motifs in the photoactive layer and subsequently larger transient photocurrents.

⇒ **Subchapter 6.2**
Introduction of a dielectric coating with varying thicknesses on top of the photoactive layer for improved device stability and as a barrier against Faradaic current flow into the electrolyte.
Result:
This subchapter illustrates the importance of photoinduced capacitive charge injection for the SQIB:PC60BM-electrolyte interface which is investigated by adding a dielectric coating into the device architecture.

[1] Parts of this chapter have been published in: " *Organic Photovoltaic Sensors for Photocapacitive Stimulation of Voltage-Gated Ion Channels in Neuroblastoma Cells*".[196]

The coating contributes to an increase in capacitive charge injection and to a longer decay time of the transient photocurrent signal.

⇒ **Subchapter 6.3**
Composition of the Ringer's solution and sheet resistance of the ITO electrode.
Result:
The magnitude of the depolarization recorded in N2A cells depends on the amount of capacitive charge injection as well as the electrolyte resistance and can be enhanced by decreasing the concentrations of NaCl and KCl in the Ringer's solution. Interestingly, it was also found that the sheet resistance of the ITO electrode plays a crucial role in increasing the photocurrent response and the charge injection.

⇒ **Subchapter 6.4**
A systematic study investigating the effect of the spot size and light power of the light beam on the device performance. Here, a white LED was employed as a light source where the alignment allowed two defined spot sizes for the light beam.
Result:
The transient current response, the charge injection and depolarization depend on the size of the illuminated area and on the light power, rather than the light intensity.

6.1 SQIB:PC60BM Blend Film Morphology

6.1.1 Effect of the Mixture Ratio

The results that were shown in Chapter 5 proof not only the feasibility of capacitive coupling at the interface between squaraine-based photosensor and electrolyte but also that the magnitude of the capacitive coupling depends on the morphology of the SQIB:PC60BM film. The platelet motifs contribute to larger ionic displacement currents. Therefore, the initial steps towards more optimized devices consisted of testing different mixture ratios of SQIB and PC60BM and determining how the device fabrication influences the resulting morphology. The photoelectrical responses of the new devices were probed via the patch-clamp technique under the same floating conditions described previously. It needs to be noted here that a new light source was chosen for the optimization phase which consisted of a 625 nm LED that illuminated the samples from below (Figures 6.1 a) and b)). Compared to the xenon lamp this allowed photostimulation experiments with a defined light spot size that can be adjusted by an iris diaphragm. Furthermore, the light path of the LED was directed by a mirror through the microscope condenser directly onto the ITO/glass substrate of the photoreceptor device without the risk of losses in the light intensity due to light scattering, as was the case for a photostimulation across the electrolyte by the Leica objective. Images illustrating the LED setup can be found in the experimental section (see Figures 10.2 and 10.3). Information about the light spot size and light power for each measurement is given in the captions.

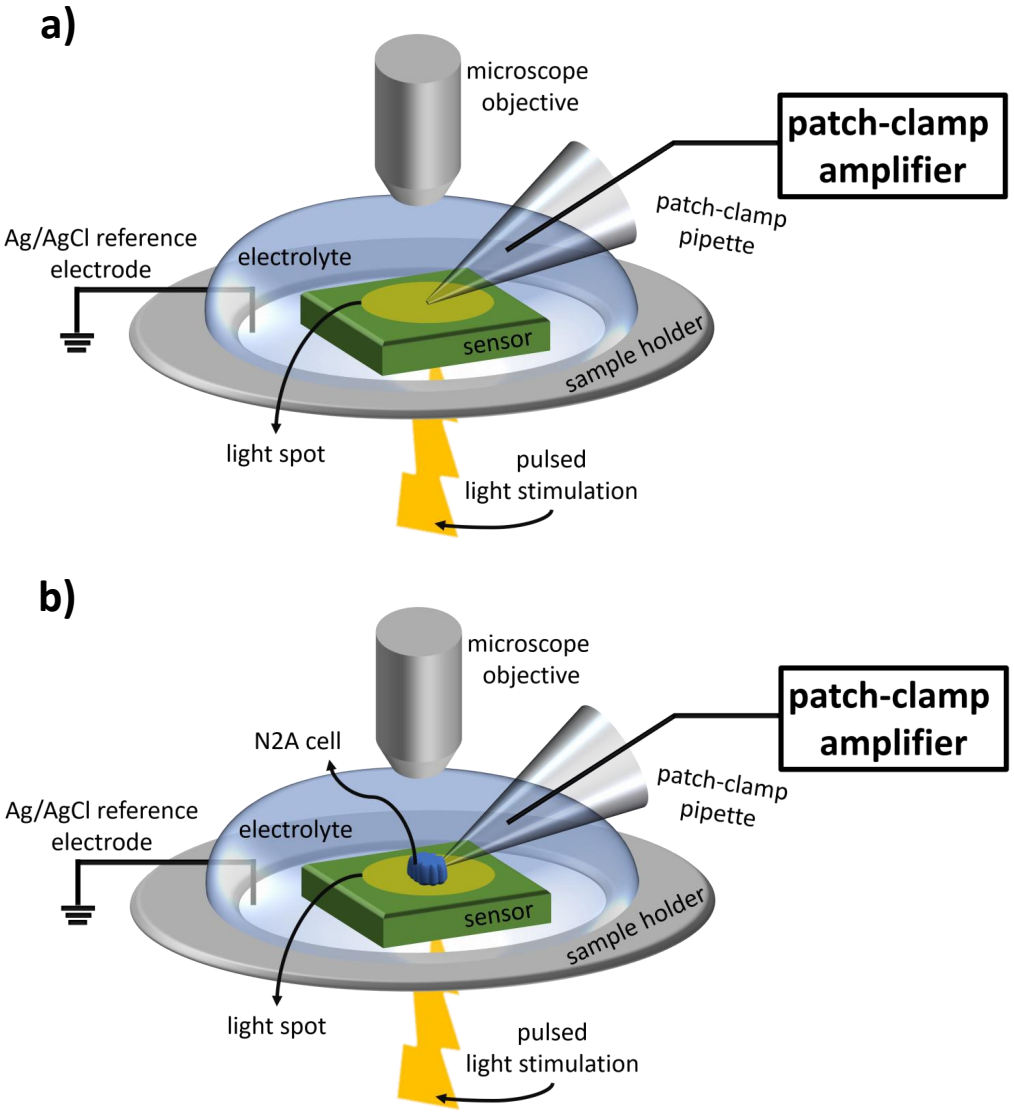

Figure 6.1: Schematic illustration of the experimental setup that was used for all a) transient photocurrent and b) patch-clamp recordings. The middle of a Teflon ring sample holder was closed with a glass plate. The photosensor was placed onto the glass and covered with the electrolyte. The devices shown in this and the following chapters were photostimulated from the bottom. A Leica microscope objective (20x or 40x) was immersed into the electrolyte to patch-clamp the N2A cells, to monitor the device surface and the tip of the patch-clamp electrode. The same water-immersion objectives were used to record images of the N2A cells. Images of various light spots were taken with a 5x Leica objective. During all measurements, an Ag/AgCl reference electrode was placed into the electrolyte without touching the sensor. a) During transient photocurrent recordings, the tip of the patch-clamp electrode was fixed into the center of the light spot and 3 µm above the device surface. b) Patch-clamp recordings entailed attaching the patch-clamp electrode to a single N2A cell that was located in the middle of the light spot.

First, the amount of SQIB was varied. Blend solutions with ratios of 3:1 and 1:3 and a total concentration of 4 mg/mL were spin casted and annealed at 180 °C. Increasing the amount of SQIB did not greatly affect the film morphology, which showed similar fern and platelet structures as the 1:1 mixture (Figure 6.2 a), areas 1 (platelets) and 2 (ferns)). On the contrary, increasing the concentration of PC60BM induced the formation of large branched PC60BM domains for 1:3 devices (Figure 6.2 b) area 2). This was further evidenced by photocurrent measurements of ionic displacement currents with inversed polarity (Figure 6.2 d) yellow current trace) as was reported for PC60BM-alone thin films in the previous Chapter 5 (Figure 5.12 a) yellow current signal). The positive current, most likely stemming from SQIB domains, was marginal and did not exceed 40 pA (Figure 6.2 d) red current signal). The 3:1 device responded with positive photocurrents around 250 pA for both platelet and fern regions (Figure 6.2 c)). As the formation of platelet structures was inhibited for 1:3 samples it becomes apparent that the SQIB amount needs to be equal to or higher than the PC60BM concentration.

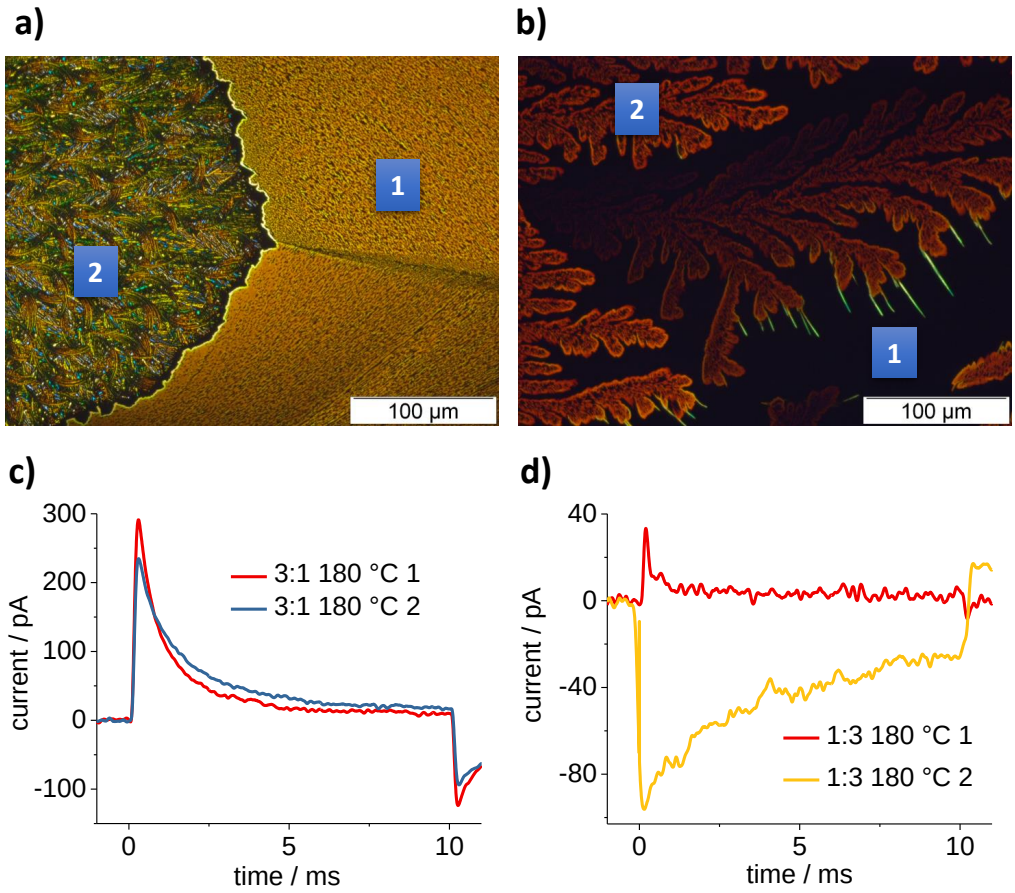

Figure 6.2: Transient photocurrent measurements conducted on a) SQIB:PC60BM(3:1)/ITO/glass and b) SQIB:PC60BM(1:3)/ITO/glass devices in standard Ringer's solution. Both device types were annealed at 180 °C for 2h. Following LED settings were used: 625 nm, 0.15 mm^2 light spot size, 1.6 mW. Recorded current traces in c) and d) represent the average value of 10 consecutive recordings of one sample area. a) A photoactive layer with a mixture ratio of 3:1 features birefringent platelet (1) and fern (2) structures. Platelet motifs feature pinholes similar to the SQIB:PC60BM film with a mixture ratio of 1:1. b) A 1:3 mixture ratio results in large PC60BM motifs (2) that are surrounded by a non-birefringent layer (1). The photocurrents (yellow current trace d)) above area (2) in b) were measured using the 150 W xenon high stability lamp at 400 nm (0.25 mm^2 spot size, 1.4 mW). Optical microscopy images were recorded with Olympus BX41 in reflection with crossed polarizers.

6.1.2 Effect of the Annealing Temperature

In addition to the mixture ratio, the impact of the annealing temperature on the thin film morphology was tested for three different temperatures: 180 °C, 120 °C and 60 °C. In general, upon treatment at 180 °C and 120 °C 3:1 blend films crystallized strongly into fern and platelet structures (Figure 6.3 a), b): 180 °C and c), d): 120 °C). However, the device annealed at 60 °C had a mostly non-birefringent, amorphous morphology with thin

faint fern-like motifs (Figure 6.3 e)). Most significantly, platelet regions that formed during the annealing at 120 °C showed a homogenous closed structure which lacked the characteristic elongated pinholes (Figures 6.3 c), d)). Furthermore, these optimized platelet areas contributed to the highest current peak and charge injection among all samples in Figure 6.3, amounting to 1.26 nA and 0.83 pC, respectively (Figure 6.4). The charge accumulation was calculated by integrating the area under the curve of the transient displacement currents that were measured within the electrolyte for the complete illumination time from 0 to 10 ms. The lowest values were measured for devices annealed at 60 °C. This series of measurements revealed the impact of the annealing temperature on the device performance. Low temperatures do not provide enough thermal energy for a sufficient crystallization while a temperature of 180 °C induces the degradation of the platelet regions due to the formation of pinholes (Figure 6.3 b). 120 °C represents a good tradeoff between these two extremes. It can be concluded that a certain degree of crystallization of the photoactive layer is required to gain large enough displacement currents. This degree of crystallinity is not given for blend films showing an amorphous surface morphology that is silent under crossed polarizers. Importantly, to develop artificial photoreceptors, crystalline structures are known to be more persistent and stable.[185] Since they also exhibit platelet and fern motifs, it is most likely that 3:1 devices also undergo a phase separation upon annealing at 120 °C, similar to the 1:1 samples, annealed at 180 °C, described before (see 5.1 Characterization of SQIB:PC60BM Photoreceptor). By reducing the annealing temperature by 60 °C the formation of pinholes can be avoided. Nevertheless, further morphological investigations are required to validate this hypothesis, in particular, transmission electron microscopy images to test if tesselated structures found in the pinholes of the 1:1 thin film (see 5.1 Characterization of SQIB:PC60BM Photoreceptor) are also present underneath the platelet regions of the 3:1 device. As was previously discussed, regarding capacitive coupling, photoinduced space charges within the photoactive layer play a key role. It is most likely that the thermally induced phase separation results in large PC60BM and SQIB domains forming a bilayer-type structure with a pure SQIB layer on top and an amorphous PC60BM sandwiched between the top layer and the ITO electrode. On the other hand, non-crystalline blend films as shown in Figure 6.3 e) seem to favor Faradaic charge transfer.

The resulting charge is in the same order of magnitude as the platelet regions of the 3:1 device annealed at 180 °C, although the current peak amplitude does not exceed 100 pA (Figure 6.4).

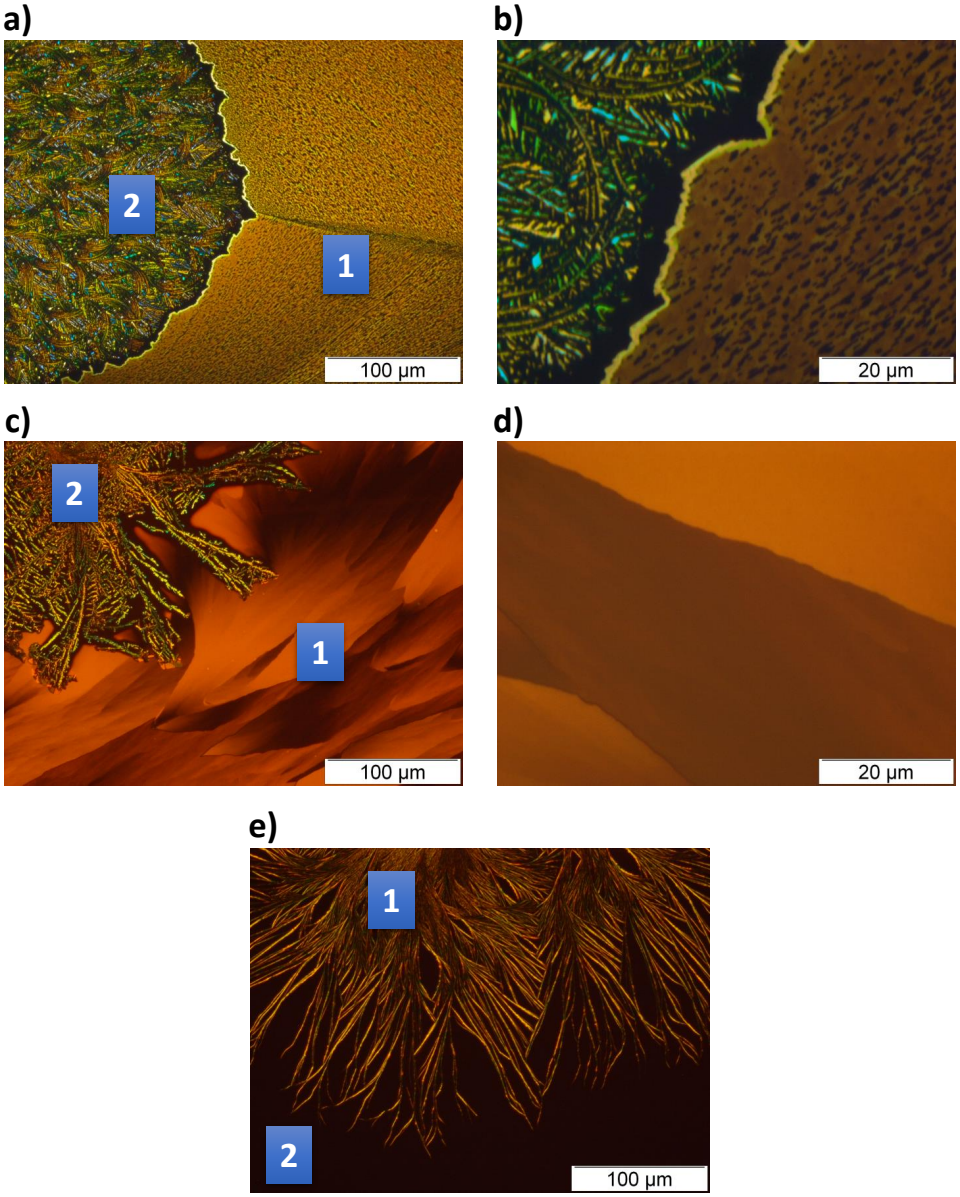

Figure 6.3: Variation of the annealing temperature for the SQIB:PC60BM(3:1)/ITO/glass device. Optical microscopy images recorded with Olympus BX41 in reflection with crossed polarizers. a) A sample that was annealed at 180 °C for 2h shows platelet (1) and fern (2) areas. A magnified image of the interface between platelet and fern regions is given in b) that shows noticeable pinholes in the platelets and thin branches on the fern side. c) Samples annealed at 120 °C, 2h also feature platelet (1) and fern (2) structures. In contrast to b), annealing the 3:1 samples at 120 °C gives a closed platelet layer that is shown in d). e) demonstrates the outcome of annealing the 3:1 device at merely 60 °C for 20 min. A formation of thin fern structures (1) is visible which are surrounded by a non-birefringent layer (2).

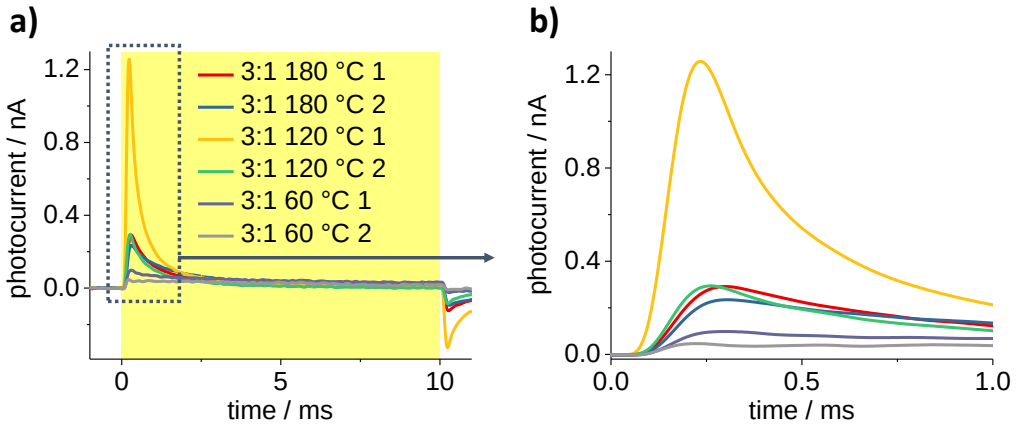

sample	current peak / nA	charge / pC
3:1, 180 °C, platelet 1	0.29	0.42
3:1, 180 °C, fern 2	0.24	0.52
3:1, 120 °C, platelet 1	1.26	0.83
3:1, 120 °C, fern 2	0.29	0.32
3:1, 60 °C, 1	0.10	0.45
3:1, 60 °C, 2	0.05	0.27

Figure 6.4: Transient photocurrent measurements of samples shown in Figure 6.3, conducted on SQIB:PC60BM(3:1)/ITO/glass devices in standard Ringer's solution. Following LED settings were used: 625 nm, 0.15 mm^2 light spot size, 1.6 mW. The table below shows values for ON-current peak maxima and charge injection that were obtained from the recording above. Recorded current traces represent the average value of 10 consecutive recordings of one sample area.

6.1.3 Comparison between 3:1 and 1:1 SQIB:PC60BM

In the third series of photostimulation experiments, a new set of devices with 3:1 and 1:1 mixture ratios were compared. First, the optimized light source consisting of the 625 nm LED enhanced the current response of the 1:1 sample, annealed at 180 °C (Figure 6.5 b) and 6.6). There was an approximately fivefold increase in the photocurrent measured above platelet areas whereas ferns showed lower signals, confirming the discrepancy in the photocurrent response of both motifs observed in the previous chapter. The difference in photocurrent amplitude for fern and platelet structures was more pronounced for the 3:1 sample, 1.5 pA (platelet) versus 0.35 pA (fern) (Figure 6.6). Although the platelet regions for both mixture ratios revealed approximately the same amount of charge injection, the current peak amplitude showed higher values for the 3:1 sample, outperforming the 1:1 device by a factor of 3.

Besides differences in the performances, there were variations in the macroscopic absorbance spectra of both blend ratios (Figure 6.5 c)). The thinner 3:1 blend with a total concentration of 4 mg/mL exhibited a lower absorbance (blue trace). Another variation could be found in the peak ratio of the two humps at 650 and 730 nm. As the absorbance spectra are superpositions of fern and platelet regions, the absorbance signal at 650 nm of the 1:1 sample is usually pronounced for samples that contain more fern structures. This changes upon increasing the concentration of SQIB which results in a weaker absorbance at 650 nm, indicating the formation of platelet-rich areas. Optimizing the mixture in favor of SQIB leads to fern-poor thin films that induce larger displacement currents. This behavior is also noticeable in optical microscopy images of 1:1 and 3:1 samples (Figure 6.5 a) 3:1 and b) 1:1). Fern regions dominate the 1:1 photoactive blend film surface and show thicker more pronounced fern crystals whereas the ferns on the 3:1 device appear thinner and smaller. Increasing the thickness of the 3:1 blend film by drop casting the solution onto the ITO/glass substrates did not improve the current signal (Figure 6.7 b)). An approximately 50 % lower current response was recorded for platelet areas found on the drop casted sample, compared to platelet motifs of the 3:1 film (Figure 6.7 d)). Moreover, a new type of motif formed in the drop casted device upon annealing (Figure 6.7 b) area 1). However, the photocurrents measured for these structures did not exceed 100 pA (Figure 6.7 d)).

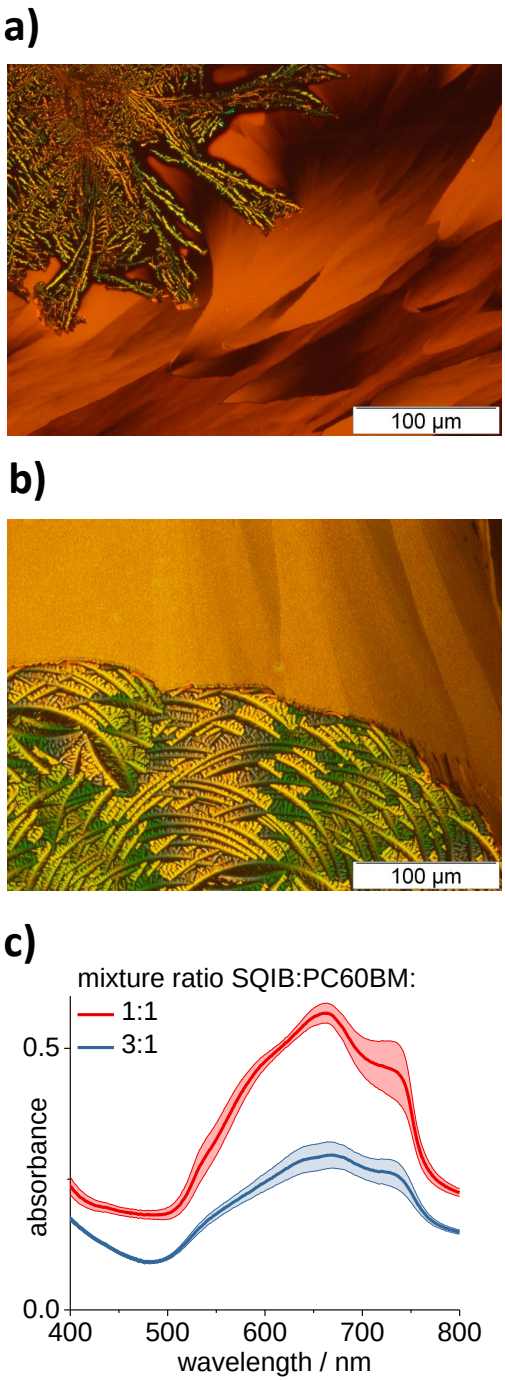

Figure 6.5: Characterization of SQIB:PC60BM/ITO/glass samples that feature different mixture ratios. Polarized optical microscopy images taken in reflection (Olympus BX41, crossed polarizers) of SQIB:PC60BM photoactive layers with a mixture ratio of a) 3:1 (120 °C, 2h) and b) 1:1 (180 °C, 2h). c) Macroscopic absorbance spectra of 3:1 (total concentration 4 mg/mL) (blue trace) and 1:1 (total concentration 12 mg/mL) (red trace) samples. Shaded areas are standard deviations. The traces represent the average value of 7 samples for each mixture ratio (recorded with a Cary 100 spectrophotometer, referenced to air, zero/baseline correction).

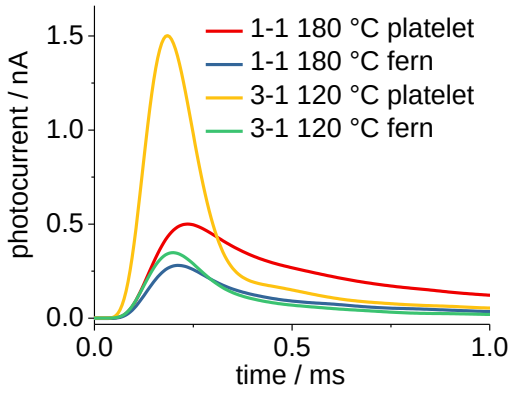

samples uncoated	current peak / nA	charge / pC
1:1, 180 °C, platelet	0.50	0.44
1:1, 180 °C, fern	0.28	0.17
3:1, 120 °C, platelet	1.50	0.42
3:1, 120 °C, fern	0.35	0.12

Figure 6.6: Transient photocurrent measurements conducted on SQIB:PC60BM(1:1)/ITO/glass (180 °C, 2h) and SQIB:PC60BM(3:1)/ITO/glass (120 °C, 2h) devices, in standard Ringer's solution. The aim here was to compare the photocurrent responses between 1:1 and 3:1 devices and their respective platelet and fern regions. Following LED settings were used: 625 nm, 0.15 mm^2 light spot size, 1.6 mW. Table below shows values for ON-current peak maxima and charge injection that were obtained from the recording above.

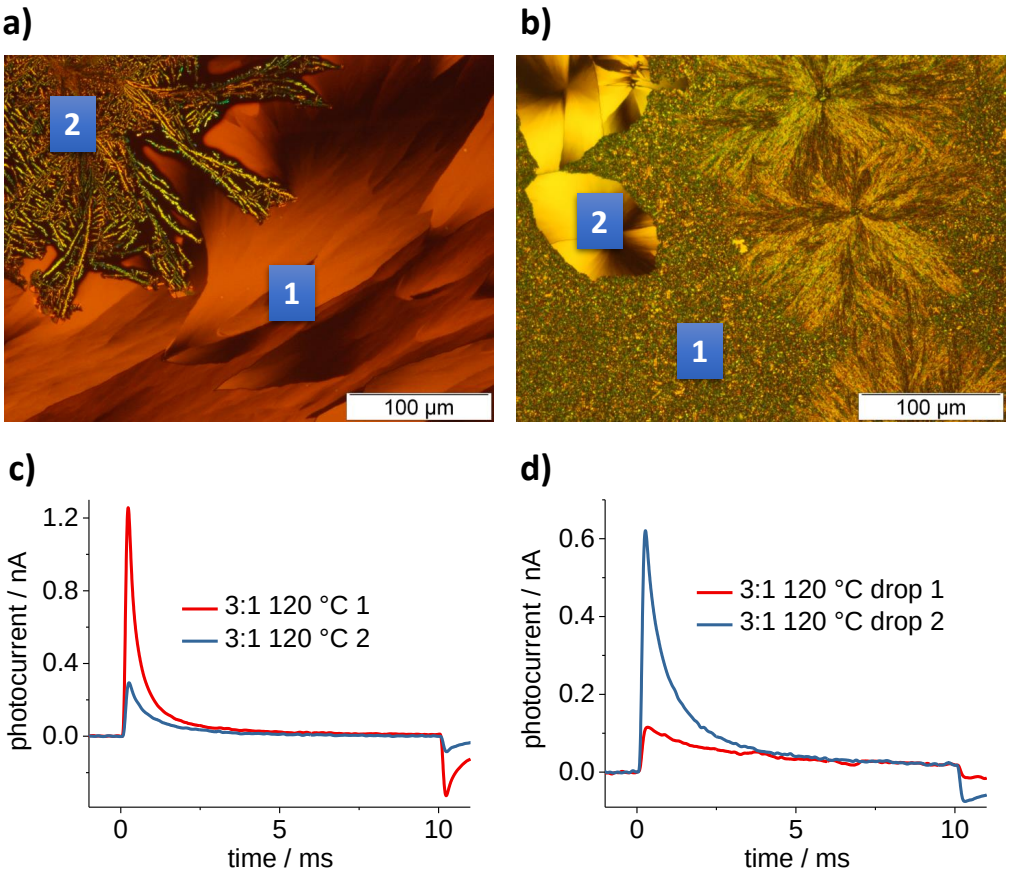

Figure 6.7: Transient photocurrent measurements conducted on SQIB:PC60BM(3:1)/ITO/glass devices, in standard Ringer's solution. The devices were either spin coated (a) and c)) or drop casted (b) and d)) and annealed at 120 °C for 2h. Following LED settings were used: 625 nm, 0.15 mm^2 light spot size, 1.6 mW. Recorded current traces in c) and d) represent the average value of 10 consecutive recordings of one sample area. The spin coated sample shown in a) features platelet (1) and fern (2) regions. Drop casting the SQIB:PC60BM blend solution results in small platelet regions (2) as illustrated in b) surrounded by regions featuring grainy shaped structures (1). Images were taken with an optical microscope (Olympus BX41) in reflection using crossed polarizers.

6.2 Dielectric Coating

Following this, in order to avoid the deterioration of the photoactive layer (see Chapter 5: Stability tests) the SQIB:PC60BM blend film was coated with silicon dioxide as protective layer via electron-beam deposition as shown in Figure 6.8 a). The optical microscopy image in Figure 6.8 b) demonstrates the transparency of the silicon dioxide layer which does not alter the morphology of the SQIB:PC60BM film underneath it.

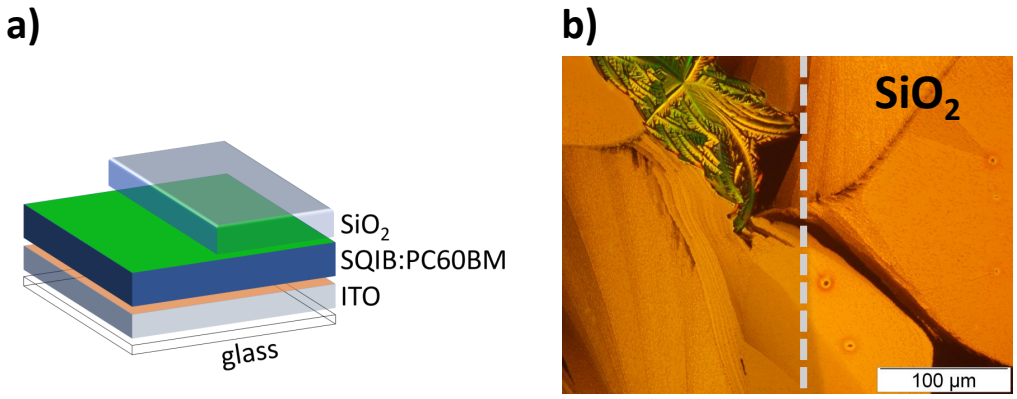

Figure 6.8: a) Schematic illustration of the SQIB:PC60BM/ITO/glass device architecture with a partial silicon dioxide coating.
b) Optical microscopy image (Olympus BX41, reflection, crossed polarizers) of a SQIB:PC60BM(3:1)/ITO/glass (120 °C, 2h) device with (right side) and without (left side) dielectric coating. The image illustrates the morphology of the SQIB:PC60BM blend film surface that features mostly platelet motifs. Moreover, it demonstrates that the photoactive layer is not damaged underneath the coating.

The photoresponses of 3:1 samples with varying coating thicknesses are summarized in Figures 6.9 and 6.10 a). Here, the coating enhanced the charge injection and contributed to a longer decay time of the transient ON-current peak measured for the platelet regions. There was a gradual increase for growing thicknesses up to 55 nm, which featured the maximum charge accumulation, 0.98 pC. On the contrary uncoated areas exhibited the highest current amplitude. The charge injection decreased however for thicker coating layers (96 and 193 nm). For these layer thicknesses the coating assumed a glassy transparent property that gradually ruptured upon insertion into the electrolyte revealing the bare platelet motif underneath (Figure 6.10 b) and c)). Therefore, the 55 nm silicon dioxide layer was selected for all successive devices because it featured the highest amount of charge accumulation.

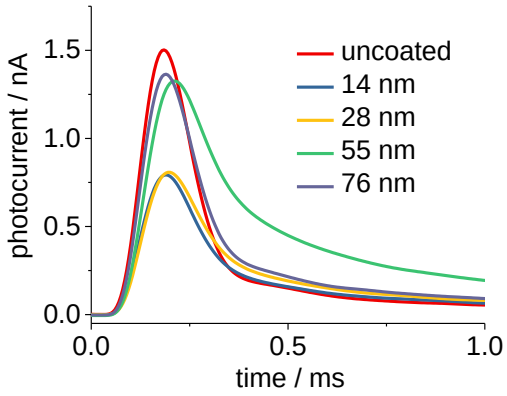

sample SQIB:PC60BM 3:1	current peak / nA	charge / pC
uncoated	1.5	0.42
14 nm	0.79	0.36
28 nm	0.81	0.47
55 nm	1.32	0.98
76 nm	1.36	0.57

Figure 6.9: Transient photocurrent measurements conducted on bare SQIB:PC60BM(3:1)/ITO/glass (120 °C, 2h) devices and devices that were partially covered with either a 14, 28, 55, or 76 nm silicon dioxide coating in standard Ringer's solution. Following LED settings were used: 625 nm, 0.15 mm^2 light spot size, 1.6 mW. The table below shows values for ON-current peak maxima and charge injection that were obtained from the recording above. Recorded current traces represent the average value of 10 consecutive recordings of one sample area.

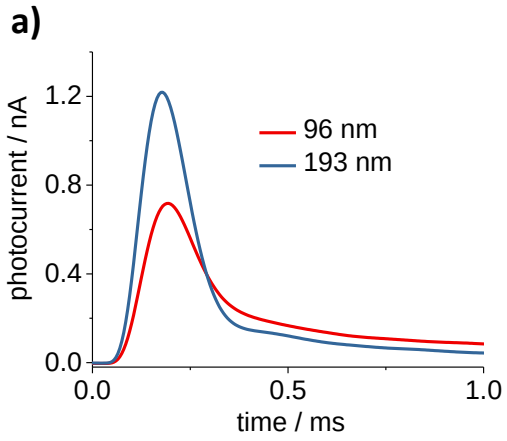

sample SQIB:PC60BM 3:1	current peak / nA	charge / pC
96 nm	0.72	0.50
193 nm	1.22	0.35

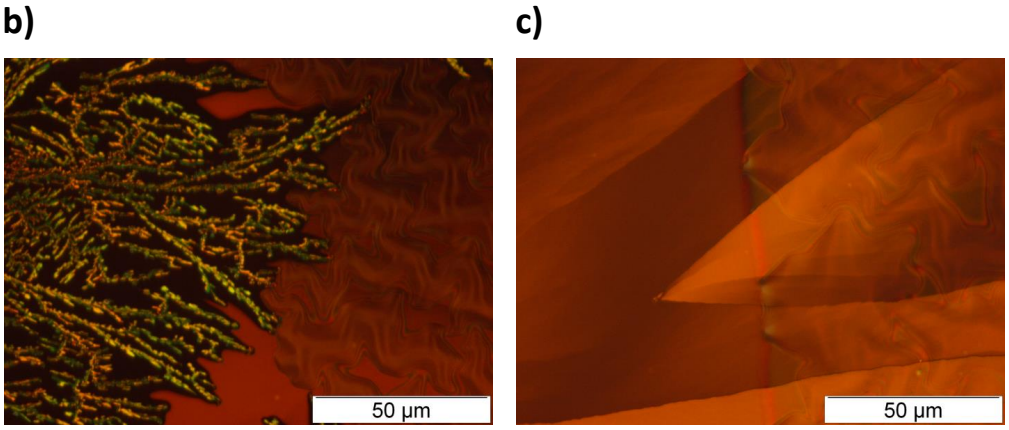

Figure 6.10: a) Transient photocurrent measurements conducted on SQIB:PC60BM(3:1)/ITO/glass (120 °C, 2h) devices that were partially covered with either a 96 nm or 193 nm silicon dioxide coating in standard Ringer's solution. Following LED settings were used: 625 nm, 0.15 mm^2 light spot size, 1.6 mW. The table in the middle shows values for ON-current peak maxima and charge injection that were obtained in recording a). Recorded current curves represent the average value of 10 consecutive recordings of one sample area. b) and c) are optical microscopy images, taken with an Olympus BX41 in reflection using crossed polarizers, of SQIB:PC60BM(3:1)/ITO/glass devices with coated (b): 96 nm, c): 193 nm SiO_2) and uncoated regions. The platelet and fern structures are noticeable in the images as is the border between the bare photoactive layer and silicon dioxide (right side of images are coated). The images demonstrate further that very thick layers of silicon dioxide exhibit a glassy surface.

6.3 Variations in the Electrolyte Resistance and Sheet Resistance of the ITO Electrode

6.3.1 Ringer's Solution

The focus of this measurement series was to investigate the role of the electrolyte concentration on the depolarization of the membrane potential. To this end, three types of Ringer's solution were tested. Apart from the standard Ringer's solution, the second type contained no KCl, and also the NaCl concentration was reduced from 137 mM to 50 mM. To gain a very high concentration, the NaCl concentration for the third type was drastically increased to 300 mM without omission of KCl. The remaining content that consisted of $CaCl_2$, $MgCl_2$, D-glucose, and HEPES for all types was not altered. Figure 6.11 b) demonstrates the photoinduced changes in the membrane potential for all three electrolyte concentrations. The membrane potential showed a fast transient depolarization peak at the beginning of the light pulse and a hyperpolarization at the offset of illumination. The depolarization peak was analyzed closely and normalized to a capacitance of 20 pF, which represents the average capacitance of all measured N2A cells shown in this chapter. Solely coating the blend film with 55 nm silicon dioxide and optimizing the light source to the 625 nm LED without modifying the Ringer's solution resulted in a mere 5 mV depolarization. A 15-fold increase in the depolarization signal compared to the data shown in Chapter 5 was observed however for the Ringer's solution with a NaCl concentration of 50 mM without the presence of KCl, which will be referred to henceforward as "modified Ringer's solution". In comparison, the depolarization dropped drastically to approximate1y 1 mV for the solution containing 300 mM NaCl. This behavior is in good agreement with the observations reported by Fromherz et al. who gained a sufficient capacitive stimulation by depleting the NaCl concentration and thereby increasing the electrolyte resistance.[98] Although it was was not possible to directly obtain a value for the resistance of the Ringer's solution used in this thesis, the resistance of the patch-clamp electrode posed a good measure for the conductance of the electrolyte. The same patch-clamp electrode showed a two-fold decrease in the resistance when placed from a standard into an electrolyte containing 300 mM NaCl.

Moreover, similar to the behavior of the displacement currents, increasing the amount of SQIB in the mixture ratio enhanced the strength of the depolarization up to 40 mV (Figure 6.11 d)).

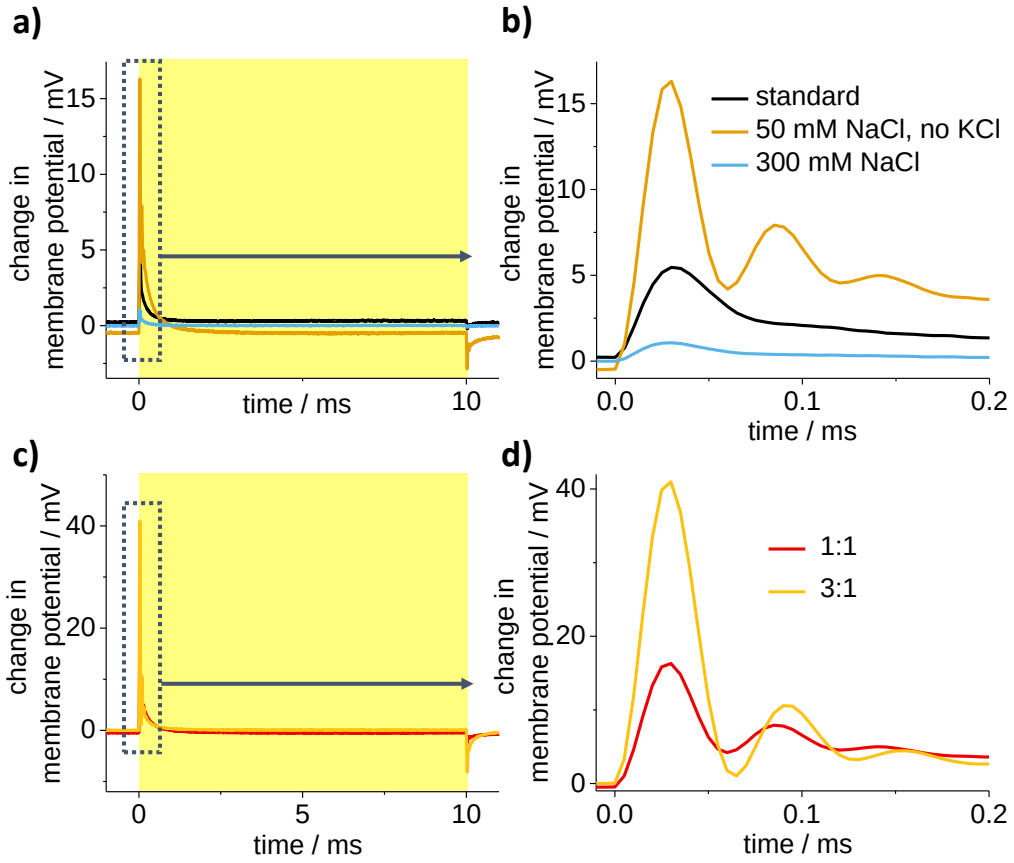

Figure 6.11: Current-clamp recordings of N2A cells grown on SiO_2(55nm)/SQIB:PC60BM/ITO/glass devices using following LED settings: 625 nm, 0.84 mm^2 light spot size, 21 mW. Each voltage trace represents the average value of 10 consecutive recordings on one N2A cell. Measurements were normalized to 20 pF capacitance. a) Complete recording that depicts the depolarization and hyperpolarization signals of N2A cells grown on SiO_2(55nm)/SQIB:PC60BM(1:1)/ITO/glass (180 °C, 2h) samples induced by a 10 ms light pulse. b) Close-up of the depolarization responses shown in a) for three different compositions of the Ringer's solution: standard, 50 mM NaCl without KCl and 300 mM NaCl with standard KCl concentration. c) Photoinduced depolarization and hyperpolarization signals. d) Close-up of the depolarization signals in c) for two mixture ratios of SQIB:PC60BM: 1:1 (180 °C, 2h) and 3:1 (120 °C, 2h), measured in the modified Ringer's solution (50 mM NaCl, no KCl).

6.3.2 ITO Electrode

The effect of the ITO electrode sheet resistance on the photocurrent and charge injection was investigated here. A new type of ITO electrode (termed as "temicon-ITO" here) with a lower sheet resistance of 8 ± 2 Ω/sq compared to the ITO used so far (15 ± 2 Ω/sq, termed henceforward as "old-ITO") was applied.[196] Samples fabricated on the temicon-ITO exhibited a twice higher charge injection in the range of 5 pC with a maximum current amplitude of 10 pA compared to the SQIB:PC60BM blend film fabricated on the old-ITO (Figure 6.13). The difference in the amount of the injected charge for coated and uncoated part of the sample was also pronounced for the temicon-ITO, which doubled from 2.56 to 5.06 pC for coated areas. Nevertheless, additional investigations of the ITO-organic semiconductor interface are required in future studies to explain the impact of the ITO sheet resistance on the device performance.

Despite this major increase in the current signal, the N2A cells could not be depolarized beyond 60 mV (Figure 6.14). There was also no significant difference in the depolarization between N2A cells grown on coated or uncoated areas.

Here, it should be noted that an almost platelet-only device was achieved by further increasing the concentration of SQIB in the blend solution (Figure 6.12). Both the value of the current signal and the charge injection were maximized successfully by selecting a 7:1 mixture ratio (Figure 6.13 7:1 old-ITO +/- SiO_2). Values up to 7 nA and 2.40 pC were obtained for 7:1 samples coated with 55 nm silicon dioxide. Although uncoated regions showed a higher photocurrent response, the charge injection was lower than 2 pC, resulting in a faster decay time for the transient ON-current peak (Figure 6.13 blue current signal). Both coated and uncoated 7:1 blend films showed a salient absorbance signal at 730 nm (Figure 6.12 b)). Maximizing the SQIB concentration in the blend leads almost exclusively to the formation of platelets with a J-aggregation as is also evidenced by optical microscopy images revealing a blend film surface covered almost only by platelet structures (Figure 6.12 a)).

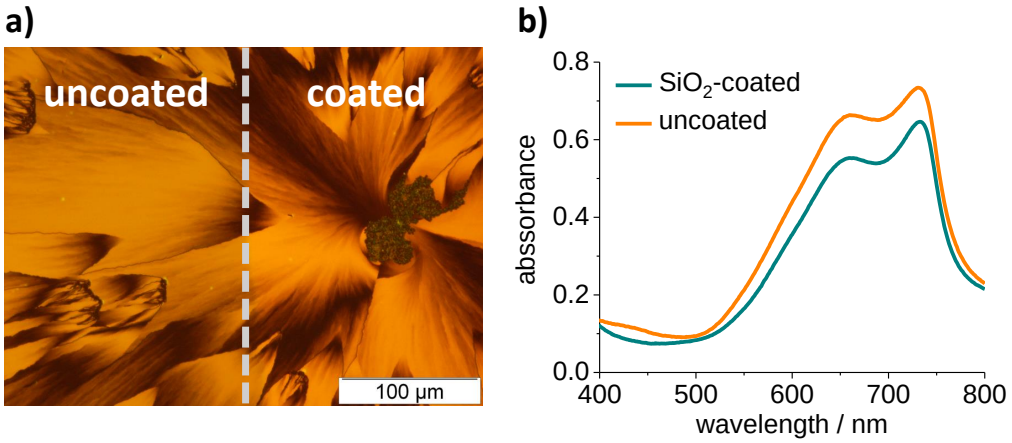

Figure 6.12: Characterization of a SQIB:PC60BM(7:1)/ITO(temicon)/glass device (120 °C, 2h), partially coated with 55 nm silicon dioxide. a) Polarized optical microscopy image (Olympus BX41, reflection, crossed polarizers) showing mostly platelet features after 2h of annealing at 120 °C. b) Absorbance spectra of coated and uncoated regions (recorded with a Cary 100 spectrophotometer, referenced to air, zero/baseline correction).

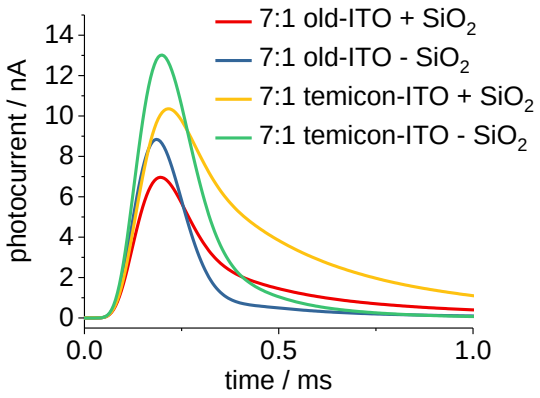

sample	current peak / nA	charge / pC
7:1 old-ITO + 55 nm SiO_2	7	2.40
7:1 old-ITO - 55 nm SiO_2	9	1.73
7:1 temicon-ITO + 55 nm SiO_2	10	5.06
7:1 temicon-ITO - 55 nm SiO_2	13	2.56

Figure 6.13: Transient photocurrent measurements conducted on SQIB:PC60BM(7:1)/ITO(old)/glass and SQIB:PC60BM(7:1)/ITO(temicon)/glass (120 °C, 2h) devices that are partially covered with a 55 nm silicon dioxide coating in modified Ringer's solution. Following LED settings were applied: 625 nm, light spot size: 0.59 mm^2, 12.5 mW (see Figure 10.4, Experimental Section). Table below summarizes values obtained by the data above for current peak maxima and charge injection. Three different regions on the device were measured for each parameter.

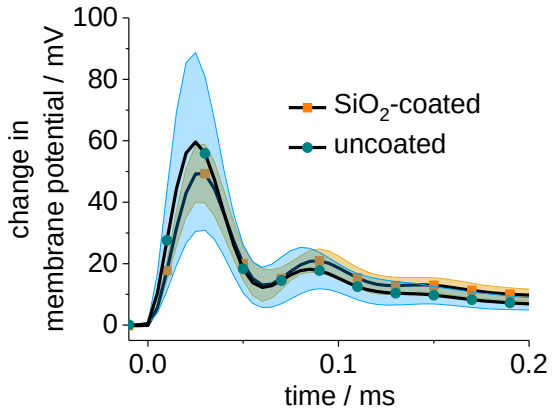

Figure 6.14: Current-clamp recordings of N2A cells grown on coated (55 nm SiO_2) and uncoated regions of a SQIB:PC60BM(7:1)/ITO(temicon)/glass (120 °C, 2h) device in modified Ringer's solution using following LED settings: 625 nm, light spot size: 0.59 mm^2, 12.5 mW. Number of measured N2A cells for coated and non-coated areas: N = 5 cells. Shaded areas represent standard deviations. Measurements were normalized to 20 pF capacitance.

6.4 The Effect of the LED Spot Size and LED Light Power

This final part of the optimization procedure focused on determining how the depolarization and charge injection depend on parameters regarding the illumination source e.g., light power, light intensity and size of the illuminated area on the blend film (see Experimental Section for more information).

To this end, a warm white LED was selected for the photostimulation experiments (details on the LED are given in the experimental section). Adjusting the iris diaphragm enabled two light spot sizes (Figure 6.15 a) spot size I: 2.5 mm^2 and b) spot size II: 0.6 mm^2). In addition, the broad spectrum of this type of LED was beneficial to address the broad absorbance spectrum of the blend film that ranges from 530 nm to 800 nm (see Figure 10.7, Experimental Section).

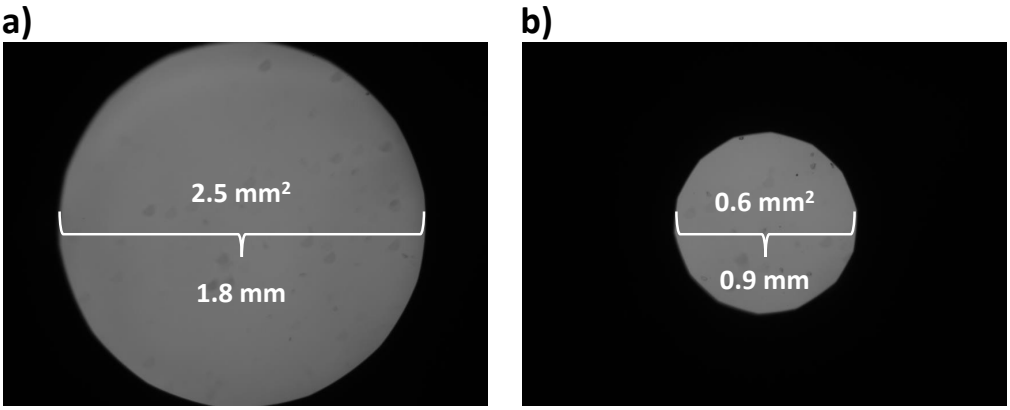

Figure 6.15: Alignment of white LED light source. Light beam adjusted with an iris diaphragm resulting in two light spots with following sizes: a) I: 2.5 mm^2 and b) II: 0.6 mm^2. Images were recorded with a 2000DC CCD digital camera (QImaging Retiga) and Live Acquisition 2.4 software using a 5x Leica objective. Fiji and ImageJ software were employed to calculate the spot sizes. [197,198]

Initially, the photoinduced changes in the membrane potential were measured in current-clamp mode for N2A cells grown on coated and uncoated regions using the larger light spot I (Figure 6.15 a) and 6.16 a)). Most significantly, the degree of depolarization was higher for N2A cells grown on the SiO_2 coating going as far as 80 mV compared to cells on the uncoated layer that did not exceed 50 mV (Figure 6.16 a)). Further analysis of the transient displacement current measured in the electrolyte revealed that the injected charge for the coating amounted to 8 pC while the value for the uncoated layer was lower, 6 pC (Figure 6.17 a)). In agreement with the data obtained so far, the capacitive charge injection was enhanced by the silicon dioxide layer which in turn caused an increase in the membrane depolarization. This trend was also observed for various light powers below 180 mW, as shown in Figure 6.18 b). In comparison, the current peak data collected for light powers ranging from 20 to 180 W had higher values for the uncoated part of the sample (Figure 6.18 a)). Furthermore, the current peak values exhibited a saturation behavior, evidenced by the nonlinearity in the data fitting. The current signals measured above coated areas saturated for light powers higher than 70 mW while this saturation was even more distinct for bare SQIB:PC60BM layers (slope (coated): 0.17 versus slope (uncoated): 0.03) (Figure 6.18 a)). Saturating current values reveal that the device is out of the dynamic range meaning that illuminating the sample with higher light powers would not result in equally higher current responses. [194,195]

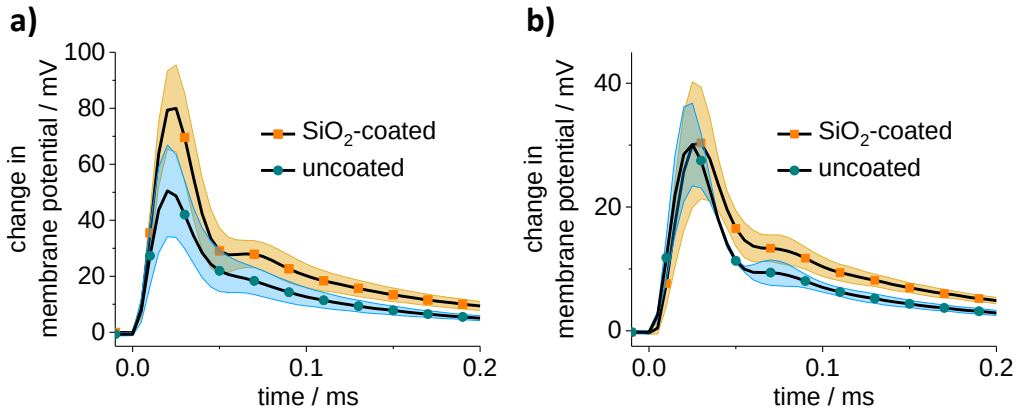

Figure 6.16: Current-clamp recordings of N2A cells grown on coated and uncoated regions of SQIB:PC60BM(7:1)/ITO(temicon)/glass (120 °C, 2h) devices in modified Ringer's solution using following white LED settings: a) I (2.5 mm^2, 180 mW) and b) II (0.6 mm^2, 42 mW). Number of measured N2A cells for coated and non-coated areas: N = 3 cells. Shaded areas represent standard deviations. Measurements were normalized to 20 pF capacitance.

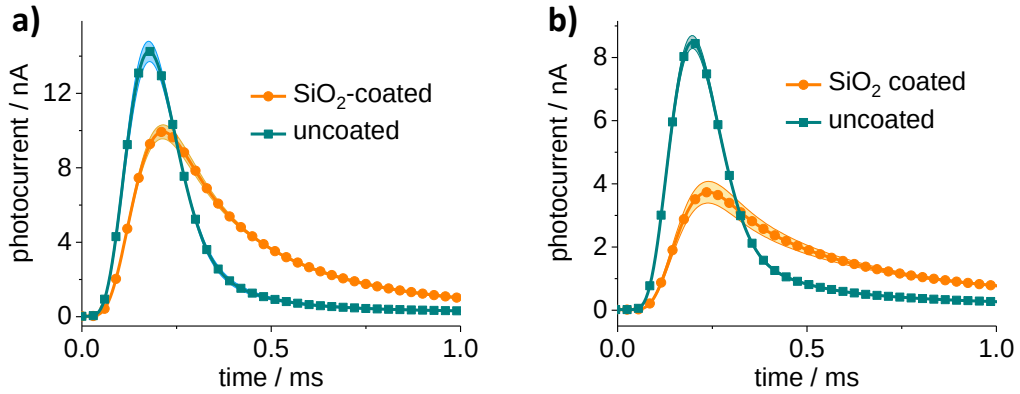

a) Spot size I

sample	current peak / nA	charge / pC
7:1 temicon-ITO + 55 nm SiO_2	9.93	7.98
7:1 temicon-ITO - 55 nm SiO_2	14.25	6.31

b) Spot size II

sample	current peak / nA	charge / pC
7:1 temicon-ITO + 55 nm SiO_2	3.74	4.20
7:1 temicon-ITO - 55 nm SiO_2	8.49	2.84

Figure 6.17: Transient photocurrent measurements conducted on coated and uncoated areas of SQIB:PC60BM(7:1)/ITO(temicon)/glass devices (120 °C, 2h) in modified Ringer's solution: ON-current peaks measured using following light spots: a) I (2.5 mm^2, 180 mW) and b) II (0.6 mm^2, 42 mW). The table below summarizes values obtained from the data above for current peak maxima and charge injection. Three different regions on the device were measured for each parameter. Shaded areas represent standard deviations.

Simultaneously, the same experiments were also conducted applying the smaller light spot II (Figure 6.15 b)). Counterintuitively, there was a strong decline in the magnitude of the depolarization and the transient current signals (Figures 6.16 b) and 6.17 b)). Although both spot sizes display the same light intensity (see Figure 10.6 b) in the Experimental Section), they do show different light powers (see Figure 10.6 a) in the Experimental Section). Hence, it was initially hypothesized that the strength of the photostimulation scales with the light power rather than the light intensity. To verify this, the current peak maxima and charge injection measured with both spot sizes were compared for approximately the same light powers as indicated by the small orange boxes in Figure 10.6 a) (Experimental Section). As Figure 6.19 demonstrates, the device performance scales with the light power because the current peak maxima and charge are in the same order of magnitude for both spot sizes despite different light intensities. However, in addition to the light power, these parameters also seem to scale with the spot size because larger values can be obtained upon increasing the illuminated area (Figure 6.19). The underlying cause for this behavior should be investigated in future experiments. A suitable approach would be to determine the spacial ionic charge distribution in the electrolyte at the illuminated spot since the photocurrent measurements described here were merely conducted at the center of the light spot approximately 3 µm above the photoactive thin film. A study focusing on artificial photoreceptor devices based on organic pigments, exhibiting a photocapacitive working mechanism, found that the photoresponse is indeed enhanced when a larger area of the photoactive layer is illuminated. The highest photoresponse was recorded at the center of the light spot which showed a decay for areas further away from the center. For a large light spot, this decay occurred more slowly compared to the photoresponse measured above areas that were illuminated with a small light spot.[100]

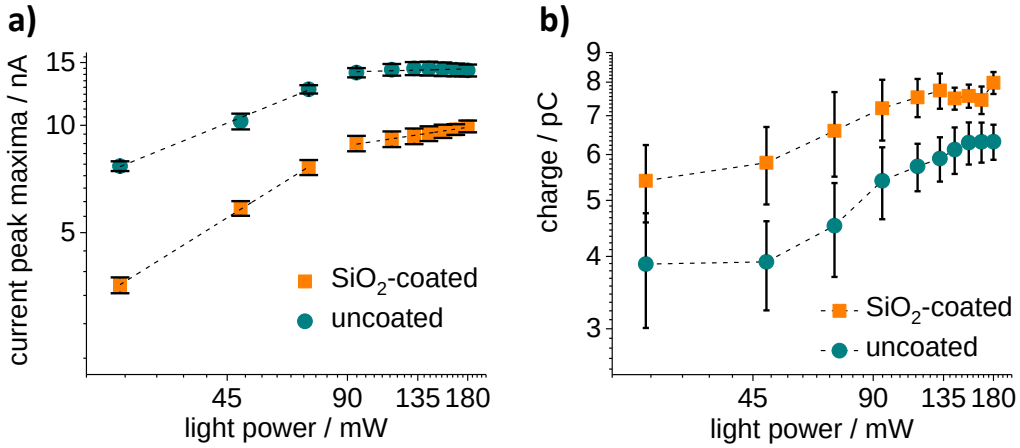

coated	uncoated
0.70 ± 0.01	0.46 ± 0.02
0.17 ± 0.01	0.03 ± 0.01

Figure 6.18: Dependance of the a) current peak maxima and b) charge injection on various LED powers. Data was collected from the measurements shown in Figure 6.17 a) which were conducted with the large light spot I (2.5 mm^2). Error bars represent standard deviations. In total, three sample areas were measured for each parameter. The table below Figure 6.18 a) shows the slopes obtained via linear fit for the first three (coated: 0.70; uncoated: 0.46) and last seven data points (coated: 0.17; uncoated: 0.03) in a) as indicated by dashed lines.

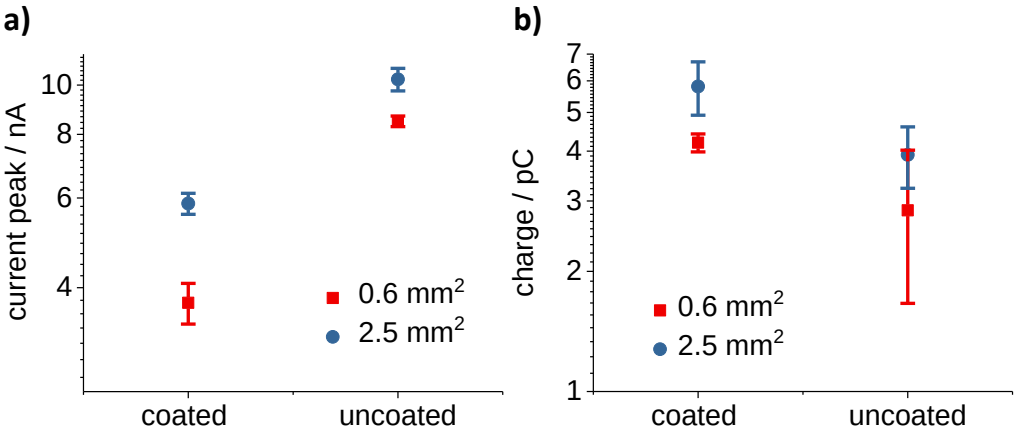

Figure 6.19: a) Current peak maxima and b) charge injection values for coated and uncoated regions of a SQIB:PC60BM(7:1)/ITO(temicon)/glass (120 °C, 2h) device that were measured for light spots I (blue data points, 2.5 mm^2) and II (red data points, 0.6 mm^2) using following light powers: 42 mW (light spot II: 0.6 mm^2) and 48 mW (light spot I: 2.5 mm^2). The data points represent the average current and charge value obtained for three different regions on the device. Error bars represent standard deviations.

6.5 Summary of the Optimization Procedure

The previous chapter demonstrated the feasibility of a capacitive working mechanism for SQIB:PC60BM artificial photoreceptors interfaced with a biological environment. However, the poor device performance limited the amount of depolarization preventing an active cellular response. Now this chapter implemented strategies to maximize the photoresponse initiating depolarization signals that reach the desired threshold necessary to activate voltage-gated ion channels. Figure 6.20 a) shows general trends for the ON-current peak associated with changing various fabrication and experimental conditions. Apart from a gradual rise in the current amplitude, higher charge injection contributes to a prolonged decay time of the transient signal. This behavior is reflected in the changes of the membrane potential (Figure 6.20 b)). Increasing the current peak maxima correlates with a rise in the depolarization. Moreover, longer discharge times are achieved by enhanced charge injection allowing the cells to stay depolarized for a longer period of time.

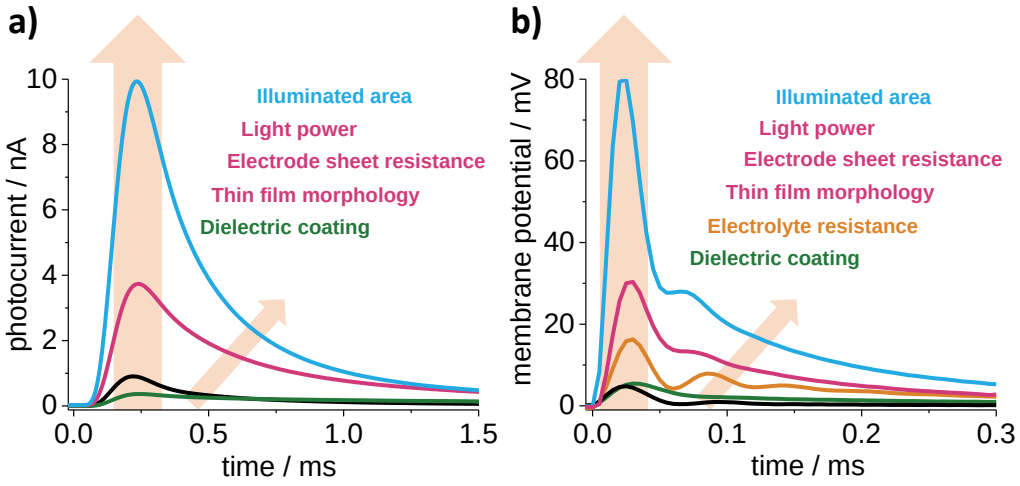

Figure 6.20: Overview of exemplary photocurrent and depolarization signals obtained by systematically optimizing following parameters: dielectric coating, electrolyte resistance, thin film morphology, electrode sheet resistance, light power and the size of the illuminated area.

6.6 Stability Tests

The objective here was to test the long-term stability of the silicon dioxide coating under ambient and aqueous conditions via atomic force and optical microscopy.

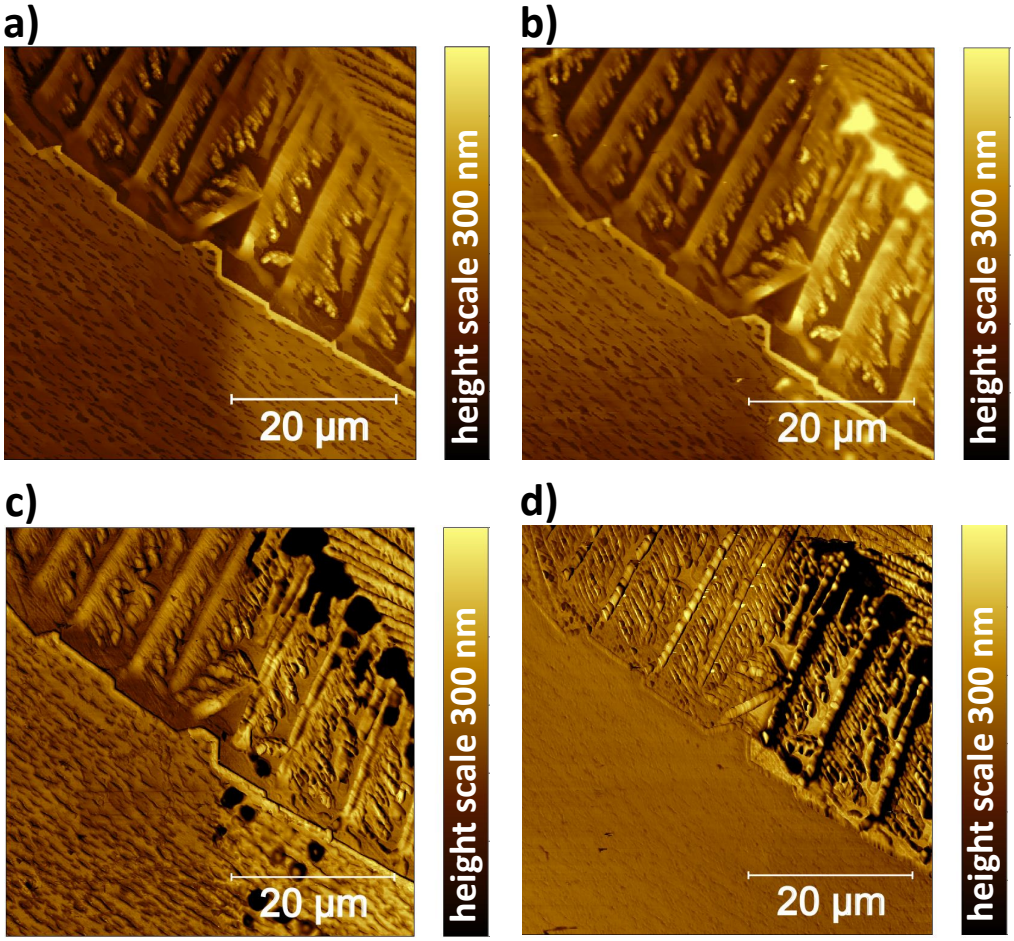

Figure 6.21: Stability tests performed via atomic force microscopy in Ringer's solution of SQIB:PC60BM(1:1)/ITO(old)/glass (180 °C, 2h) devices partially covered with 55 nm silicon dioxide (right side of images). a) Initial condition. b) After 29 hours under dark conditions. c) After 9 days in the dark. d) After 11 days in the dark combined with 27 hours of constant illumination. (Samples were prepared by Oliya S. Abdullaeva and the stability tests conducted by Frank Balzer.)

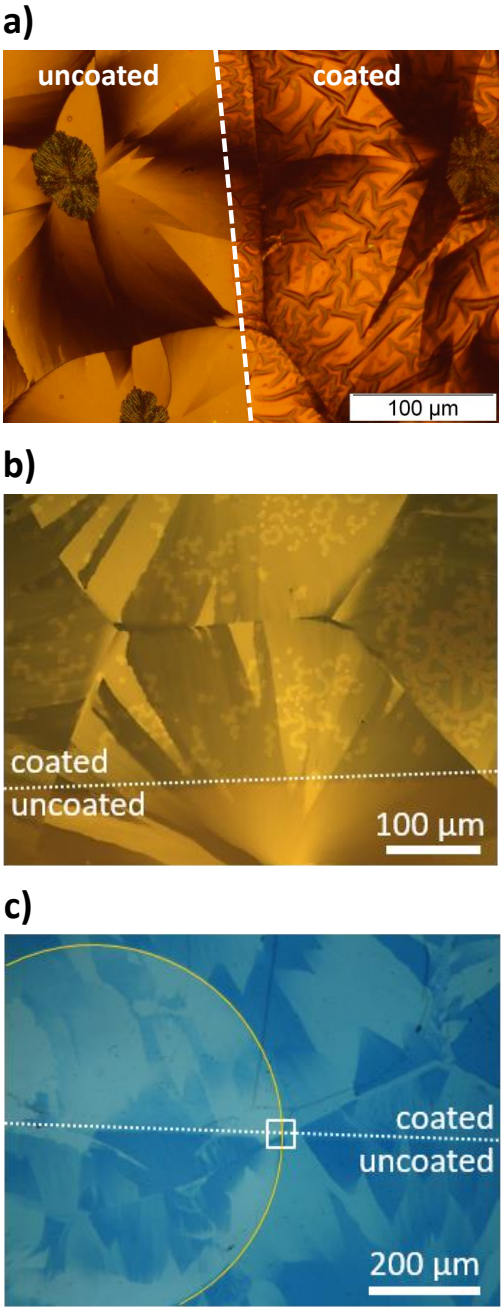

Figure 6.22: Microscopy images of coated (55 nm SiO_2) and uncoated regions of SQIB:PC60BM(7:1)/ITO(temicon)/glass (120 °C, 2h) devices. a) Optical microscopy image (Olympus BX41, in reflection, crossed polarizers) of a sample that was exposed only to pulsed photostimulation during transient photocurrent measurements. b) Microscopy image recorded in reflection with a single polarizer shows a sample 16 min after insertion into the Ringer's solution with constant illumination. c) Transmission microscopy image of a device that was kept in Ringer's solution for 18 h in the dark which was followed by 2h of constant illumination. (Samples were prepared by Oliya S. Abdullaeva and the stability tests conducted by Frank Balzer.)

Although the silicon dioxide coating enhanced the capacitive coupling, it was not able to function as a protective layer for the SQIB:PC60BM layer. AFM stability tests as shown previously were repeated for 1:1 samples partially coated with 55 nm silicon dioxide in Ringer's solution in the dark and under constant illumination (Figure 6.21). Upon placing into the electrolyte, the coated regions suffered from a faster deterioration in comparison to the uncoated side of the layer. As illustrated in Figures 6.21 b) and c) the degradation of the coated areas is characterized by the gradual formation of holes resulting in the ablation of the photoactive layer. The ferns also seemed to skeletonize earlier on the coated areas (Figures 6.21 c) and d)). Constant illumination accelerated the corrosion of the organic material which was more severe for the sample part covered by the silicon dioxide (Figure 6.21 d)). Additional optical microscopy images of the silicon dioxide coating taken after exposure to Ringer's solution provide a macroscopic insight into this degradation process (Figure 6.22). Images a), b), and c) stem from 7:1 devices partially coated with 55 nm SiO_2 that were exposed to Ringer's solution. First, image a) in Figure 6.22 shows a withered sample that was exposed only to pulsed light, one day after photocurrent measurements. Figure 6.22 b), on the other hand, depicts a sample exposed to constant illumination 16 min after insertion into the Ringer's solution. In contrary to the bare SQIB:PC60BM, the coating reacts to the electrolyte with the formation of bubbles and wrinkles. The degree of degradation is also more pronounced for coated regions as can be seen in Figure 6.22 c). Here, the device was kept for 18 h in Ringer's solution under dark conditions and later on illuminated constantly for 2 hours. Silicon dioxide cannot be considered for long-term applications. More stable charge injecting dielectric coatings need to be found in future studies. Nevertheless, the rate of degradation proceeds on a time scale of several hours. The stability is therefore satisfactory during experiments applying pulsed illumination with a duration of a few milliseconds.

Chapter 7

Organic Bioelectronic Interfaces II: Direct Activation of Voltage-Gated Ion Channels

After the successful completion of the optimization, this final chapter focuses on the application of the new optimized 7:1 SQIB:PC60BM device. One of the central objectives that will be discussed here is the impact that the new device morphology including the silicon dioxide coating has on cell growth. Finally, the study will be concluded by determining if the 80 mV depolarization that has been obtained through optimization can trigger an activation of voltage-gated ion channels.[1]

7.1 Cell Growth and Adhesion

The cell growth was evaluated by counting the number of attached cells on three different samples (Figure 7.1 c)). The number of cells was determined for overall 67 coated and 59 uncoated regions. In addition to the total cell number, the number of cells with neurites was also considered (Figure 7.1 b)). The presence of neurites usually signifies that the cells are healthy and tolerate the surface. Similar to the 1:1 sample, the cell growth here was successful without an adhesion promoter. The coated part of the device had the highest number of attached cells, 11 % of which formed neurites (Figure 7.1 a)). This was reduced to 6 % for areas without the coating that also showed a lower number of N2A cells.

[1] Parts of this chapter have been published in: " *Organic Photovoltaic Sensors for Photocapacitive Stimulation of Voltage-Gated Ion Channels in Neuroblastoma Cells*".[196]

A closer analysis of the film morphology via atomic force microscopy might explain this drastic difference in the total number of grown cells (Figure 7.2 a) and b)). Although the RMS surface roughness does not exceed 1 nm for both the coated and uncoated side, the silicon dioxide layer contains small clusters (approximately 41 nm) spread evenly over the surface (Figure 7.2 a)). These clusters possibly provide small intermediate spaces for the cell membrane to attach to. These results agree well with previous studies that found that 10 % of undifferentiated N2A cells exhibit neurites.[199] In conclusion, according to these findings the 7:1 device does not compromise the cell adhesion, and the silicon dioxide coating provides beneficial conditions for cell adhesion.

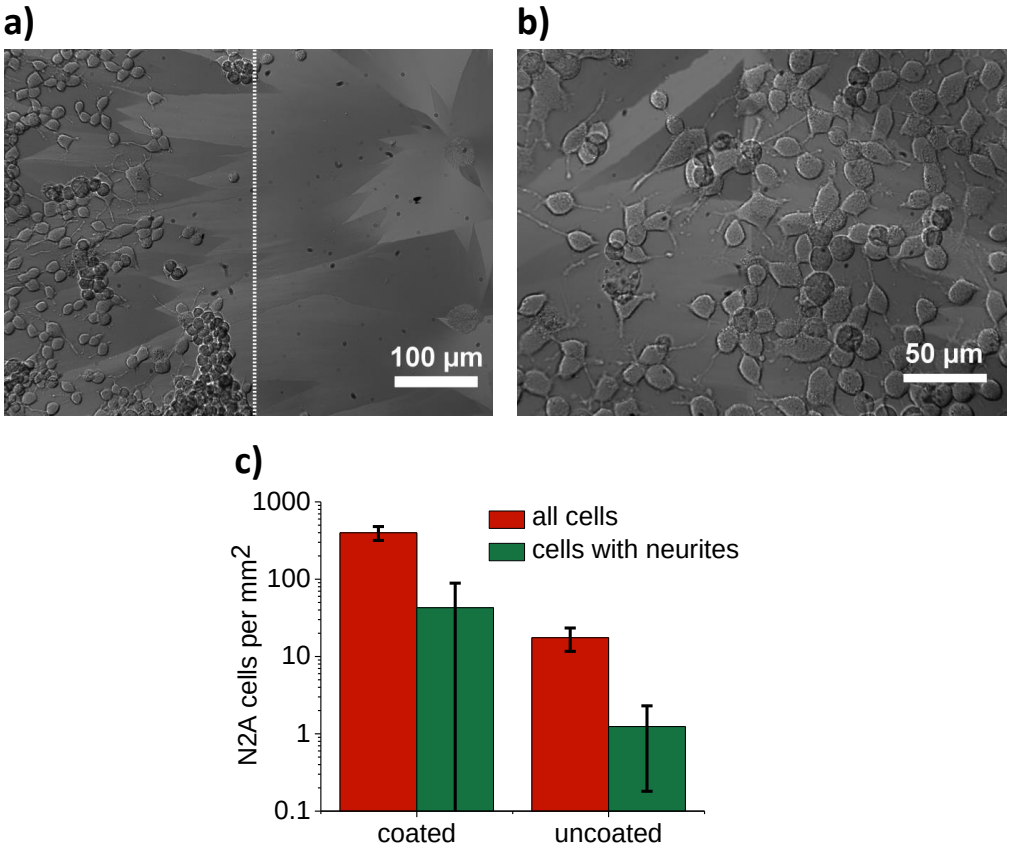

Figure 7.1: Cell growth characterization of N2A cells cultivated on coated (55 nm SiO_2) and uncoated areas of SQIB:PC60BM(7:1)/ITO(temicon)/glass (120 °C, 2h) devices in modified Ringer's solution. a) DIC microscopy image (2 days after seeding) shows the cell adhesion on coated (left side) and uncoated (right side) areas. b) DIC microscopy image gives a magnified overview of N2A cells attached to the silicon dioxide coating. c) Quantitative evaluation of the cell growth for coated and uncoated regions. Bar diagrams show the number of N2A cells (red bars) and number of N2A cells exhibiting neurites (green bars) per mm^2. The standard deviations are represented by error bars.

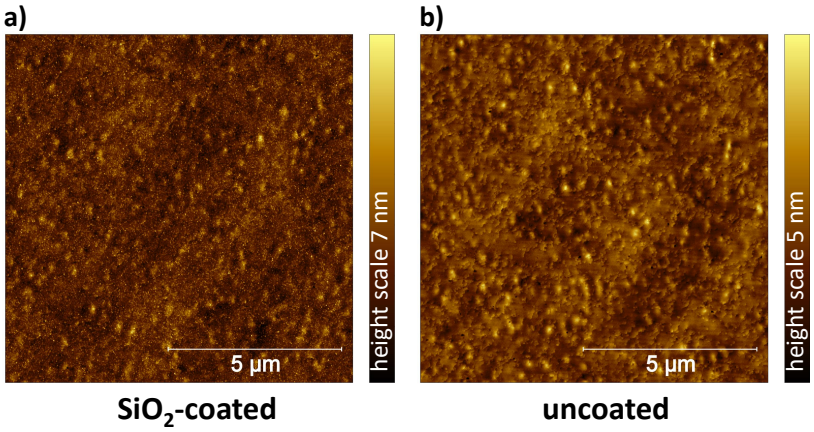

Figure 7.2: Atomic force microscopy images of a) coated (55 nm SiO_2) and b) uncoated region on a SQIB:PC60BM(7:1)/ITO(temicon)/glass (120 °C, 2h) device recorded in intermittent contact mode. (Samples were prepared by Oliya S. Abdullaeva and the AFM measurements conducted by Frank Balzer.)

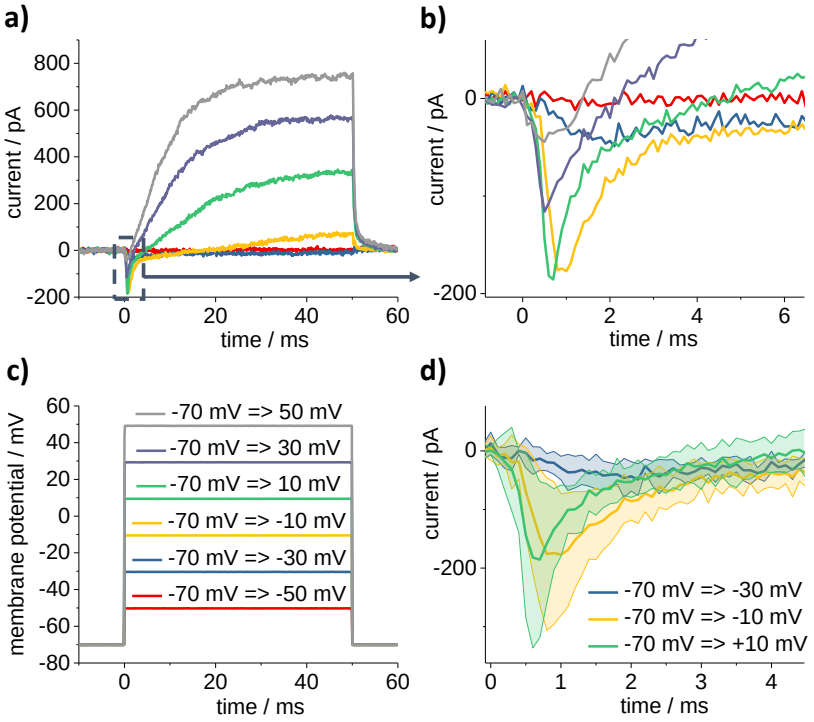

Figure 7.3: Artificial depolarization tests conducted in the dark on N2A cells grown on SiO_2(55 nm)/SQIB:PC60BM(7:1)/ITO(temicon)/glass (120 °C, 2h) devices. A variety of 50 ms artificial depolarization pulses were applied to the N2A cells as shown in Figure 7.3 c). Figure a) gives an overview of negative inward sodium and positive outward potassium currents measured in voltage-clamp mode. A close-up of the sodium currents induced by the artificial depolarization can be found in b). The current traces represent the average value of 7 N2A cells. All recordings were measured in modified Ringer's solution and normalized to 40 pF capacitance. In addition, Figure d) depicts three current traces for the following three depolarization steps ΔV: 40, 60 and 80 mV. Shaded areas represent standard deviations.

Voltage-gated ion channels require the membrane potential to be depolarized beyond a certain activation threshold to be activated. By performing artificial depolarization tests, this specific threshold can be determined as was shown in Chapter 5. This test needed to be repeated for the N2A cells grown on the dielectric coating. Firstly, it was crucial to check if the new device architecture disrupts the intrinsic properties of these ion channels. Secondly, since the salt concentration of the Ringer's solution was changed the N2A cells are forced to adapt to a new aqueous environment. Thus the excitability of the ion channels had to be ensured under these uncommon conditions. Recordings of artificially depolarized N2A cells demonstrated that their function was maintained despite the modifications (Figure 7.3). There was a noticeable decrease in the sodium current though, due to the reduced amount of sodium ions in the extracellular vicinity of the N2A cells. Typically, sodium inward currents can reach values up to 600 pA in standard Ringer's solution. According to the data in Figures 7.3 b) and d), a threshold potential of 60 mV was enough to activate fast sodium ion channels which is far below the 80 mV photoinduced depolarization (Figure 7.3 c)).

7.2 Activation of Voltage-Gated Sodium Channels

Hence this prompted further photostimulation experiments where the photoelectrical response of the N2A cells was measured in voltage-clamp mode without any injection of artificial depolarizing currents by the patch-clamp electrode. The photosensor was stimulated with 100 ms light pulses while the N2A cells were kept at a holding potential of -70 mV (Figure 7.4). The illumination time was extended from 10 to 100 ms in order to record any potential current response that occurs beyond 10 ms. Upon illumination the cells grown on the SiO_2 coating responded with very fast negative transmembrane currents, strongly resembling characteristic negative sodium inward currents (Figures 7.4 a) and b) blue data points). Two types of control experiments were designed to investigate the origin of the observed currents. A classical approach is to selectively block sodium channels in the N2A cells. If this were an actual opening of sodium channels, the current should diminish. QX-314 bromide is a selective blocker for sodium channels and has the advantage that it can be easily applied by adding it to the intracellular solution.[149] TTX, on the other hand, would alter the composition of the extracellular solution and could, therefore, interfere with the coupling mechanism. When the N2A cells were blocked with QX-314 bromide, they showed a significantly smaller current response (Figure 7.4 b) red data points). The residual signal that was detected even during the control experiment can probably be attributed to residual capacitive transmembrane currents that are of a passive nature and can not be compensated by the amplifier as is normally the case during artificial activation of ion channels. To ultimately verify the activation of sodium channels it was necessary to have a closer look at the current-voltage relationship of the current signals for individual holding potentials from -90 to +80 mV (Figure 7.4 c)). In doing so, the current minima of each measurement was determined and normalized to the highest value which in turn was set to -1. The current-voltage plot obtained from photostimulation matched the characteristic behavior of voltage-gated sodium channels which undergo three different states depending on the membrane potential: activated, closed and inactivated.[200,201] The most negative current value was recorded for a holding potential of -70 mV where the ion channels are situated in a closed state and can be readily activated by a photoinduced 80 mV depolarization. At more positive holding potentials the ion channels usually enter an

inactivation phase. Here, they can not be activated as they need to be hyperpolarized first. The hyperpolarization allows them to regain the closed state before they would be able to open again. This explains the gradual reduction of the current signal for holding potentials from -60 mV to +80 mV (Figure 7.4 c)). However, a decrease in current is also observed for -80 and -90 mV holding potentials. The reason for the decreased activity is probably that the ion channels require a depolarization beyond 80 mV to open. The current signals of N2A cells that were measured with the QX-314 bromide blocker were also evaluated for the same holding potentials (Figure 7.4 d)). This resulted in a completely altered current-voltage behavior. Although the current was not 0 pA for blocked N2A cells, the detected current minima did not show the activity typical for sodium channels. The stimulation mechanism was found to be caused by a photocapacitive coupling at the semiconductor-electrolyte-membrane interface. There was a direct temporal link between the photoinduced rapid transient displacement currents in the electrolyte and the fast response of the sodium channels. Furthermore, the transmembrane current in the N2A cell diminished upon omission of the ITO electrode from the SQIB:PC60BM sensor (Figure 7.4 b) grey data points).

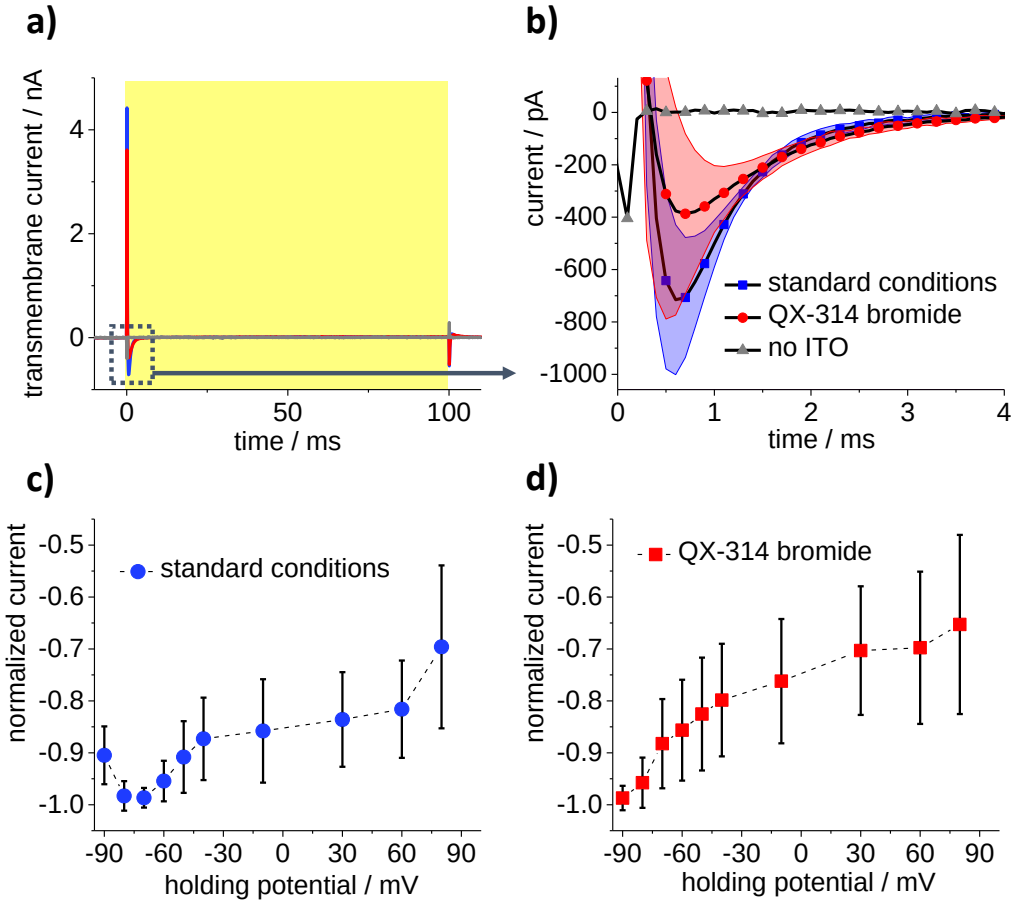

Figure 7.4: Activation of voltage-gated sodium channels in N2A cells grown on SiO_2(55 nm)/SQIB:PC60BM(7:1)/ITO(temicon)/glass (120 °C, 2h) devices. Figure 7.4 a) depicts a voltage-clamp measurement (holding potential -70 mV) conducted while simultaneously illuminating the device for 100 ms (yellow background, 180 mW, white LED, spot size 2.5 mm^2). All measurements were conducted in modified Ringer's solution. A sampling rate of 10 kHz was used during all recordings. Moreover, all data was normalized to a capacitance of 40 pF which is the average capacitance of all N2A cells that have been considered for data analysis. A close-up of the negative transmembrane current responses to the illumination pulse is shown in b) for the first 4 ms of the recording. This figure compares the current responses of N2A cells patch-clamped either with the standard intracellular solution (blue data points, number of measured N2A cells: N = 9) or an intracellular solution containing QX-314 bromide that selectively blocks sodium channels (red data points, number of measured N2A cells: N = 8). The grey data points represent a N2A cell grown on a photosensor device without an ITO electrode that was patch-clamped with a standard intracellular solution. During recording a live P/n correction was performed with following settings: min/max = -85 mV/-85 mV, number of leaks = 4, leak delay = -100 µs, leak size = 0.25, leak hold[mV] = -85. For the same N2A cells the photostimulation experiment was repeated for different holding potentials: -90, -80, -70, -60, -50, -40, -10 +30, +60 and +80 mV. In the next step, the minima of these photoinduced current responses were plotted for each holding potential. The resulting plots are shown in c) for N2A cells patch-clamped with a standard intracellular solution and in d) with an intracellular solution containing QX-314 bromide. Error bars and shaded areas are standard deviations.

7.3 Activation of Potassium Channels

To investigate the possibility of additional stimulation mechanisms that occur on a slower time scale a new photostimulation experiment was designed. The first step consisted of applying artificial 100 ms depolarization pulses (from -40 mV to +70 mV) to the N2A cells in voltage-clamp mode, to specifically address voltage-gated potassium channels (Figure 7.5 a)). Next, the depolarization protocol was run while simultaneously illuminating the sensor for 100 ms (Figure 7.5 b)). In the end, the same depolarizing step was repeated in the dark (Figure 7.5 c)). It needs to be pointed out that the current responses for all three steps were obtained from the same cell. Potassium channels respond very slowly, therefore only the average of the current signal from 50 ms to 95 ms was relevant in this case. The dots connected by dashed lines in Figure 7.6 represent the average current values of a single cell in 1.) dark, 2.) light and 3.) dark conditions. There was an increase in the current for the illuminated state before it returned to its initial value during the second dark phase (Figure 7.6 a)). The significance of the increase was verified by a Friedman test, the p-values are given in the caption of Figure 7.6. To rule out that the increase was merely due to necrosis only those measurements were considered for the evaluation where the leakage current varied only by 1-9 pA during the whole recording. It could be concluded that the outward currents were caused by an opening of potassium channels after they were selectively blocked with CsCl which in turn prevented a rise of the current signal during illumination (Figure 7.6 b)). A final control experiment was undertaken to determine the stimulation pathway. N2A cells grown on photoactive sensors lacking the ITO electrode showed the same activation of potassium channels (Figure 7.6 c)). Since devices missing an ITO electrode are incapable of generating capacitive currents an electrical stimulation mechanism as a potential cause for the activation was precluded. The most obvious explanation is a thermal-mediated activation that occurs due to the high light power of the illumination source that was used during photostimulation. However, the extent of the temperature increase needs to be determined in future studies.

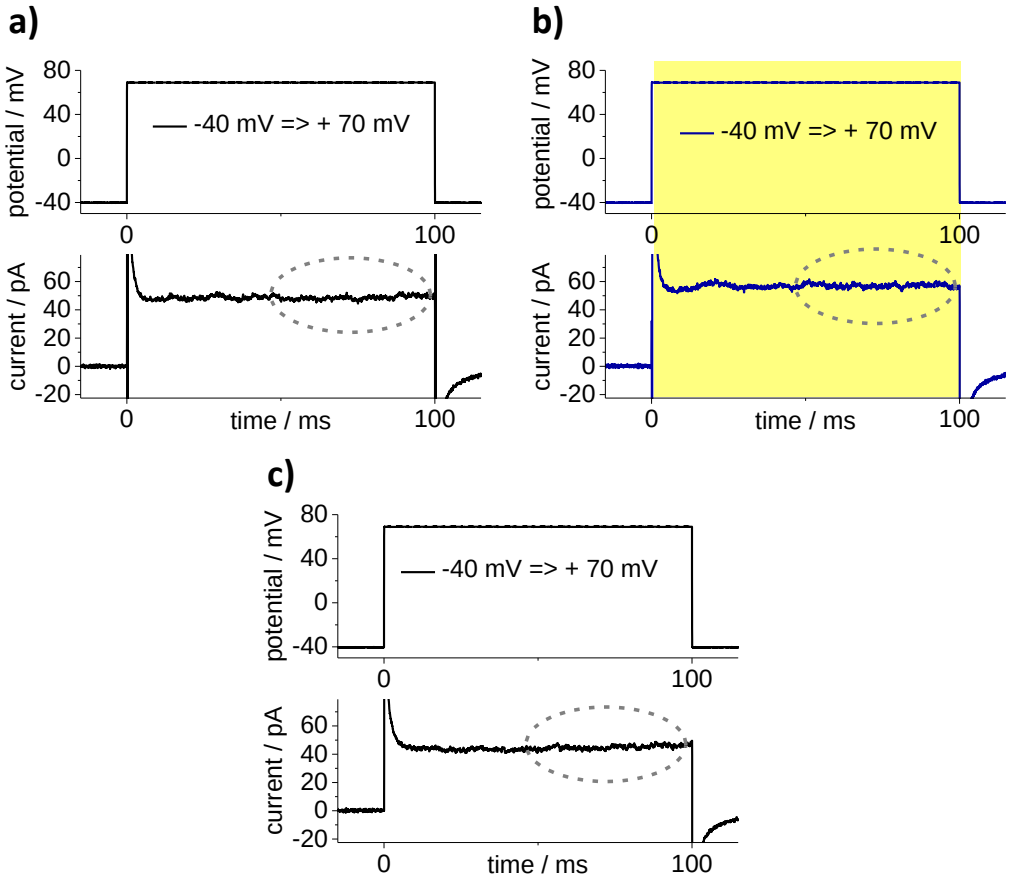

Figure 7.5: Exemplary voltage-clamp recordings of N2A cells grown on SiO_2(55 nm)/SQIB:PC60BM(7:1)/ITO(temicon)/glass (120 °C, 2h) devices. Each figure shows both the 100 ms artificial depolarization pulse (from -40 mV to +70 mV) that was applied to the N2A cells and their respective current responses to this stimulation in voltage-clamp mode. Experiments a) and c) were conducted in the dark whereas the measurement in b) was recorded while simultaneously illuminating the device for 100 ms (180 mW, white LED, spot size 2.5 mm^2), matching the length of the artificial depolarization pulse as is visualized by the yellow background. All measurements were conducted in modified Ringer's solution. The dashed circles show the range of the current response (from 50 ms to 95 ms) that was considered for further analysis (see Figure 7.6).

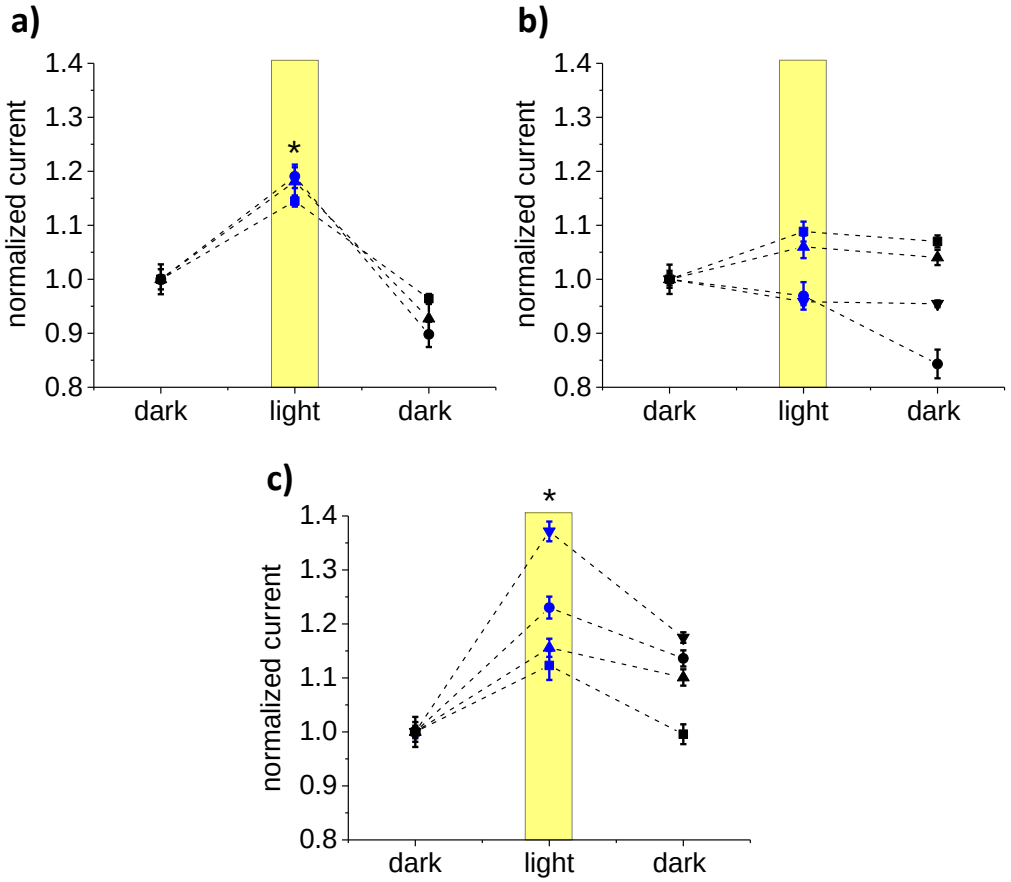

Figure 7.6: Analysis of the recordings shown in Figure 7.5. Here, the aim was to calculate the average current value for a time scale ranging from 50 ms to 95 ms as illustrated by the dashed circles in Figure 7.5. These average current values are represented by data points shown in Figures 7.6 a) to c). The experimental uncertainty is depicted by error bars. Data points connected by dashed lines stem from the same N2A cell. The denotations "dark-light-dark" in each figure indicate the sequence of experiments undertaken for each N2A cell. The data points shown in Figures 7.6 a) and b) stem from recordings conducted on N2A cells grown on devices with following architecture: SiO_2(55 nm)/SQIB:PC60BM(7:1)/ITO(temicon)/glass (120 °C, 2h). The difference between a) and b) is the type of intracellular solution that was used during the patch-clamp experiments: a) standard intracellular solution, b) intracellular solution containing CsCl in order to selectively block potassium channels. The control experiment presented in Figure c) was performed on N2A cells grown on devices lacking the ITO electrode: SiO_2(55 nm)/SQIB:PC60BM(7:1)/glass (120 °C, 2h). Here, the standard intracellular solution without CsCl was used. The $p < 0.05$ differences between light and dark states are marked by the asterisks. Following p values were obtained in the Friedman test with Dunn's correction for multiple comparisons: a) $p = 0.0278$ and c) $p = 0.0417$. Since both p values obtained for a) and c) are lower than 0.05 the differences in the average current values between dark and light states can be considered as significant. (Friedman test was performed by Karin Dedek.)

Chapter 8

Discussion

Since the beginnings of bioelectronics, especially in the field of retinal implants, there has been a constant effort to resolve and optimize the working principle. Several key milestones have been achieved in this project that demonstrate the feasibility of several photostimulation mechanisms that occur on a cellular level. This chapter discusses the main results and compares them with previous studies.

8.1 Capacitive Coupling

The idea of establishing a dynamic capacitive mechanism for organic semiconductor-electrolyte interfaces is not new and has been successfully demonstrated in studies involving several types of organic semiconductors.[59,72,100,119] However, they fail to address the impact that the capacitive coupling has on voltage-gated ion channels, the basis for capacitive driven neuronal stimulation as discussed by Fromherz et al. for silicon-based devices.[93,94,98] This thesis bridges the gap by systematically showing on a cellular level how photoinduced capacitive displacement currents at an organic semiconductor-electrolyte interface are directly linked to a substantial depolarization of the cell membrane and subsequent activation of fast responding voltage-gated sodium channels.

In order to understand the underlying mechanism of this photoinduced capacitive stimulation pathway, it is necessary to take following models into consideration: the *RC*-circuit model developed by Hodgkin and Huxley to explain the electrical properties of neurons and the Helmholtz double layer model for electrode-electrolyte interfaces. The events taking place in the electrolyte during illumination can be explained by modeling the organic semiconductor-electrolyte interface as a double layer capacitor. The transient character of the ON-current signals measured within the Ringer's solution signifies the rapid movement of ionic species in the electrolyte. This type of current can be designated as a displacement current without the involvement of Faradaic currents which would rather have resulted in a steady-state current signal. A drift of ionic charge carriers in the electrolyte that correlates with the light stimulus and only occurs in the presence of an electrode suggests a formation of local space charges within the organic semiconductor thin film resulting in an electric field which eventually polarizes the electrolyte. This polarization, in turn, leads to a rapid redistribution of ionic species in the electrolyte and local charge accumulation. The end result is the formation of a Helmholtz double layer at the interface between the organic semiconductor and the Ringer's solution when the double layer capacitor is fully charged. The OFF-current response with reversed polarity shows that this process is reversible. Upon termination of the light pulse, the accumulated charge carriers dissipate rapidly back into the opposite direction restoring the initial charge distribution in the dark before the light stimulus. This capacitive behavior is in good agreement with previous studies conducted on P3HT-electrolyte interfaces by Narayan, Hanein et al./ Lanzani et al./Ghezzi et al. and organic pigment-electrolyte photocapacitors developed by Glowacki et al., showing similar ON- and OFF-transient photoresponses upon photostimulation.[72,100,119]

The membrane of the N2A cells can perceive the displacement currents and the accumulation of charge carriers as can be seen in the photoinduced alterations in their membrane potential. The polarity of the accumulated charge is crucial and determines if the membrane potential is depolarized or hyperpolarized. The positive shift occurring in the membrane potential at the onset of illumination indicates that negative ionic charge carriers accumulate in the vicinity of the cell membrane. As a result, the inside of the cell becomes more positive compared to the extracellular medium, which can be measured as a depolarization.

This process is reversed at the offset of the light pulse as the accumulated negative charge carriers dissipate away from the vicinity of the cell, causing a hyperpolarization. The progression of the depolarization signal exhibits a typical behavior that is associated with the charging and discharging of a cell membrane capacitor. However, in contrast to an artificial steady-state electrical stimulus, the photoinduced transient stimulation pulse has a very short duration. Therefore, the depolarization phase is followed by a rapid drop of the voltage signal to the initial resting membrane potential. The membrane capacitor discharges too rapidly before the membrane potential can reach a constant voltage plateau. These rapid photoinduced alterations in the membrane voltage trigger passive transmembrane currents within the membrane without having any effect on the conductance of the ion channels according to following equation: $I = C_{\mathrm{m}}(\mathrm{d}\,V_{\mathrm{m}}/\mathrm{d}t)$. According to the Hodgkin-Huxley model, I represents the flow of capacitive currents that arise due to change in the membrane potential $\mathrm{d}\,V_{\mathrm{m}}$ that occurs during the charging and discharging of the membrane double layer capacitor.[133] Photoinduced passive transmembrane currents have also been reported for HEK cells grown on organic pigments.[86] Evidently, the ability to induce passive electrical cell responses is a common feature among organic semiconductors. Moreover, it has been shown that P3HT/ITO devices can also evoke fast depolarization signals in HEK-293 cells upon illumination. But the order of magnitude was merely around 0.3 mV.[85]

In view of these existing studies in the field of organic-based photovoltaic artificial retinas this thesis provides yet highly significant results since a depolarization in the range of 80 mV, and a successive direct activation of voltage-gated sodium channels via a photocapacitive mechanism have not been reported before for organic semiconductors. The studies focusing on P3HT, organic pigments and carbon nanotubes have shown that photostimulation can indeed elicit action potentials within degenerated retinas that are grown on these devices.[59,72,74,82,100] However, a direct recording of sodium channels was not provided that would offer an explanation for the occurrence of the action potentials. Key parameters were identified that need to be modified step-by-step in order to reach the activation threshold of sodium channels. In doing so, it was crucial to take the role of the double layer capacitance as well as the resistance of the electrolyte into account. Both constitute the RC time constant and determine the time it takes to charge and discharge the double layer capacitor.

It is possible to optimize both parameters by adapting the concept of the EOS (electrolyte-oxide-semiconductor) capacitor and modifying the Ringer's solution.[93,94,98] The capacitance was enhanced upon inclusion of an insulating silicon dioxide layer on top of the photoactive SQIB:PC60BM film as evidenced by longer decay times for the ON-transient displacement currents. During operation of the photoreceptor, the insulator enhances charge separation between the organic thin film and the electrolyte, causing slower charge and discharge times for the double layer capacitor. A further decrease in the conductivity of the electrolyte was achieved by changing the salt concentration of the Ringer's solution which also contributes to a longer time constant. These modifications contributed to an enhancement of the depolarization signal beyond a threshold value and to an increase in the discharge time of the voltage signal, meaning that the membrane potential maintains depolarized for a longer period of time. Though at this point only impedance spectroscopy and cyclic voltammetry measurements would be able to provide definite quantitative values for the double layer capacitance of the SQIB:PC60BM-oxide-electrolyte interface. These type of measurements go beyond the scope of this thesis but should be part of future investigations. On the other hand, the duration of the photoinduced transient stimulation pulse is too short to activate potassium channels that reach a maximum current plateau after 40 ms. As will be discussed later, non-electrical events at the interface occur on such slow time scales that trigger an activation of these channels.

Regarding the long-term applicability of neuroprosthetics, the amount of charge injection provided by the electrode cannot be arbitrarily large.[89,202] Standard measures for the safety and efficiency of electrical stimulation are the threshold charge and threshold charge density, defined as the least charge necessary for depolarization of the neuronal tissue up to a potential where action potentials are evoked due to the activation of voltage-gated ion channels.[203] A recent study determined the individual thresholds for single retinal ganglion cells (RGC).[203] The charge densities were found to depend strongly on the electrode size. In general, ganglion cells that were stimulated with larger electrodes required lower charge injection to be activated. Values ranging between 8-73 µC/cm^2 were measured for 4x4 electrodes with an area of 78400 µm^2, whereas the threshold charge injection did not exceed the range of 4-40 µC/cm^2 for large 16x16 electrodes with an area of 125000 µm^2.

In the case of the squaraine-based photosensor, a photoinduced threshold charge injection of about 8 pC evoked the activation of sodium channels. While calculating the charge density, the size of the recording patch-clamp electrode tip needs to be considered which has a size of 1.8 μm^2. Thus the charge density would amount to 400 $\mu C/cm^2$, exceeding the threshold for single RGCs by far. The charge density might be even higher. Measuring the charge accumulation with a patch-clamp electrode underestimates the actual charge injection area because the light spot size, as well as the N2A cell, are much larger than the diameter of the recording electrode tip.

The strategies that have been applied here during the optimization also included tuning the device morphology towards highly crystalline film structures with complete coverage of the underlying ITO electrode. It was found that spin coated blends containing both SQIB donor and PC60BM acceptor material require high annealing temperatures to undergo a phase separation resulting in a bilayer architecture which was beneficial for the device performance. A recent study by Glowacki et al. has also demonstrated the importance of a donor-acceptor bilayer stacking of organic pigments for the development of photocapacitors.[100] The device included however a metal electrode that needed to be partially in direct contact with the electrolyte to achieve a capacitive coupling.[100] In contrast, encapsulating the SQIB:PC60BM sample and further improving the platelet morphology by inhibiting the formation of pinholes and large fern areas that expose bare ITO in some regions enhanced the charge injection and transient capacitive behavior. In addition to maximizing the magnitude of the charge accumulation and photocurrent, the polarity of the current response plays a big role in the photostimulation of the cell membrane. It was found that the polarity is determined by the composition of the photoactive layer that is directly in contact with the electrolyte. Negative photocurrents were measured above large PC60BM domains and pure PC60BM thin films, whereas a positive polarity was obtained for SQIB-rich structures, indicating that the photoinduced double layer capacitance can be adjusted to give the appropriate charge depending on whether a depolarization or hyperpolarization is intended. Narayan et al. experimented with bulk polymer heterojunction-electrolyte interfaces and were able to control the polarity of the transient photovoltages by varying the thickness of the photoactive P3HT:N2200 layer (N2200 functioned in this study as acceptor material).[73–75,119] The photovoltage scaled with the thickness.

Very thick layers showed the largest responses while the polarity was reversed for the minimum thickness. The direction of the illumination also affected the polarity, which switched from a positive to a negative transient voltage response upon changing from the electrolyte to the ITO side.[119] This was not observed for the SQIB:PC60BM photoreceptor, the displacement current exhibited a positive polarity for both directions. Neither was there any observable dependence of the polarity on the film thickness. The squaraine-based device displayed the opposite behavior where the photocurrent response was diminished for thick drop casted films.

Aside from modifications to the device morphology, architecture, and electrolyte composition, a substantial part of the improvements should be attributed to the application of high powered light sources in the unphysiological range. The activation of sodium channels was achieved at a light intensity as high as 72 mW/mm^2. This is however not applicable in everyday life for the natural human retina, as the outdoor daylight intensity amounts to merely 0.001 mW/mm^2.[204] Only direct sunlight would provide enough intensity for sufficient neurostimulation of the degenerated retina. This case would, however, cause severe photodamage to the retina.

8.2 Non-Capacitive Coupling (Thermal)

As described before in the introduction, there is a wide range of non-capacitive stimulation pathways that might potentially occur at the organic semiconductor-electrolyte-cell interface. Non-electrical neurostimulation has been the subject of numerous studies.[85,86,128,129] One of them involved devices consisting of either P3HT, P3HT:PC60BM or photoresist.[85] The photostimulation of HEK-293 cells grown on all types of films evoked a transient depolarization of the cell membrane followed by a hyperpolarization after the offset of the light pulse. Devices carrying an ITO electrode additionally induced a fast depolarization spike independent of this subsequent slower transient depolarization signal. Two distinguishable temporal signals are also evident for the squaraine-based photoreceptor.[85] The results presented here elucidate that long illumination times trigger a second signaling mechanism on a time scale beyond 50 ms. Potassium ion channels respond to this stimulation with an outward current.

The true nature of this stimulation mechanism that obviously activates a voltage-gated potassium channel without the involvement of a capacitive coupling has yet to be comprehended in future studies. Some commonalities are noticeable for both cell types though, HEK-293 as well as N2A: non-electrical activation appears on a rather slow time scale upon photostimulation using high light intensities, and it is observed even without the presence of an electrode.[85,86] Several possible mechanisms have been proposed.[85–87] The above-mentioned depolarization of HEK-293 cells has been attributed to a thermal coupling, a universal phenomenon ascertained for the optical stimulation of oocytes, mammalian cells, artificial bilayers, and artificial neurons by Shapiro et al.[128,129] This study explains the activation mechanism during infrared stimulation. According to this investigation, the aqueous environment absorbs the infrared light resulting in a local temperature rise (approximately $\Delta T = 22.2 \pm 0.6$ °C).[128,129] The cell membrane responds to this heating with a change in the electrical capacitance which is responsible for a substantial depolarization of the cell. Lanzani et al. could show that this theory can also be applied to P3HT-electrolyte interfaces.[85] Their study demonstrated a temporal correlation between a temperature increase (approximately $\Delta T = 7$ °C) at the P3HT-electrolyte interface and a slow transient change in the membrane potential. Furthermore, they showed the possibility of hyperpolarizing the membrane potential with illumination times longer than 20 ms and as long as 200 ms.[85] In addition, the degradation of the SQIB:PC60BM blend observed during the stability tests is indicative of redox reactions at the interface which result in the consumption of the organic material. Therefore, a mechanism involving such chemical reactions at the interface should not be excluded as a potential reason for the activation of the potassium channels.[47]

Chapter 9

Conclusion and Outlook

The objective and challenge of this thesis were to figure out if and how artificial organic semiconducting devices communicate with biological species. Establishing a functional communication pathway is an essential centerpiece in the development of future organic-based neuronal prosthetics. Without knowledge of the detailed mechanistic processes at the interface between device and living tissue, it is difficult to build implants with a precise target. This thesis attempts to gain insight into these events at bioelectronic interfaces on a fundamental level focusing on voltage-gated sodium and potassium channels. Several key milestones have been reached that allow the following conclusions:

⇒ **Squaraine-based artificial photoreceptor can indeed communicate electrically with N2A cells via a fast direct capacitive coupling:**

The study demonstrates in a simple proof of principle investigation that photostimulating squaraine-based samples can elicit an electrical but yet weak signal by the cell membrane in the form of depolarization and passive transmembrane currents via capacitive coupling. The patch-clamp technique provides a unique and basic electrophysiological tool to investigate these electrical responses. Pure capacitive signaling between biological tissue and organic electronics is considered as an ideal mechanism for bioelectronics intended for a safe stimulation. The second half of the project showed that this capacitive coupling can be enhanced.

The optimization procedure entailed learning more about the structure-property relationship of the donor-acceptor blend film and eventually tailoring the morphology to obtain a preferably high photocurrent to maximize the depolarization signal of the N2A cells. The most intriguing concept was to include a dielectric layer that encapsulates the photoactive layer and increases the amount of injected charge which demonstrates that the idea of an electrolyte-oxide-semiconductor (EOS) capacitor, implemented by Fromherz et al. for silicon-based bioelectronics, can also be applied to organic bioelectronics.[93,94,96,98] Following these optimization steps, the ultimate goal of implementing a direct capacitive signaling mechanism leading to a subsequent direct activation of sodium ion channels was reached. This project was able to affirm the possibility of an electrical communication pathway based on capacitive coupling for pure organic semiconductors.

⇒ Cellular neuronal models provide an ideal platform for fundamental mechanistic studies / the stimulation pathway at the organic biointerface is not limited to capacitive coupling: artificial photoreceptor triggers a second active cell response due to slow nonelectrical processes:

This study also underlines the need for fundamental investigations at the core of neurostimulation, simplistic neuronal cell lines that express voltage-gated ion channels. Merely recording action potentials in very complex neuronal tissues does not suffice to make statements about the stimulation mechanism because photoinduced action potentials can also originate from nonelectrical mechanisms that occur independently from the capacitive coupling. Either a thermal or chemical coupling were shown here to activate slow responding voltage-gated potassium channels. Such adverse effects are caused by high light intensities that were required to induce a sufficient capacitive coupling.

Outlook

According to the results shown here, a fast direct capacitive activation of fast-responding sodium channels is possible. However, the squaraine photoreceptor presented here supports a capacitive coupling mechanism only at very high unphysiological light intensities. An important issue remains: how do these results obtained by lab-scale experiments relate to potential future organic neuroprosthetics that can be employed as retinal implants? Organic semiconductor materials do show beneficial properties that make them useful alternatives compared to prosthetics consisting of inorganic devices. This thesis validates their ability to directly target voltage-gated sodium channels via electrical coupling. There is however no guarantee that the same organic materials will abide by similar working mechanisms once implanted into a more complex environment. Testing the capacitive coupling on more advanced neuronal networks should be part of upcoming investigations. The SQIB:PC60BM sensor requires a lot of improvement in long-term stability and efficiency. Future studies should focus on gaining sufficient charge output with safe ambient daylight. Combining organic semiconductors with charge injecting polarizable metal electrodes has been recently proposed by Ghezzi et al. This solution allows neurostimulation with lower light intensities.[59]

Nevertheless, although organic semiconductors face a lengthy period of development until they can be approved for clinical trials, the findings presented in this thesis emphasize that they already meet the basic demands of neurostimulation under lab-scale conditions.

Chapter 10

Experimental Section

Synthesis of SQIB

The synthesis of SQIB was conducted at the University of Bonn by Dr. Matthias Schulz. The synthesis protocol has been published[184] and is also described in Dr. Matthias Schulz's doctoral thesis, entitled "Synthese, Eigenschaften und Anwendung von Squarainen als Komponente in Photodioden" (University of Bonn, 2018).

Device Preparation

Device preparation of samples shown in Chapter 5: The photoactive layer was fabricated by solution processing in an inert atmosphere. First, a 6 mg/mL solution of SQIB was prepared in chloroform (Sigma-Aldrich, stabilized with amylene). After stirring overnight, 6 mg PC60BM (Solenne) were added. This blend solution with a mixture ratio of 1:1 and a total concentration of 12 mg/mL was stirred overnight and spin coated onto ITO/glass substrates that had a size of either 10 x 10 mm or 25 x 25 mm in an inert atmosphere, under following spin coating settings: 950 rpm, ramping 0, 1 sec. Before spin coating, the ITO/glass substrates (sheet resistance: 15 $\pm$ 2 Ω/sq) were cleaned with distilled water. Nitrogen was used to blow-dry the substrates which were eventually etched with oxygen plasma for 10 min. After spin coating, the devices were annealed at 180 °C for 2 hours.

During the course of the optimization described in Chapters 6 and 7, the procedure of device preparation was modified. The photoactive layer was fabricated by solution processing. In an inert atmosphere, separate 6 mg/mL solutions of SQIB and PC60BM were prepared in chloroform

(Sigma-Aldrich, stabilized with amylene). After stirring overnight, both solutions were blended with varying mixture ratios. This blend solution was stirred overnight and spin coated onto ITO/glass substrates that had a size of 15 x 15 mm, under following spin coating settings: 950 rpm, ramping 0, 1 sec. Before spin coating, the temicon ITO/glass substrates (sheet resistance: 8 ± 2 Ω/sq) were cleaned with distilled water and isopropanol. Nitrogen was used to blow-dry the substrates which were eventually etched with oxygen plasma for 10 min. The devices were annealed at 120 °C for 2 hours after spin coating.

Cell Culture

10 mL of a cell culture medium, containing 50 mL Dulbecco's modified Eagle's Medium 2x (Merck Millipore), 2.7 mL sodium bicarbonate (Merck Millipore), 1 mL 4-(2-hydroxyethyl)-1-piperazineethanesulfonic acid (HEPES) buffer (Merck Millipore), 1 mL penicillin/streptomycin (Merck Millipore), 2 mL L-glutamine, 10 mL fetal bovine serum (Merck Millipore) and 33.7 mL ultrapure water (Merck Millipore), was used to store the N2A cells in an incubator set to 37 °C with 5 % CO_2. The trypsinization of the N2A cells was carried out once a week with 2 mL trypsin (Merck Millipore). This step was followed by seeding of the N2A cells onto the devices with a density of 10^4 (cell density). 3 days after seeding, the cells attached to the device were removed from the cell medium and measured after placing them into Ringer's solution. During the course of the thesis, the seeding procedure was modified. Prior to the seeding step, the cells were additionally diluted 5 days after trypsinization. The density was increased to 10^5 (cell density) to reduce the incubation time to 2 days.

Silicon Dioxide Coating

Silicon dioxide was purchased from MaTecK GmbH (silicon(IV) oxide/99.99 %). The annealed devices were placed onto a sample holder for evaporation and covered with an evaporation mask, resulting in partially covered devices. The evaporation was conducted in a Pfeiffer PLS 500 chamber via electron-beam deposition under following conditions: rates ranging from 0.01 to 0.3 nm/s and a power varying from 90 to 140 W.

Patch-Clamp Setup and Experiments

The setup consisted of an upright DM LFS Leica microscope with a polarizing microscope filter (Pol 513711 Leica/Leitz), a differential interference contrast (DIC) slider (D1 555063 Leica) and an analyzer slider (L ICT/P 555045 Leica/Leitz). The measurements were conducted with either a 20x or 40x objective with Nomarski optics (Leica). The images of the N2A cells were taken using a 2000DC CCD digital camera (QImaging Retiga), which was mounted on top of the microscope. A Live Acquisition 2.4 software was employed to save the images which were further analyzed with Fiji and ImageJ software.[197,198]

All patch-clamp and transient photocurrent recordings were performed using a HEKA EPC 9 double patch-clamp amplifier. Furthermore, a Bessel-filter at 2.9 kHz was applied and the capacitance of the electrode and cell membrane compensated with the C-fast and C-slow functions, respectively.

The patch-clamp electrode consisted of a glass micropipette filled with an inserted Ag/AgCl wire. A horizontal electrode puller (P97, Sutter, Novato, CA) was used to fabricate the micropipettes freshly out of borosilicate glass (1.5 mm o.d., Hilgenberg GmbH, Malsfeld, Germany). A pipette holder (D (diameter) = 1.5 mm, HEKA, Lambrecht, Germany) was used to connect the Ag/AgCl wire to the HEKA headstage which was further connected to the HEKA EPC 9 amplifier. The HEKA headstage was further equipped with a second Ag/AgCl wire, that was inserted together with the recording glass microelectrode into the electrolyte and functioned as a reference electrode. The wires had to be chlorinated regularly with a 3 M $FeCl_3$ solution. During transient photocurrent measurements, the tip of the patch-clamp electrode was placed above (approximately 3 µm) the blend film surface. In contrast to patch-clamp recordings, the patch-clamp electrode here was filled with the Ringer's solution that had the same composition as the bath solution.

N2A cells were recorded in whole-cell configuration with an intracellular solution composed of (in mM): 140 KCl, 1 $CaCl_2$, 2 $MgCl_2$, 11 ethylene glycol-bis(β-aminoethyl ether)-*N*,*N*,*N*',*N*'-tetraacetic acid (EGTA), and 10 HEPES (pH was adjusted to 7.4 with 1 M NaOH).

In order to selectively block potassium channels, the intracellular solution included CsCl (in mM): 120 CsCl, 1 $CaCl_2$, 2 $MgCl_2$, 20 TEA-Cl, 11 EGTA, and 10 HEPES (pH 7.2).

Intracellular solution used for selectively blocking sodium channels consisted of (in mM): 100 CsOH, 100 gluconic acid, 10 Na-HEPES, 5 EGTA, 5 tetrabutylammonium (TBA)-Cl, 5 Qx-314-Br, 3 Mg-ATP, 0.5 $MgCl_2$, 0.5 $CaCl_2$ and 0.5 Na-Guanosintriphosphat (GTP) (pH 7.25 (CsOH)).[149]

Compositions of the standard and modified Ringer's solution:
The standard extracellular Ringer's solution contained (in mM): 137 NaCl, 5.4 KCl, 1.8 $CaCl_2$, 1 $MgCl_2$, 10 D-glucose, and 5 HEPES (pH adjusted to 7.4 with 1 M NaOH). The concentrations of NaCl and KCl were altered for the modified Ringer's solution: 50 mM NaCl and no KCl.

Clampfit (Molecular Devices, LLC), Nest-o-Patch[205], Origin (OriginLab Corporation) and Matlab (The MathWorks Inc.) were used for data analysis.

TTX Test

The TTX experiments were conducted by diluting 100 µL of 1 mM tetrodotoxin citrate (Tocris Bioscience, Cat. No. 1069) in 100 mL H_2O in order to obtain a concentration of 1 µM. A pump (Ismatec, Wertheim, Germany) was used to perfuse the diluted TTX solution into the Ringer's solution.

Illumination Sources used for Patch-Clamp and Transient Photocurrent Recordings

The light source that was used for the experiments in Chapter 5 consisted of a 150 W xenon high stability lamp and a monochromator with a spectral width of 15 nm (Polychrome V, Till Photonics, Germany). The illumination parameters e.g., illumination time and wavelength were set via a Live Acquisition 2.4 software (Till Photonics). The setup also included an optical UV/vis quartz/quartz fiber (Till Photonics, Germany) and a 90R/10T beam splitter (400-700 nm, AHF, Germany). A 20x water-immersion objective mounted to the Leica microscope illuminated the samples across the electrolyte. Figure 10.1 shows the light powers, spot sizes and light intensities for various wavelengths. The light powers for each wavelength were measured with a S170C low-power microscope slide power meter sensor head which was connected to a PM100D power meter (Thorlabs, US). To this end, a drop of Ringer's solution was placed on top of the sensor head.

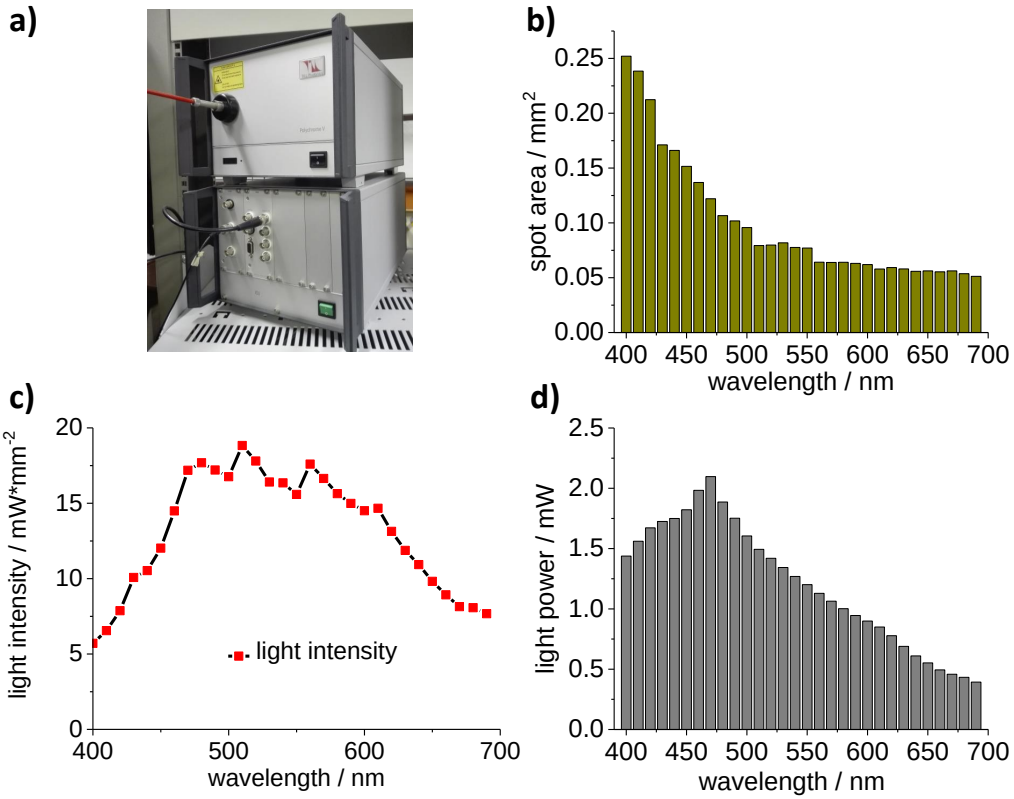

Figure 10.1: Characterization of the monochromatic light source used for photostimulation experiments that were presented in Chapter 5. a) Image of 150 W xenon high stability lamp, Polychrome V monochromator and Till Photonics quartz fiber (red cable). b), d) Measured light spot sizes and light powers for specific wavelengths. c) Calculated light intensities.

The photostimulation measurements shown in Chapters 6 and 7 were conducted with a mounted warm white LED (Figure 10.5) (Thorlabs MWWHLP1, color temperature: 3000 K, minimum power output: 2000 mW) and a mounted 625 nm LED (Figures 10.2, 10.3, 10.4) (Thorlabs M625L4, minimum power output: 700 mW). A DC 2200 LED Driver was used as a power source for both LEDs. The pulse length, LED drive current, LED brightness (0% - 100% of LED maximum current) were set using the pulse mode of the LED driver. In order to serve as trigger source, the LED driver was connected to the trigger input of the HEKA EPC 9 amplifier.

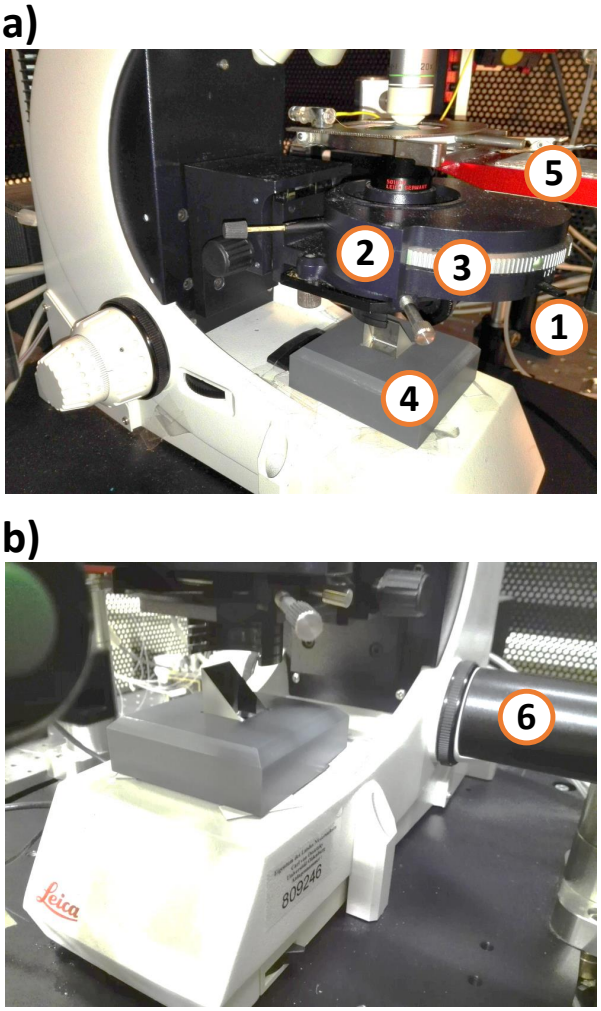

Figure 10.2: Experimental photostimulation setup that was applied in Chapters 6 and 7. a), b) 1: aperture diaphragm, 2: condenser, 3: bright field filter, 4: mirror, 5: patch-clamp sample holder table, 6: light source.

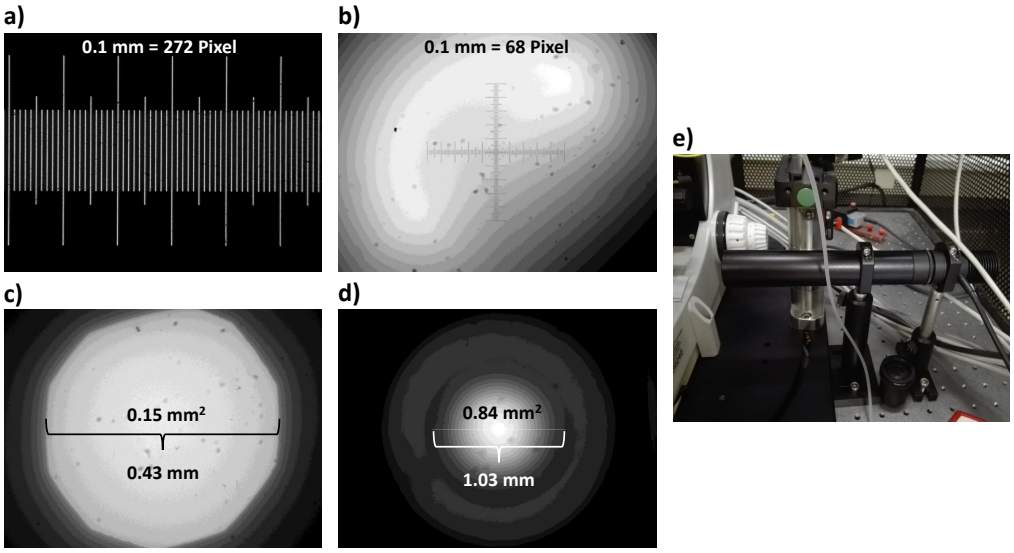

Figure 10.3: 625 nm LED alignment I. a) and b) Calibration standards used in order to calculate the diameter of light spots. Images were recorded with either a a) 20x objective or b) 5x objective and saved with Live Acquisition 2.4 software and further analyzed with Fiji and ImageJ software.[197,198] Images of light spots for two configurations: c) 6 mm iris diaphragm, spot size: 0.15 mm^2 and d) without iris diaphragm, spot size: 0.84 mm^2. e) Image of illumination setup for 625 nm LED that is mounted onto the optical table and equipped with an iris diaphragm and a lens tube.

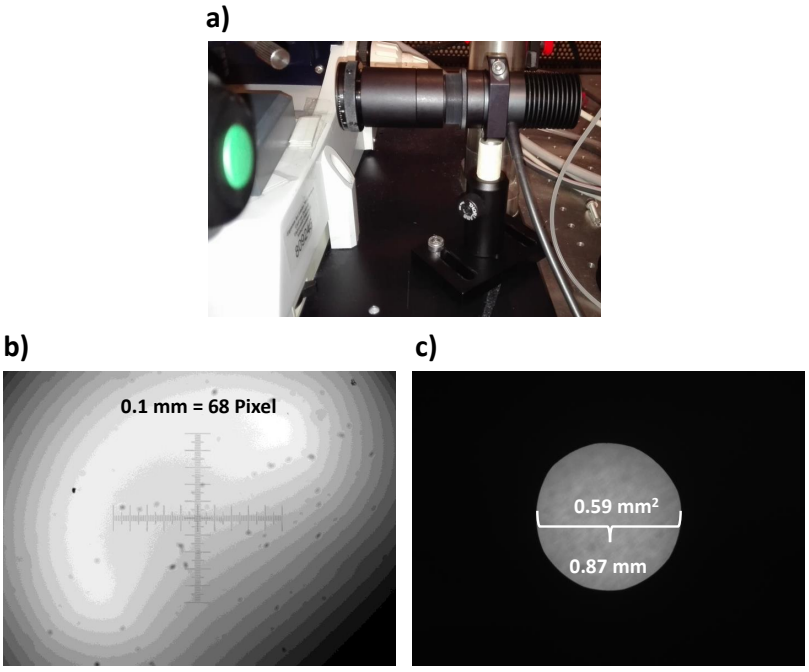

Figure 10.4: 625 nm LED alignment II. a) Experimental setup showing the 625 nm LED mounted onto the microscope table equipped with an iris diaphragm and a shorter lens tube. b) Image of calibration standard used for determining the diameter of the light spot taken with a 5x objective. c) Image of light spot for following configuration: 12 mm iris diaphragm, spot size: 0.59 mm^2.

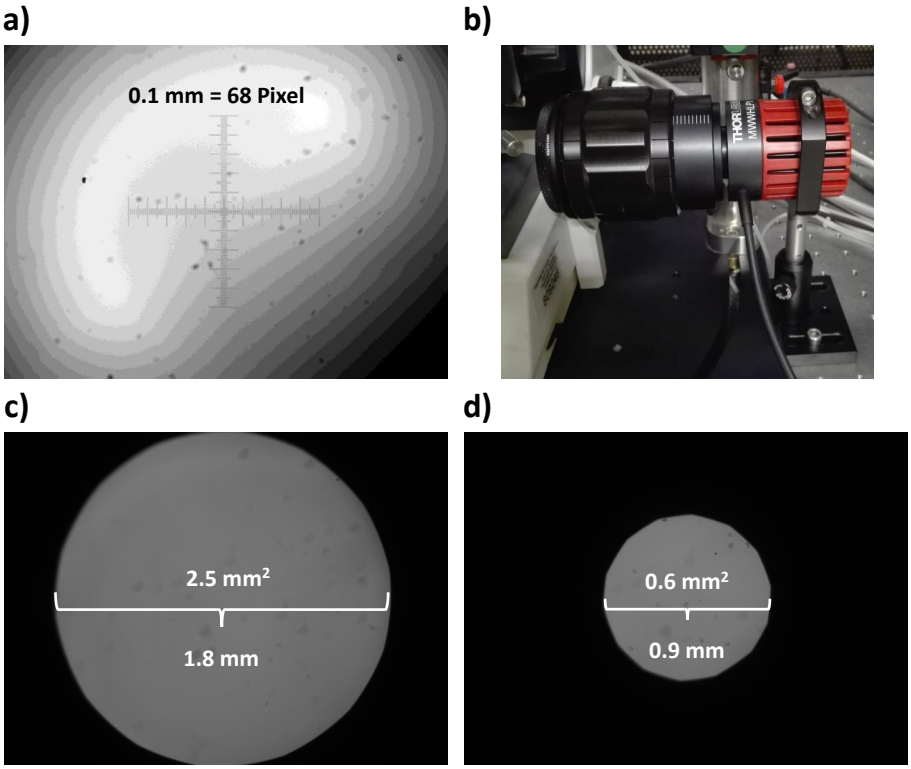

Figure 10.5: Alignment of white LED light source. a) Image of calibration standard recorded with a 5x microscope objective. b) Image of the experimental setup showing the white LED which is mounted onto the microscope table. Two light spots adjusted with an iris diaphragm with areas of c) 2.5 mm^2 and d) 0.6 mm^2 were obtained.

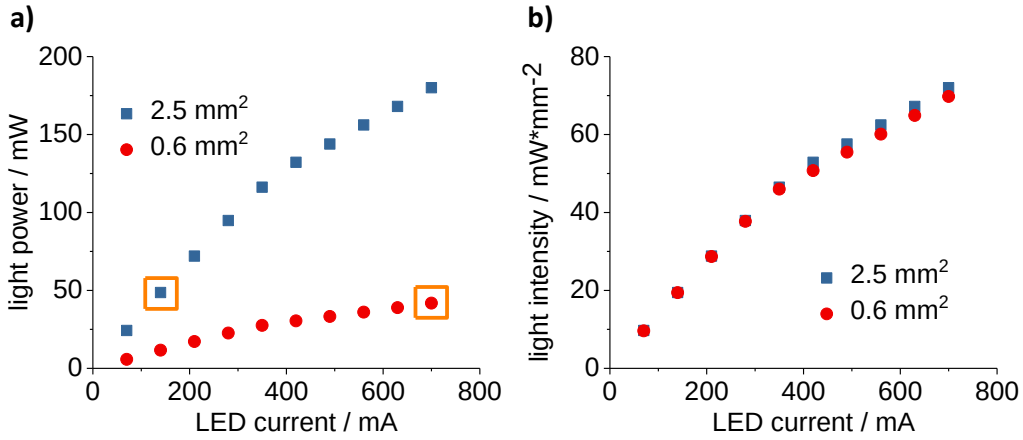

Figure 10.6: Characterization of white LED. a) Light powers measured for various LED currents using light spots I (blue data points, 2.5 mm^2) and II (red data points, 0.6 mm^2). b) The corresponding light intensities calculated for both light spots. Orange boxes hightlight data points in a) for both light spots that exhibit approximately the same light powers: 42 mW (0.6 mm^2) and 48 mW (2.5 mm^2). Light power is defined as the photon energy per unit time. On the other hand, light intensity is given by the light power per unit area. [195]

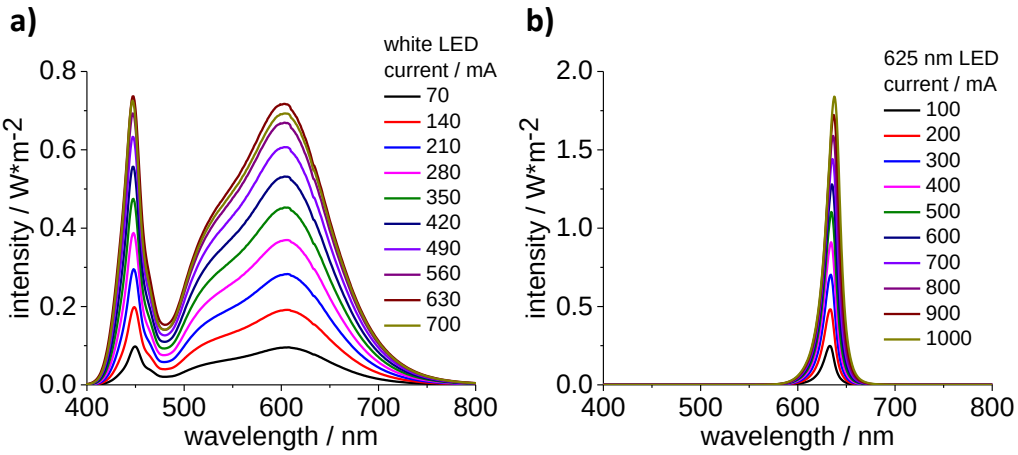

Figure 10.7: Spectra of white and 625 nm LED for different LED currents. Spectra were recorded with a SPECTRO 320 optical scanning spectrometer. a) Broad spectrum of white LED (max. LED current: 700 mA) ranging from 400 to 800 nm. b) Narrow spectrum of 625 nm LED (max. LED current: 1000 mA) ranging from approximately 600 to 650 nm.

Atomic Force Microscopy and Stability Tests

All stability tests were conducted by Frank Balzer using a JPK NanoWizard AFM. Intermittent contact mode measurements were performed with either BudgetSensor Tap-300G tips (resonance frequency = 300 kHz, force constant = 40 N/m and tip radius < 10 nm) or Nanoworld NCH tips (resonance frequency = 320 kHz, force constant = 42 N/m and tip radius < 12 nm). Samples inserted into the Ringer's solution were investigated with another intermittent contact mode tip (NanoWorld Pointprobe CONT, resonance frequency 13 kHz, force constant 0.2 N/m). The JPK NanoWizard AFM was combined with an inverted optical microscope (Nikon Eclipse TE 300) in order to monitor the same sample area by both AFM and optical microscopy. Devices were further illuminated from below through a 40x microscope objective using a halogen lamp. The intensity of the white light through the objective amounted to 2.5 mW/mm^2 with a light power of 1 mW. A microscope slide power meter sensor head (Thorlabs S175C) was used to measure the light power. The analysis of the AFM images was conducted with the software Gwyddion.[192,193] Bleaching experiments, bireflection, and birefringence microscopy were performed with a DMRME polarization microscope. During bleaching tests, the illumination of the samples was conducted from above using a 20x (2.1 mm^2) or 50x (0.4 mm^2) microscope objective. In addition, either single or two crossed linear polarizers were employed resulting in light powers of 2.7 and 0.5 mW, respectively.

An Ocean Optics Maya 2000 spectrometer in combination with the Nikon microscope was used to record spatially resolved optical absorbance spectra. Here, the camera port of the Nikon microscope was connected to the spectrometer via a 200 µm optical fiber.

External Quantum Efficiency and Absorbance Spectra

A Bentham PVE300 system was employed which consisted of a dual xenon/ quartz halogen light source, a Czerny-Turner TMc300 monochromator, and a DTR6 integrating sphere. The monochromatic light beam had a spot size of 1.85 mm^2 with light intensities ranging from 8 $\mu W/mm^2$ at 400 nm to 29 $\mu W/mm^2$ at 700 nm. The light power was measured with a S170C low-power microscope slide power meter sensor head and a PM100D power meter (Thorlabs, US). The total transmission of the samples was measured first under dry conditions by referencing to air. The spectrum had a spectral resolution of 1 nm. The EQE was recorded by inserting the sample into Ringer's solution. The electrical circuit was closed by electrically contacting the ITO electrode and placing a platinum wire into the Ringer's solution. The wavelength resolution and modulation of the monochromatic light were set to 5 nm and 60 Hz, respectively. The data was corrected using the BenWin+ software in reference to the light intensity by performing a calibration with a silicon solar cell first. During recording, no voltage bias was applied. Two amplifiers were employed to measure the photocurrents: ac transimpedance preamplifier with a gain of 10^4 V/A and a Stanford Research SR830 lock-in amplifier.

Scanning and Transmission Electron Microscopy

A FEI Helios NanoLab 600i scanning electron microscopy system was used to prepare lamellas of the device cross section during which platinum is deposited onto the SQIB:PC60BM/ITO/glass device as protective layer first. In order to obtain a free-standing lamella, the material around the lamella was removed in the next step. After detaching the lamella from the device and transferring it to a lift-out TEM grid the tip of the lamella was thinned out until the thickness was under 100 nm. Transmission electron microscopy images of the lamellas were recorded using a Jeol JEM2100F TEM system which was operated at a voltage of 200 keV. Size of the lamella: length: approximately 10 µm, length of the tip that was thinned out: approximately 5 µm, thickness under 100 nm at the tip, height: > 2 µm.

Before recording scanning electron microscopy images using the FEI Helios NanoLab 600i scanning electron microscopy system, 100 nm aluminium was deposited onto the SQIB:PC60BM/ITO/glass devices as a protective layer.

Floating samples for transmission electron microscopy images of platelet and fern structures were prepared by spin coating the SQIB:PC60BM blend solution (950 rpm, ramping 0, 1 sec) onto a 50 nm LiF sacrificial layer that was previously deposited onto glass substrates. After annealing the spin coated samples at 180 °C for 2h the SQIB:PC60BM blend layer was detached from the device by dissolving the LiF layer with a drop of distilled water. The floating SQIB:PC60BM layer was then immediately transferred to a carbon coated Cu-TEM grid. The images were recorded with a Jeol JEM2100F transmission electron microscopy system at an operating voltage of 200 keV.

Bibliography

[1] F. A. Vera-Díaz, N. Doble in *Topics in Adaptive Optics*, InTech, **2012**.

[2] `http://www.nano-retina.com/retinal-degenerative-diseases/\(accessed:September2018)`.

[3] L. Yue, J. D. Weiland, B. Roska, M. S. Humayun, Retinal stimulation strategies to restore vision: Fundamentals and systems, *Prog. Retin. Eye Res.* **2016**, *53*, 21–47.

[4] W. A. Beltran, A. V. Cideciyan, A. S. Lewin, S. Iwabe, H. Khanna, A. Sumaroka, V. A. Chiodo, D. S. Fajardo, A. J. Román, W.-T. Deng, M. Swider, T. S. Alemán, S. L. Boye, S. Genini, A. Swaroop, W. W. Hauswirth, S. G. Jacobson, G. D. Aguirre, Gene therapy rescues photoreceptor blindness in dogs and paves the way for treating human X-linked retinitis pigmentosa, *PNAS* **2012**, *109*, 2132–2137.

[5] E. P. Rakoczy, C.-M. Lai, A. L. Magno, M. E. Wikstrom, M. A. French, C. M. Pierce, S. D. Schwartz, M. S. Blumenkranz, T. W. Chalberg, M. A. Degli-Esposti, I. J. Constable, Gene therapy with recombinant adeno-associated vectors for neovascular age-related macular degeneration: 1 year follow-up of a phase 1 randomised clinical trial, *Lancet.* **2015**, *386*, 2395–2403.

[6] R. N. Fariss, Z. Y. Li, A. H. Milam, Abnormalities in rod photoreceptors, amacrine cells, and horizontal cells in human retinas with retinitis pigmentosa, *Am. J. Ophthalmol.* **2000**, *129*, 215–223.

[7] R. E. Marc, B. W. Jones, C. B. Watt, E. Strettoi, Neural remodeling in retinal degeneration, *Prog. Retin. Eye Res.* **2003**, *22*, 607–655.

[8] S. Y. Kim, S. Sadda, J. Pearlman, M. S. Humayun, E. de Juan Jr, B. M. Melia, W. R. Green, Morphometric analysis of the macula in

eyes with disciform age-related macular degeneration, *Retina.* **2002**, *22*, 471–477.

[9] N. E. Medeiros, C. A. Curcio, Preservation of Ganglion Cell Layer Neurons in Age-Related Macular Degeneration, *Invest. Ophthalmol. Vis. Sci.* **2001**, *42*, 795–803.

[10] M. S. Humayun, E. de Juan Jr., J. D.Weiland, G. Dagnelie, S. Katona, R. Greenberg, S. Suzuki, Pattern electrical stimulation of the human retina, *Vision Res.* **1999**, *39*, 2569–2576.

[11] M. S. Humayun, M. Prince, E. de Juan Jr, Y. Barron, M. Moskowitz, I. B. Klock, A. H. Milam, Morphometric analysis of the extramacular retina from postmortem eyes with retinitis pigmentosa, *Invest. Ophthalmol. Vis. Sci.* **1999**, *40*, 143–148.

[12] A. Santos, M. S. Humayun, E. de Juan Jr, R. J. Greenburg, M. J. Marsch, I. B. Klock, A. H. Milam, Preservation of the Inner Retina in Retinitis Pigmentosa. A Morphometric Analysis., *Arch. Ophthalmol.* **1997**, *115*, 511–515.

[13] J. D. Weiland, A. K. Cho, M. S. Humayun, Retinal Prostheses: Current Clinical Results and Future Needs, *Ophthalmology.* **2011**, *118*, 2227–2237.

[14] H. Beck, W. E. Boden, S. Patibandla, D. Kireyev, V. Gutpa, F. Campagna, M. E. Cain, J. E. Marine, 50th Anniversary of the First Successful Permanent Pacemaker Implantation in the United States: Historical Review and Future Directions, *Am. J. Cardiol.* **2010**, *106*, 810–818.

[15] M. L. Kringelbach, N. Jenkinson, S. L. F. Owen, T. Z. Aziz, Translational principles of deep brain stimulation, *Nat. Rev. Neurosci.* **2007**, *8*, 623–635.

[16] J. K. Niparko, *Cochlear Implants: Principles & Practices*, Lippincott Williams & Wilkens, **2009**.

[17] J. D. Weiland, M. S. Humayun, Visual Prosthesis, *Proc. of the IEEE* **2008**, *96*, 1076–1084.

[18] G. S. Brindley, W. S. Lewin, The sensations produced by electrical stimulation of the visual cortex, *J. Physiol.* **1968**, *196*, 479–493.

[19] A. M. Potts, J. Inoue, The electrically evoked response (EER) of the visual system. II. Effect of adaptation and retinitis pigmentosa., *Invest. Ophthalmol.* **1969**, *8*, 605–612.

[20] J. Besharse, D. Bok, *The Retina and its Disorders*, Elsevier Ltd., **2011**.

[21] J. F. Rizzo, J. Wyatt, J. Loewenstein, S. Kelly, D. Shire, Perceptual efficacy of electrical stimulation of human retina with a microelectrode array during short-term surgical trials, *Invest. Ophthalmol. Vis. Sci.* **2003**, *44*, 5362–5369.

[22] R. Hornig, T. Zehnder, M. Velikay-Parel, T. Laube, M. Feucht, G. Richard in *Artificial Sight*, Springer New York, pp. 111–128.

[23] C. de Balthasar, S. Patel, A. Roy, R.Freda, S. Greenwald, A. Horsager, M. Mahadevappa, D. Yanai, M. J. McMahon, M. S. Humayun, R. J. Greenberg, J. D. Weiland, I. Fine, Factors Affecting Perceptual Thresholds in Epiretinal Prostheses, *Invest. Ophthalmol. Vis. Sci.* **2008**, *49*, 2303–2314.

[24] A. Horsager, S. H. Greenwald, J. D. Weiland, M. S. Humayun, R. J. Greenberg, M. J. McMahon, G. M. Boynton, I. Fine, Predicting visual sensitivity in retinal prosthesis patients, *Invest. Ophthalmol. Vis. Sci.* **2009**, *50*, 1483–1491.

[25] M. Mahadevappa, J. D. Weiland, D. Yanai, I. Fine, R. J. Greenberg, M. S. Humayun, Perceptual thresholds and electrode impedance in three retinal prosthesis subjects, *IEEE Trans. Neural Syst. Rehabil. Eng.* **2005**, *13*, 201–206.

[26] D. Yanai, J. D. Weiland, M. Mahadevappa, R. J. Greenberg, I. Fine, M. S. Humayun, Visual performance using a retinal prosthesis in three subjects with retinitis pigmentosa., *Am. J. Ophthalmol.* **2007**, *143*, 820–827.

[27] A. C. Ho, M. S. Humayun, J. D. Dorn, L. da Cruz, G. Dagnelie, J. Handa, P.-O. Barale, J.-A. Sahel, P. E. Stanga, F. Hafezi, A. B. Safran, J. Salzmann, A. Santos, D. Birch, R. Spencer, A. V. Cideciyan, E. de Juan, J. L. Duncan, D. Eliott, A. Fawzi, L. C. O. de Koo, G. C. Brown, J. A. Haller, C. D. Regillo, L. V. D. Priore, A. Arditi,

D. R. Geruschat, R. J. Greenberg, A. I. S. Group, Long-Term Results from an Epiretinal Prosthesis to Restore Sight to the Blind, *Ophthalmology* **2015**, *122*, 1547–1554.

[28] J. D. Weiland, M. S. Humayun, Retinal prosthesis, *IEEE Trans. Biomed. Eng.* **2014**, *61*, 1412–1424.

[29] Y. H. L. Luo, L. da Cruz, The Argus® II Retinal Prosthesis System, *Prog. Retin. Eye Res.* **2016**, *50*, 89–107.

[30] D. D. Zhou, J. D. Dorn, R. J. Greenberg, *2013 IEEE International Conference on Multimedia and Expo Workshops (ICMEW)*, **2013**.

[31] M. S. Humayun, J. D. Dorn, L. da Cruz, G. Dagnelie, J.-A. Sahel, P. E. Stanga, A. V. Cideciyan, J. L. Duncan, D. Eliott, E. Filley, A. C. Ho, A. Santos, A. B. Safran, A. Arditi, L. V. D. Priore, R. J. Greenberg, A. I. S. Group, Interim results from the international trial of Second Sight's visual prosthesis, *Ophthalmology* **2012**, *119*, 779–788.

[32] Y. H.-L. Luo, J. J. Zhong, L. da Cruz, The use of Argus® II retinal prosthesis by blind subjects to achieve localisation and prehension of objects in 3-dimensional space, *Graefes Arch. Clin. Exp. Ophthalmol.* **2014**, *253*, 1907–1914.

[33] L. da Cruz, B. F. Coley, J. Dorn, F. Merlini, E. Filley, P. Christopher, F. K. Chen, V. Wuyyuru, J. Sahel, P. Stanga, M. Humayun, R. J. Greenberg, G. Dagnelie, A. I. S. Group, The Argus II epiretinal prosthesis system allows letter and word reading and long-term function in patients with profound vision loss, *Br. J. Ophthalmol.* **2013**, *97*, 632–636.

[34] K. Stingl, K. U. Bartz-Schmidt, D. Besch, A. Braun, A. Bruckmann, F. Gekeler, U. Greppmaier, S. Hipp, G. Hortdorfer, C. Kernstock, A. Koitschev, A. Kusnyerik, H. Sachs, A. Schatz, K. T. Stingl, T. Peters, B. Wilhelm, E. Zrenner, Artificial vision with wirelessly powered subretinal electronic implant alpha–IMS, *Proc. Biol. Sci.* **2013**, *280*, 20130077–20130077.

[35] R. Wilke, V.-P. Gabel, H. Sachs, K.-U. B. Schmidt, F. Gekeler, D. Besch, P. Szurman, A. Stett, B. Wilhelm, T. Peters, A. Harscher, U. Greppmaier, S. Kibbel, H. Benav, A. Bruckmann, K. Stingl,

A. Kusnyerik, E. Zrenner, Spatial Resolution and Perception of Patterns Mediated by a Subretinal 16-Electrode Array in Patients Blinded by Hereditary Retinal Dystrophies, *Invest. Ophthalmol. Vis. Sci.* **2011**, *52*, 5995.

[36] E. Zrenner, K. U. Bartz-Schmidt, H. Benav, D. Besch, A. Bruckmann, V.-P. Gabel, F. Gekeler, U. Greppmaier, A. Harscher, S. Kibbel, J. Koch, A. Kusnyerik, T. Peters, K. Stingl, H. Sachs, A. Stett, P. Szurman, B. Wilhelm, R. Wilke, Subretinal electronic chips allow blind patients to read letters and combine them to words., *Proc. R. Soc. B* **2010**, *278*, 1489–1497.

[37] K. Stingl, K. U. Bartz-Schmidt, D. Besch, C. K. Chee, C. L. Cottriall, F. Gekeler, M. Groppe, T. L. Jackson, R. E. MacLaren, A. Koitschev, A. Kusnyerik, J. Neffendorf, J. Nemeth, M. A. N. Naeem, T. Peters, J. D. Ramsden, H. Sachs, A. Simpson, M. S. Singh, B. Wilhelm, D. Wong, E. Zrenner, Subretinal Visual Implant Alpha IMS–Clinical trial interim report, *Vision Res.* **2015**, *111*, 149–160.

[38] K. Stingl, K.-U. Bartz-Schmidt, F. Gekeler, A. Kusnyerik, H. Sachs, E. Zrenner, Functional Outcome in Subretinal Electronic Implants Depends on Foveal Eccentricity, *Invest. Ophthalmol. Vis. Sci.* **2013**, *54*, 7658.

[39] D. Palanker, G. Goetz, Restoring sight with retinal prostheses, *Physics Today* **2018**, *71*, 26–32.

[40] D. Boinagrov, S. Pangratz-Fuehrer, G. Goetz, D. Palanker, Selectivity of direct and network-mediated stimulation of the retinal ganglion cells with epi-, sub- and intraretinal electrodes, *J. Neural Eng.* **2014**, *11*, 026008.

[41] K. Mathieson, J. Loudin, G. Goetz, P. Huie, L. Wang, T. I. Kamins, L. Galambos, R. Smith, J. S. Harris, A. Sher, D. Palanker, Photovoltaic retinal prosthesis with high pixel density, *Nat. Photonics* **2012**, *6*, 391–397.

[42] D. Palanker, A. Vankov, P. Huie, S. Baccus, Design of a high-resolution optoelectronic retinal prosthesis, *J. Neural Eng.* **2005**, *2*, S105–S120.

[43] H. Lorach, G. Goetz, Y. Mandel, X. Lei, T. I. Kamins, K. Mathieson, P. Huie, R. Dalal, J. S. Harris, D. Palanker, Performance of photovoltaic arrays in-vivo and characteristics of prosthetic vision in animals with retinal degeneration, *Vision Res.* **2015**, *111*, 142–148.

[44] H. Lorach, G. Goetz, R. Smith, X. Lei, Y. Mandel, T. Kamins, K. Mathieson, P. Huie, J. Harris, A. Sher, D. Palanker, Photovoltaic restoration of sight with high visual acuity, *Nat. Med.* **2015**, *21*, 476–482.

[45] H. Lorach, J. Wang, D. Y. Lee, R. Dalal, P. Huie, D. Palanker, Retinal safety of near infrared radiation in photovoltaic restoration of sight, *Biomed. Opt. Express* **2015**, *7*, 13.

[46] G. J. Lee, C. Choi, D.-H. Kim, Y. M. Song, Bioinspired Artificial Eyes: Optic Components, Digital Cameras, and Visual Prostheses, *Adv. Funct. Mater.* **2017**, *28*, 1705202.

[47] F. D. Maria, F. Lodola, E. Zucchetti, F. Benfenati, G. Lanzani, The evolution of artificial light actuators in living systems: from planar to nanostructured interfaces, *Chem. Soc. Rev.* **2018**, *47*, 4757–4780.

[48] S. M. Wellman, J. R. Eles, K. A. Ludwig, J. P. Seymour, N. J. Michelson, W. E. McFadden, A. L. Vazquez, T. D. Y. Kozai, A Materials Roadmap to Functional Neural Interface Design, *Adv. Funct. Mater.* **2017**, *28*, 1701269.

[49] R. Chen, A. Canales, P. Anikeeva, Neural recording and modulation technologies, *Nat. Rev. Mater.* **2017**, *2*, 16093.

[50] G. Polino, C. Lubrano, G. Ciccone, F. Santoro, Photogenerated Electrical Fields for Biomedical Applications, *Front. Bioeng. Biotechnol.* **2018**, *6*, 167.

[51] B. J. Schwartz, Conjugated Polymers as Molecular Materials: How Chain Conformation and Film Morphology Influence Energy Transfer and Interchain Interactions, *Annu. Rev. Phys. Chem.* **2003**, *54*, 141–172.

[52] G. Scarpa, A.-L. Idzko, S. Götz, S. Thalhammer, Biocompatibility Studies of Functionalized Regioregular Poly(3-hexylthiophene) Layers for Sensing Applications, *Macromol. Biosci.* **2010**, *10*, 378–383.

[53] P. Fattahi, G. Yang, G. Kim, M. R. Abidian, A Review of Organic and Inorganic Biomaterials for Neural Interfaces, *Adv. Mater.* **2014**, *26*, 1846–1885.

[54] J. Rivnay, R. M. Owens, G. G. Malliaras, The Rise of Organic Bioelectronics, *Chem. Mater.* **2013**, *26*, 679–685.

[55] S. H. Park, R. Su, J. Jeong, S.-Z. Guo, K. Qiu, D. Joung, F. Meng, M. C. McAlpine, 3D Printed Polymer Photodetectors, *Adv. Mater.* **2018**, *30*, 1803980.

[56] D. T. Simon, E. O. Gabrielsson, K. Tybrandt, M. Berggren, Organic Bioelectronics: Bridging the Signaling Gap between Biology and Technology, *Chem. Rev.* **2016**, *116*, 13009–13041.

[57] C. Liao, M. Zhang, M. Y. Yao, T. Hua, L. Li, F. Yan, Flexible Organic Electronics in Biology: Materials and Devices, *Adv. Mater.* **2014**, *27*, 7493–7527.

[58] G. G. Malliaras, Organic bioelectronics: A new era for organic electronics, *Biochim. Biophys. Acta* **2013**, *1830*, 4286–4287.

[59] L. Ferlauto, M. J. I. A. Leccardi, N. A. L. Chenais, S. C. A. Gilliéron, P. Vagni, M. Bevilacqua, T. J. Wolfensberger, K. Sivula, D. Ghezzi, Design and validation of a foldable and photovoltaic wide-field epiretinal prosthesis, *Nat. Commun.* **2018**, *9*, 992.

[60] F. Benfenati, G. Lanzani, New technologies for developing second generation retinal prostheses, *Lab Animal* **2018**, *47*, 71–75.

[61] S. Inal, J. Rivnay, A.-O. Suiu, G. G. Malliaras, I. McCulloch, Conjugated Polymers in Bioelectronics, *Acc. Chem. Res.* **2018**, *51*, 1368–1376.

[62] S. Löffler, K. Melican, K. P. R. Nilsson, A. Richter-Dahlfors, Organic bioelectronics in medicine, *J. Intern. Med.* **2017**, *282*, 24–36.

[63] T. Someya, Z. Bao, G. G. Malliaras, The rise of plastic bioelectronics, *Nature* **2016**, *540*, 379–385.

[64] A. Savchenko, V. Cherkas, C. Liu, G. B. Braun, A. Kleschevnikov, Y. I. Miller, E. Molokanova, Graphene biointerfaces for optical stimulation of cells, *Sci. Adv.* **2018**, *4*, eaat0351.

[65] M. Irimia-Vladu, E. D. Głowacki, G. Voss, S. Bauer, N. S. Sariciftci, Green and biodegradable electronics, *Materials Today* **2012**, *15*, 340–346.

[66] M. Irimia-Vladu, E. D. Glowacki, N. S. Sariciftci, S. Bauer, *Green Materials for Electronics*, Wiley-VCH Verlag GmbH & Co. KGaA, **2017**.

[67] C. J. Bettinger, Recent advances in materials and flexible electronics for peripheral nerve interfaces, *Bioelectronic Medicine* **2018**, *4*, 6.

[68] N. Martino, D. Ghezzi, F. Benfenati, G. Lanzani, M. R. Antognazza, Organic semiconductors for artificial vision, *J. Mater. Chem. B* **2013**, *1*, 3768.

[69] A. Barriga-Rivera, L. Bareket, J. Goding, U. A. Aregueta-Robles, G. J. Suaning, Visual Prosthesis: Interfacing Stimulating Electrodes with Retinal Neurons to Restore Vision, *Front. Neurosci.* **2017**, *11*, 620.

[70] A. R. Harris, G. G. Wallace, Organic Electrodes and Communications with Excitable Cells, *Adv. Funct. Mater.* **2017**, *28*, 1700587.

[71] J. Hopkins, L. Travaglini, A. Lauto, T. Cramer, B. Fraboni, J. Seidel, D. Mawad, Photoactive Organic Substrates for Cell Stimulation: Progress and Perspectives, *Advanced Materials Technologies* **2019**, 1800744.

[72] D. Ghezzi, M. R. Antognazza, R. Maccarone, S. Bellani, E. Lanzarini, N. Martino, M. Mete, G. Pertile, S. Bisti, G. Lanzani, F. Benfenati, A polymer optoelectronic interface restores light sensitivity in blind rat retinas, *Nat. Photonics* **2013**, *7*, 400–406.

[73] V. Gautam, M. Bag, K. S. Narayan, Single-Pixel, Single-Layer Polymer Device as a Tricolor Sensor with Signals Mimicking Natural Photoreceptors, *J. Am. Chem. Soc.* **2011**, *133*, 17942–17949.

[74] V. Gautam, D. Rand, Y. Hanein, K. S. Narayan, A Polymer Optoelectronic Interface Provides Visual Cues to a Blind Retina, *Adv. Mater.* **2013**, *26*, 1751–1756.

[75] V. Gautam, K. S. Narayan, Polymer optoelectronic structures for retinal prosthesis, *Organogenesis* **2014**, *10*, 9–12.

[76] M. R. Antognazza, N. Martino, D. Ghezzi, P. Feyen, E. Colombo, D. Endeman, F. Benfenati, G. Lanzani, Shedding Light on Living Cells, *Adv. Mater.* **2014**, *27*, 7662–7669.

[77] M. R. Antognazza, M. D. Paolo, D. Ghezzi, M. Mete, S. D. Marco, J. F. Maya-Vetencourt, R. Maccarone, A. Desii, F. D. Fonzo, M. Bramini, A. Russo, L. Laudato, I. Donelli, M. Cilli, G. Freddi, G. Pertile, G. Lanzani, S. Bisti, F. Benfenati, Characterization of a Polymer-Based, Fully Organic Prosthesis for Implantation into the Subretinal Space of the Rat, *Adv. Healthc. Mater.* **2016**, *5*, 2271–2282.

[78] E. Mosconi, P. Salvatori, M. I. Saba, A. Mattoni, S. Bellani, F. Bruni, B. S. Gonzalez, M. R. Antognazza, S. Brovelli, G. Lanzani, H. Li, J.-L. Brédas, F. D. Angelis, Surface Polarization Drives Photoinduced Charge Separation at the P3HT/Water Interface, *ACS Energy Lett.* **2016**, *1*, 454–463.

[79] V. Benfenati, N. Martino, M. R. Antognazza, A. Pistone, S. Toffanin, S. Ferroni, G. Lanzani, M. Muccini, Photostimulation of Whole-Cell Conductance in Primary Rat Neocortical Astrocytes Mediated by Organic Semiconducting Thin Films, *Adv. Healthc. Mater.* **2013**, *3*, 392–399.

[80] J. F. Maya-Vetencourt, D. Ghezzi, M. R. Antognazza, E. Colombo, M. Mete, P. Feyen, A. Desii, A. Buschiazzo, M. D. Paolo, S. D. Marco, F. Ticconi, L. Emionite, D. Shmal, C. Marini, I. Donelli, G. Freddi, R. Maccarone, S. Bisti, G. Sambuceti, G. Pertile, G. Lanzani, F. Benfenati, A fully organic retinal prosthesis restores vision in a rat model of degenerative blindness, *Nat. Mater.* **2017**, *16*, 681–689.

[81] L. Bareket-Keren, Y. Hanein, Carbon nanotube-based multi electrode arrays for neuronal interfacing: progress and prospects, *Front. Neural Circuits* **2013**, *6*, 122.

[82] L. Bareket, N. Waiskopf, D. Rand, G. Lubin, M. David-Pur, J. Ben-Dov, S. Roy, C. Eleftheriou, E. Sernagor, O. Cheshnovsky, U. Banin, Y. Hanein, Semiconductor Nanorod-Carbon Nanotube Biomimetic Films for Wire-Free Photostimulation of Blind Retinas, *Nano Lett.* **2014**, *14*, 6685–6692.

[83] J. P. Chinta, N. Waiskopf, G. Lubin, D. Rand, Y. Hanein, U. Banin, S. Yitzchaik, Carbon Nanotube and Semiconductor Nanorods Hybrids: Preparation, Characterization, and Evaluation of Photocurrent Generation, *Langmuir* **2017**, *33*, 5519–5526.

[84] J. L. Duncan, E. A. Pierce, A. M. Laster, S. P. Daiger, D. G. Birch, J. D. Ash, A. Iannaccone, J. G. Flannery, J. A. Sahel, D. J. Zack, M. A. Zarbin, Inherited Retinal Degenerations: Current Landscape and Knowledge Gaps, *Transl. Vis. Sci. Technol.* **2018**, *7*, 6.

[85] N. Martino, P. Feyen, M. Porro, C. Bossio, E. Zucchetti, D. Ghezzi, F. Benfenati, G. Lanzani, M. R. Antognazza, Photothermal cellular stimulation in functional bio-polymer interfaces, *Sci. Rep.* **2015**, *5*, 8911.

[86] M. Sytnyk, M. Jakešová, M. Litviňuková, O. Mashkov, D. Kriegner, J. Stangl, J. Nebesářová, F. W. Fecher, W. Schöfberger, N. S. Sariciftci, R. Schindl, W. Heiss, E. D. Głowacki, Cellular interfaces with hydrogen-bonded organic semiconductor hierarchical nanocrystals, *Nat. Commun.* **2017**, *8*, 91.

[87] F. Lodola, N. Martino, G. Tullii, G. Lanzani, M. R. Antognazza, Conjugated polymers mediate effective activation of the Mammalian Ion Channel Transient Receptor Potential Vanilloid 1, *Sci. Rep.* **2017**, *7*, 8477.

[88] N. Ghosh, A. Das, S. Chaffee, S. Roy, C. K. Sen in *Immunity and Inflammation in Health and Disease*, Elsevier, **2018**, pp. 45–55.

[89] S. F. Cogan, Neural Stimulation and Recording Electrodes, *Annu. Rev. Biomed. Eng.* **2008**, *10*, 275–309.

[90] P. Fromherz, A. Stett, Silicon-Neuron Junction: Capacitive Stimulation of an Individual Neuron on a Silicon Chip, *Physical Review Letters* **1995**, *75*, 1670–1673.

[91] D. Braun, P. Fromherz, Fast Voltage Transients in Capacitive Silicon-to-Cell Stimulation Detected with a Luminescent Molecular Electronic Probe, *Physical Review Letters* **2001**, *86*, 2905–2908.

[92] M. Ulbrich, *PhD Thesis: Öffnen von Ionenkanälen durch kapazitive Kopplung in Zellmembranen auf Siliziumchips (Technical University of Munich)*, **2003**.

[93] M. H. Ulbrich, P. Fromherz, Opening of K^+ channels by capacitive stimulation from silicon chip, *Appl. Phys. A* **2005**, *81*, 887–891.

[94] I. Schoen, P. Fromherz, Activation of Na channels in cell membrane by capacitive stimulation with silicon chip, *Appl. Phys. Lett.* **2005**, *87*, 193901.

[95] I. Schön, *PhD Thesis: Extrazelluläre Stimulation von Ionenkanälen und Nervenzellen mittels Elektrolyt/Oxid/Silizium-Kondensatoren (Technical University of Munich)*, **2006**.

[96] I. Schoen, P. Fromherz, The Mechanism of Extracellular Stimulation of Nerve Cells on an Electrolyte-Oxide-Semiconductor Capacitor, *Biophys. J.* **2007**, *92*, 1096–1111.

[97] P. Fromherz, Semiconductor chips with ion channels, nerve cells and brain, *Physica E: Low-dimensional Systems and Nanostructures* **2003**, *16*, 24–34.

[98] P. Fromherz, *ESSCIRC 2007 - 33rd European Solid-State Circuits Conference*, **2007**.

[99] P. Fromherz, Joining microelectronics and microionics: Nerve cells and brain tissue on semiconductor chips, *Solid-State Electronics* **2008**, *52*, 1364–1373.

[100] D. Rand, M. Jakešová, G. Lubin, I. Vėbraitė, M. David-Pur, V. Đerek, T. Cramer, N. S. Sariciftci, Y. Hanein, E. D. Głowacki, Direct Electrical Neurostimulation with Organic Pigment Photocapacitors, *Adv. Mater.* **2018**, *30*, 1707292.

[101] K. Y. Law, Organic photoconductive materials: recent trends and developments, *Chem. Rev.* **1993**, *93*, 449–486.

[102] S. Sreejith, P. Carol, P. Chithra, A. Ajayaghosh, Squaraine dyes: a mine of molecular materials, *J. Mater. Chem.* **2008**, *18*, 264–274.

[103] D. Ramaiah, I. Eckert, K. T. Arun, L. Weidenfeller, B. Epe, Squaraine dyes for photodynamic therapy: study of their cytotoxicity and genotoxicity in bacteria and mammalian cells, *Photochem. Photobiol.* **2002**, *76*, 672–677.

[104] A. D. Quartarolo, E. Sicilia, N. Russo, On the Potential Use of Squaraine Derivatives as Photosensitizers in Photodynamic Therapy: A TDDFT and RICC2 Survey, *J. Chem. Theory Comput.* **2009**, *5*, 1849–1857.

[105] W. Sun, S. Guo, C. Hu, J. Fan, X. Peng, Recent Development of Chemosensors Based on Cyanine Platforms, *Chem. Rev.* **2016**, *116*, 7768–7817.

[106] N. J. Hestand, C. Zheng, A. R. Penmetcha, B. Cona, J. A. Cody, F. C. Spano, C. J. Collison, Confirmation of the Origins of Panchromatic Spectra in Squaraine Thin Films Targeted for Organic Photovoltaic Devices, *J. Phys. Chem. C* **2015**, *119*, 18964–18974.

[107] G. Chen, H. Sasabe, T. Igarashi, Z. Hong, J. Kido, Squaraine dyes for organic photovoltaic cells, *J. Mater. Chem. A* **2015**, *3*, 14517–14534.

[108] J.-Q. Jiang, C.-L. Sun, Z.-F. Shi, H.-L. Zhang, Squaraines as light-capturing materials in photovoltaic cells, *RSC Adv.* **2014**, *4*, 32987–32996.

[109] S. Brück, C. Krause, R. Turrisi, L. Beverina, S. Wilken, W. Saak, A. Lützen, H. Borchert, M. Schiek, J. Parisi, Structure-property relationship of anilino-squaraines in organic solar cells, *Phys. Chem. Chem. Phys.* **2014**, *16*, 1067–1077.

[110] L. Beverina, P. Salice, Squaraine Compounds: Tailored Design and Synthesis towards a Variety of Material Science Applications, *Eur. J. Org. Chem.* **2010**, *2010*, 1207–1225.

[111] L. Beverina, M. Sassi, Twists and Turns Around a Square: The Many Faces of Squaraine Chemistry, *Synlett* **2014**, *25*, 477–490.

[112] M. Schulz, M. Mack, O. Kolloge, A. Lützen, M. Schiek, Organic photodiodes from homochiral l-proline derived squaraine compounds with strong circular dichroism, *Phys Chem. Chem. Phys.* **2017**, *19*, 6996–7008.

[113] D. Scheunemann, O. Kolloge, S. Wilken, M. Mack, J. Parisi, M. Schulz, A. Lützen, M. Schiek, Revealing the recombination dynamics in squaraine-based bulk heterojunction solar cells, *Appl. Phys. Lett.* **2017**, *111*, 183502.

[114] O. Kolloge, *Master Thesis: The Impact of Active Layer Thickness on the Fill Factor of Squaraine Solar Cells (University of Oldenburg)*, **2018**.

[115] L. Hu, K. Awaga in *Optoelectronics - Devices and Applications*, InTech, **2011**.

[116] L. Hu, X. Liu, S. Dalgleish, M. M. Matsushita, H. Yoshikawa, K. Awaga, Organic optoelectronic interfaces with anomalous transient photocurrent, *J. Mater. Chem. C* **2015**, *3*, 5122–5135.

[117] N. Lago, A. Cester, N. Wrachien, M. Natali, S. D. Quiroga, S. Bonetti, M. Barbato, A. Rizzo, E. Benvenuti, V. Benfenati, M. Muccini, S. Toffanin, G. Meneghesso, A physical-based equivalent circuit model for an organic/electrolyte interface, *Org. Electron.* **2016**, *35*, 176–185.

[118] L. Hu, W. Jin, R. Feng, M. Zaheer, Q. Nie, G. Chen, Z.-J. Qiu, C. Cong, R. Liu, Photovoltage Reversal in Organic Optoelectronic Devices with Insulator-Semiconductor Interfaces, *Materials* **2018**, *11*, 1530.

[119] V. Gautam, M. Bag, K. S. Narayan, Dynamics of Bulk Polymer Heterostructure/Electrolyte Devices, *J. Phys. Chem. Lett.* **2010**, *1*, 3277–3282.

[120] O. Ostroverkhova, Organic Optoelectronic Materials: Mechanisms and Applications, *Chem. Rev.* **2016**, *116*, 13279–13412.

[121] L. Hu, A. Iwasaki, R. Suizu, Y. Noda, B. Li, H. Yoshikawa, M. M. Matsushita, K. Awaga, H. Ito, Effect of photoinduced charge displacement on organic optoelectronic conversion, *Phys. Rev. B* **2011**, *84*, 205329.

[122] G. Chen, H. Sasabe, Y. Sasaki, H. Katagiri, X.-F. Wang, T. Sano, Z. Hong, Y. Yang, J. Kido, A Series of Squaraine Dyes: Effects of Side Chain and the Number of Hydroxyl Groups on Material Properties and Photovoltaic Performance, *Chem. Mater.* **2014**, *26*, 1356–1364.

[123] B. Vonhoeren, S. Dalgleish, L. Hu, M. M. Matsushita, K. Awaga, B. J. Ravoo, Photocurrent Generation in Organic Photodetectors with Tailor-Made Active Layers Fabricated by Layer-by-Layer Deposition, *ACS Appl. Mater. Interfaces* **2015**, *7*, 7049–7053.

[124] L. Hu, Y. Noda, H. Ito, H. Kishida, A. Nakamura, K. Awaga, Optoelectronic conversion by polarization current, triggered by space charges at organic-based interfaces, *Appl. Phys. Lett.* **2010**, *96*, 243303.

[125] L. Hu, A. Iwasaki, R. Suizu, H. Yoshikawa, K. Awaga, H. Ito, Highly efficient alternating photocurrent from interactive organic-radical dimers: A novel light-harvesting mechanism for optoelectronic conversion, *Chem. Phys. Lett.* **2010**, *484*, 177–180.

[126] B. Li, Y. Noda, L. Hu, H. Yoshikawa, M. M. Matsushita, K. Awaga, Highly efficient organic optoelectronic conversion induced by electric double layers in ionic liquids, *Appl. Phys. Lett.* **2012**, *100*, 163304.

[127] L. Reissig, K. Mori, R. Treadwell, S. Dalgleish, K. Awaga, Factors affecting the polarity and magnitude of photoresponse of transient photodetectors, *Phys. Chem. Chem. Phys.* **2016**, *18*, 6821–6830.

[128] M. G. Shapiro, K. Homma, S. Villarreal, C.-P. Richter, F. Bezanilla, Infrared light excites cells by changing their electrical capacitance, *Nat. Commun.* **2012**, *3*, 736.

[129] M. G. Shapiro, K. Homma, S. Villarreal, C.-P. Richter, F. Bezanilla, Corrigendum: Infrared light excites cells by changing their electrical capacitance, *Nat. Commun.* **2017**, *8*, 16148.

[130] R. A. Rhoades, D. R. Bell, *Medical Physiology: Principles for Clinical Medicine*, Lippincott Williams & Wilkens, **2009**.

[131] J. H. Byrne, R. Heidelberger, M. N. Waxham, *From Molecules to Networks: An Introduction to Cellular and Molecular Neuroscience*, Elsevier Inc., **2014**.

[132] B. Alberts, D. Bray, K. Hopkin, A. Johnson, J. Lewis, M. Raff, K. Roberts, P. Walter, *Essential Cell Biology*, Garland Science, Taylor & Francis Group, LLC, **2015**.

[133] N. Sperelakis in *Cell Physiology Source Book: A Molecular Approach*, Academic Press, **2001**, pp. 1205–1219.

[134] N. Sperelakis, *Cell Physiology Source Book: Essentials of Membrane Biophysics*, Elsevier Inc., **2012**.

[135] D. Purves, G. J. Augustine, D. Fitzpatrick, W. C. Hall, A.-S. LaMantia, J. O. McNamara, S. M. Williams, *Neuroscience*, Sinauer Associates, Inc., **2004**.

[136] A. L. Hodgkin, B. Katz, The effect of sodium ions on the electrical activity of the giant axon of the squid, *J. Physiol.* **1949**, *108*, 37–77.

[137] A. L. Hodgkin, The Ionic Basis of Electrical Activity in Nerve and Muscle, *Biol. Rev.* **1951**, *26*, 339–409.

[138] A. L. Hodgkin, A. F. Huxley, Currents carried by sodium and potassium ions through the membrane of the giant axon of Loligo, *J. Physiol.* **1952**, *116*, 449–472.

[139] A. L. Hodgkin, A. F. Huxley, A quantitative description of membrane current and its application to conduction and excitation in nerve, *J. Physiol.* **1952**, *52*, 25–71.

[140] A. L. Hodgkin, The Croonian Lecture - Ionic movements and electrical activity in giant nerve fibres, *Proc. R. Soc. Lond. B Biol. Sci.* **1958**, *148*, 1–37.

[141] P. F. Baker, A. L. Hodgkin, T. I. Shaw, Replacement of the axoplasm of giant nerve fibres with artificial solutions, *J. Physiol.* **1962**, *164*, 330–354.

[142] G. L. Fain, T. J. O'Dell, *Molecular and Cellular Physiology of Neurons*, Harvard University Press, **2014**.

[143] M. P. Blaustein, J. P. Y. Kao, D. R. Matteson, *Cellular Physiology and Neurophysiology*, Mosby, **2012**.

[144] A. L. Hodgkin, W. A. H. Rushton, E. D. Adrian, The electrical constants of a crustacean nerve fibre, *Proc. R. Soc. Med.* **1946**, *133*, 444–479.

[145] E. R. Kandel, J. H. Schwartz, T. M. Jessell, S. A. Siegelbaum, A. J. Hudspeth, *Principles of Neural Science*, McGraw-Hill Education Ltd, **2012**.

[146] C. Hammond, *Cellular and Molecular Neurophysiology*, Elsevier Ltd., **2015**.

[147] M. Chappell, S. Payne, *Physiology for Engineers: Applying Engineering Methods to Physiological Systems*, Springer International Publishing Switzerland, **2016**.

[148] E. Neher, B. Sakmann, Single-channel currents recorded from membrane of denervated frog muscle fibres, *Nature* **1976**, *260*, 799–802.

[149] S. Ströh, C. Puller, S. Swirski, M.-B. Hölzel, L. I. van der Linde, J. Segelken, K. Schultz, C. Block, H. Monyer, K. Willecke, R. Weiler, M. Greschner, U. Janssen-Bienhold, K. Dedek, Eliminating Glutamatergic Input onto Horizontal Cells Changes the Dynamic Range and Receptive Field Organization of Mouse Retinal Ganglion Cells, *J. Neurosci.* **2018**, *38*, 2015–2028.

[150] J. R. Clay, Comparison of the effects of internal TEA^+ and Cs^+ on potassium current in squid giant axons, *Biophys. J.* **1985**, *48*, 885–892.

[151] A. Molleman, *Patch Clamping: An Introductory Guide to Patch Clamp Electrophysiology*, John Wiley & Sons Ltd, **2003**.

[152] W. Walz, A. A. Boulton, G. B. Baker, *Patch-Clamp Analysis Advanced Techniques*, Humana Press Inc., **2002**.

[153] T. Jue, *Modern Tools of Biophysics*, Springer Science+Business Media LLC, **2017**.

[154] S. Dhein, F. W. Mohr, M. Delmar, *Practical Methods in Cardiovascular Research*, Springer-Verlag Berlin Heidelberg, **2005**.

[155] L. Luo, *Principles of Neurobiology*, Garland Science, Taylor & Francis Group, LLC, **2016**.

[156] J. Magistretti, M. Mantegazza, E. Guatteo, E. Wanke, Action potentials recorded with patch-clamp amplifiers: are they genuine?, *Trends Neurosci.* **1996**, *19*, 530–534.

[157] U. Windhorst, H. Johansson, *Modern Techniques in Neuroscience Research*, Springer-Verlag Berlin Heidelberg, **1999**.

[158] G. B. Rutkowski, *Operational Amplifiers: Integrated and Hybrid Circuits*, John Wiley & Sons, Inc., **1993**.

[159] J. Avison, *The World of Physics*, Thomas Nelson and Sons Ltd, **1989**.

[160] F. Bretschneider, J. R. de Weille, *Introduction to Electrophysiological Methods and Instrumentation*, Elsevier Ltd., **2006**.

[161] J. Rettinger, S. Schwarz, W. Schwarz, *Electrophysiology: Basics, Modern Approaches and Applications*, Springer International Publishing Switzerland, **2016**.

[162] R. Pethig, S. Smith, *Introductory Bioelectronics: For Engineers and Physical Scientists*, John Wiley & Sons, Ltd, **2013**.

[163] B. D. Ratner, A. S. Hoffman, F. J. Schoen, J. E. Lemons, *Biomaterials Science: An Introduction to Materials in Medicine*, Elsevier Inc., **2013**.

[164] D. R. Merrill, M. Bikson, J. G. Jefferys, Electrical stimulation of excitable tissue: design of efficacious and safe protocols, *J. Neurosci. Methods* **2005**, *141*, 171–198.

[165] H. Helmholtz, Studien über electrische Grenzschichten, *Annalen der Physik und Chemie* **1879**, *243*, 337–382.

[166] J. G. Webster, *Medical Instrumentation: Application and Design*, John Wiley & Sons, Inc., **2010**.

[167] S. G. O. G. Martinsen, *Bioimpedance and Bioelectricity Basics*, Elsevier Ltd., **2015**.

[168] P. W. Macfarlane, A. van Oosterom, O. Pahlm, P. Kligfield, M. Janse, J. Camm, *Comprehensive Electrocardiology*, Springer-Verlag London Limited, **2011**.

[169] F. Rattay, Analysis of Models for External Stimulation of Axons, *IEEE Trans. Biomed. Eng.* **1986**, *BME-33*, 974–977.

[170] A. Köhler, H. Bässler, *Electronic Processes in Organic Semiconductors*, Wiley-VCH Verlag GmbH & Co. KGaA, **2015**.

[171] W. C. H. Choy, *Organic Solar Cells: Materials and Device Physics*, Springer-Verlag London, **2013**.

[172] W. Tress, *Organic Solar Cells: Theory, Experiment, and Device Simulation*, Springer International Publishing Switzerland, **2014**.

[173] W. Brütting, C. Adachi, *Physics of Organic Semiconductors*, Wiley-VCH Verlag & Co. KGaA, **2012**.

[174] P. J. Walla, *Modern Biophysical Chemistry Detection and Analysis of Biomolecules*, Wiley-VCH Verlag GmbH & Co. KGaA, **2014**.

[175] W. Hu, *Organic Optoelectronics*, Wiley-VCH Verlag GmbH & Co. KGaA, **2013**.

[176] F. A. Carey, R. J. Sundberg, *Advanced Organic Chemistry: Part A: Structure and Mechanisms*, Kluwer Academic Publishers, **2000**.

[177] S. Ogawa, *Organic Electronics Materials and Devices*, Springer Japan, **2015**.

[178] K. A. Mazzio, C. K. Luscombe, The future of organic photovoltaics, *Chem. Soc. Rev.* **2015**, *44*, 78–90.

[179] K. Takei, *Flexible and Strechable Medical Devices*, Wiley-VCH Verlag GmbH & Co. KGaA, **2018**.

[180] J. Hölzl, F. K. Schulte in *Springer Tracts in Modern Physics*, Springer Berlin Heidelberg, **1979**, pp. 1–150.

[181] D. K. Schroder, *Semiconductor Material and Device Characterization*, John Wiley & Sons, Inc., **2006**.

[182] R. D. J. van Vuuren, A. Armin, A. K. Pandey, P. L. Burn, P. Meredith, Organic Photodiodes: The Future of Full Color Detection and Image Sensing, *Adv. Mater.* **2016**, *28*, 4766–4802.

[183] S. Shoaee, M. Stolterfoht, D. Neher, The Role of Mobility on Charge Generation, Recombination, and Extraction in Polymer-Based Solar Cells, *Advanced Energy Materials* **2018**, *8*, 1703355.

[184] O. S. Abdullaeva, M. Schulz, F. Balzer, J. Parisi, A. Lützen, K. Dedek, M. Schiek, Photoelectrical Stimulation of Neuronal Cells by an Organic Semiconductor-Electrolyte Interface, *Langmuir* **2016**, *32*, 8533–8542.

[185] F. Balzer, H. Kollmann, M. Schulz, G. Schnakenburg, A. Lützen, M. Schmidtmann, C. Lienau, M. Silies, M. Schiek, Spotlight on Excitonic Coupling in Polymorphic and Textured Anilino Squaraine Thin Films, *Cryst. Growth Des.* **2017**, *17*, 6455–6466.

[186] G. Pescitelli, L. D. Bari, N. Berova, Application of electronic circular dichroism in the study of supramolecular systems, *Chem. Soc. Rev.* **2014**, *43*, 5211–5233.

[187] B. Heyne, Self-assembly of organic dyes in supramolecular aggregates, *Photochem. Photobiol. Sci.* **2016**, *15*, 1103–1114.

[188] K. C. Deing, U. Mayerhöffer, F. Würthner, K. Meerholz, Aggregation-dependent photovoltaic properties of squaraine/$PC_{61}BM$ bulk heterojunctions, *Phys. Chem. Chem. Phys.* **2012**, *14*, 8328.

[189] K. Feron, R. Lim, C. Sherwood, A. Keynes, A. Brichta, P. Dastoor, Organic Bioelectronics: Materials and Biocompatibility, *Int. J. Mol. Sci.* **2018**, *19*, 2382.

[190] M. C. Lensen, V. A. Schulte, J. Salber, M. Diez, F. Menges, M. Möller, Cellular responses to novel, micropatterned biomaterials, *Pure and Applied Chemistry* **2008**, *80*, 2479–2487.

[191] F. Gentile, L. Tirinato, E. Battista, F. Causa, C. Liberale, E. M. di Fabrizio, P. Decuzzi, Cells preferentially grow on rough substrates, *Biomaterials* **2010**, *31*, 7205–7212.

[192] D. Nečas, P. Klapetek, Gwyddion: an open-source software for SPM data analysis, *Open Phys.* **2012**, *10*, 181.

[193] P. Klapetek, *Quantitative Data Processing in Scanning Probe Microscopy: SPM Applications for Nanometrology*, Elsevier Inc., **2018**.

[194] A. Yadav, *Solid State Devices and Circuits*, University Science Press, **2008**.

[195] J. Hecht, *Understanding Fiber Optics*, Laser Light Press, **2015**.

[196] O. S. Abdullaeva, F. Balzer, M. Schulz, J. Parisi, A. Lützen, K. Dedek, M. Schiek, Organic Photovoltaic Sensors for Photocapacitive Stimulation of Voltage-Gated Ion Channels in Neuroblastoma Cells, *Adv. Funct. Mater.* **2018**, 1805177.

[197] C. A. Schneider, W. S. Rasband, K. W. Eliceiri, NIH Image to ImageJ: 25 years of image analysis, *Nat. Methods* **2012**, *9*, 671–675.

[198] J. Schindelin, I. Arganda-Carreras, E. Frise, V. Kaynig, M. Longair, T. Pietzsch, S. Preibisch, C. Rueden, S. Saalfeld, B. Schmid, J.-Y. Tinevez, D. J. White, V. Hartenstein, K. Eliceiri, P. Tomancak, A. Cardona, Fiji: an open-source platform for biological-image analysis, *Nat. Methods* **2012**, *9*, 676–682.

[199] Y.-M. Leung, C.-F. Huang, C.-C. Chao, D.-Y. Lu, C.-S. Kuo, T.-H. Cheng, L.-Y. Chang, C.-H. Chou, Voltage-gated K^+ channels play a role in cAMP-stimulated neuritogenesis in mouse neuroblastoma N2A cells, *J. Cell. Physiol.* **2011**, *226*, 1090–1098.

[200] A. Randall, N. McNaughton, P. Green, Properties of voltage-gated Na^+ channels in the human rhabdomyosarcoma cell-line SJ-RH30: Conventional and automated patch clamp analysis, *Pharmacol. Res.* **2006**, *54*, 118–128.

[201] A. Feigenspan, K. Dedek, K. Schlich, R. Weiler, S. Thanos, Expression and Biophysical Characterization of Voltage-Gated Sodium Channels in Axons and Growth Cones of the Regenerating Optic Nerve, *Invest. Ophthalmol. Vis. Sci.* **2010**, *51*, 1789.

[202] A. R. Harris, C. Newbold, P. Carter, R. Cowan, G. G. Wallace, Measuring the effective area and charge density of platinum electrodes for bionic devices, *Journal of Neural Engineering* **2018**, *15*, 046015.

[203] A. Corna, T. Herrmann, G. Zeck, Electrode-size dependent thresholds in subretinal neuroprosthetic stimulation, *J. Neural Eng.* **2018**, *15*, 045003.

[204] D. Sliney, M. Wolbarscht, *Safety with Lasers and Other Optical Sources: A Comprehensive Handbook*, Springer Science+Business Media New York, **1980**.

[205] V. Nesterov, `Nest-o-Patch2.0\https://sourceforge.net/projects/nestopatch/\(acessed:April2018&December2018)`.

List of Publications

O. S. Abdullaeva, M. Schulz, F. Balzer, J. Parisi, A. Lützen,
K. Dedek, M. Schiek
Photoelectrical Stimulation of Neuronal Cells by an Organic Semiconductor-Electrolyte Interface
Langmuir **2016**, *32*, 8533-8542.
DOI: 10.1021/acs.langmuir.6b02085

O. S. Abdullaeva, F. Balzer, M. Schulz, J. Parisi, A. Lützen,
K. Dedek, M. Schiek
Organic Photovoltaic Sensors for Photocapacitive Stimulation of Voltage-Gated Ion Channels in Neuroblastoma Cells
Adv. Funct. Mater. **2018**, 1805177.
DOI: 10.1002/adfm.201805177

M. Schulz, J. Zablocki, O. S. Abdullaeva, S. Brück, F. Balzer, A. Lützen,
O. Arteaga, M. Schiek
Giant intrinsic circular dichroism of prolinol-derived squaraine thin films
Nat. Commun. **2018**, *9*, 2413.
DOI: 10.1038/s41467-018-04811-7

CURRICULUM VITAE

Oliya S. Abdullaeva
Carl-von-Ossietzky Str. 1A
26129 Oldenburg

Education

01/2014–present
Ph.D Student
Optoelectronic Organics
Energy and Semiconductor Research Laboratory, Institute of Physics
University of Oldenburg, Germany
DFG-German Research Foundation-Research Training Group
GRK 1885/1: "*Molecular Basis of Sensory Biology*"

10/2011–12/2013
Master of Science in Chemistry
Grade: 2.2, University of Bonn, Germany
Master thesis in supramolecular chemistry at the Kekulé-Institute of Organic Chemistry and Biochemistry:
"*Synthese von Bis(chelat)-Liganden auf der Basis von Ferrocen und deren Selbstorganisation zu heteroleptischen metallosupramolekularen Komplexen*"
(grade: 1.0)

10/2008–09/2011
Bachelor of Science in Chemistry
Grade: 2.8, University of Bonn, Germany
Bachelor thesis in supramolecular chemistry at the Kekulé-Institute of Organic Chemistry and Biochemistry:
"*1,10-Phenanthroline als Bausteine in der metallosupramolekularen Chemie*"
(grade: 1.7)

08/1998–06/2006
Higher education entrance qualification (A-levels), Abitur
Grade: 2.2
Mädchengymnasium Jülich St. Josef-Schule, Germany
02/1997–07/1998
Nordschule Jülich, Germany
09/1994–07/1995
Public School 253 Oceanview School
New York City, USA

Scholarship

01/2014–12/2016
Ph.D. scholarship by the DFG-German Research Foundation-Research Training Group GRK 1885/1: "*Molecular Basis of Sensory Biology*"

Honors and Awards

10/2016
Young Researcher in Focus (4^{th} quarter 2016)
Gateway to Vision Research
06/2016
ZEISS Scientific Poster Award (3^{rd} Place)
Young Researcher Vision Camp
08/2015
Selected for the 129^{th} BASF International Summer Course,
BASF SE, Ludwigshafen am Rhein

Languages

German: fluent
English: fluent
Uzbek: native tongue
French: basic

Talks

09/2018

"*Stimulation of Voltage-Gated Ion Channels in Neuronal Model Cells by a Photovoltaic Organic Artificial Photoreceptor*"
O. S. Abdullaeva, F. Balzer, M. Schulz, J. Parisi, A. Lützen,
K. Dedek, M. Schiek
22. Deutsche Physikerinnentagung
Oldenburg, Germany

03/2016

"*Optoelectronic solid-liquid interfaces as potential artificial photoreceptors*"
O. S. Abdullaeva, M. Schulz, F. Balzer, J. Parisi, A. Lützen,
K. Dedek, M. Schiek
International Winterschool on Bioelectronics BioEl 2016
Kirchberg in Tirol, Austria

09/2015

"*Optoelectronic Interfaces as Artificial Photoreceptors: Application of Squaraine as Photoconductive Thin Film for the Photostimulation of Biological Cells*"
O. S. Abdullaeva, M. Schulz, A. Lützen, F. Balzer, J. Parisi,
K. Dedek, M. Schiek
8th Workshop on Conjugated Oligomers and Polymers (KOPO)
Würzburg, Germany

Posters

05/2017

"*Artificial Organic Photoreceptors for Photo-Electrical Stimulation of Neuronal Cells*"
O. S. Abdullaeva, F. Balzer, K. Habashy, M. Schulz, J. Parisi, A. Lützen,
K. Dedek, M. Schiek
E-MRS Spring Meeting
Strasbourg, France

06/2016

"*Photoelectrical Stimulation of Neuronal Cells by an Organic Semiconductor-Electrolyte Interface*"

O. S. Abdullaeva, M. Schulz, F. Balzer, J. Parisi, A. Lützen,
K. Dedek, M. Schiek

Young Researcher Vision Camp, 2016 See & Hear
Castle Wildenstein, Leibertingen, Germany

08/2015

"*Optoelectronic interfaces as artificial photoreceptors: Photostimulation of biological cells grown on photoconductive thin films based on organic semiconductors*"

O. S. Abdullaeva, M. Schulz, A. Lützen, F. Balzer, K. Dedek,
J. Parisi, M. Schiek

129^{th} BASF International Summer Course, BASF SE
Ludwigshafen am Rhein, Germany

04/2015

"*Optoelectronic Interfaces as Artificial Photoreceptors*"

O. S. Abdullaeva, M. Schulz, A. Lützen, K. Dedek, J. Parisi, M. Schiek

From the Witches Cauldrons in Materials Science
Goslar, Germany

03/2015

„*Optoelectronic Interfaces for Restoration of Degenerated Retina*"

O. S. Abdullaeva, M. Schiek, K. Dedek, M. Schulz, A. Lützen, J. Parisi

79. Jahrestagung der DPG und DPG-Frühjahrstagung
Berlin, Germany

03/2015

"*Optoelectronic Interfaces as Artificial Photoreceptors*"

O. S. Abdullaeva, M. Schulz, A. Lützen, K. Dedek, J. Parisi, M. Schiek

International Winterschool on Bioelectronics BioEl 2015
Kirchberg in Tirol, Austria

02/2014

"*Facilitating artificial glutamate-based stimulation of degenerated retina*"

O. S. Abdullaeva, M. Schiek, J. Parisi

International Winterschool on Bioelectronics BioEl 2014
Kirchberg in Tirol, Austria